HU ISSN 1586–2070

JOURNAL OF COMPUTATIONAL AND APPLIED MECHANICS

A Publication of the University of Miskolc

VOLUME 6, NUMBER 1 (2005)

MISKOLC UNIVERSITY PRESS

HU ISSN 1586–2070

JOURNAL OF COMPUTATIONAL AND APPLIED MECHANICS

A Publication of the University of Miskolc

VOLUME 6, NUMBER 1 (2005)

MISKOLC UNIVERSITY PRESS

EDITORIAL BOARD

LOCAL EDITORIAL COUNCIL

Journal of Computational and Applied Mechanics, Vol. 6., No. 1., (2005), pp. 3–13

JOULE HEATING EFFECTS ON A MICROPOLAR FLUID PAST A STRETCHING SHEET WITH VARIABLE ELECTRIC CONDUCTIVITY

Walid Aniss Aissa
High Institute of Energy
Department of Mechanical Power, Aswan, Egypt
walidaniss@hotmail.com

Ahmed Ali Mohammadein
South Valley University
Faculty of Science, Department of Mathematics, Aswan, Egypt
mohammadein@yahoo.com

[Received: March 16, 2004]

Abstract. The magneto-hydrodynamic (MHD) and joule heating effect on a laminar micropolar fluid boundary layer past a continuous, linearly stretching, non-isothermal sheet (with prescribed wall heat flux) is considered. The study considers the effects of viscous dissipation and internal heat generation. The governing momentum, angular momentum and energy equations are solved to evaluate the details of the velocity and temperature fields including heat transfer rate. Graphs are presented for the velocity and temperature fields for various micropolar fluid parameters and magnetic field with variable electric conductivity.

Mathematical Subject Classification: 76W05
Keywords: joule heating, magnetic field, micropolar fluid, stretching sheet

1. Introduction

In recent years, the dynamics of micropolar fluids, originating from the theory of Eringen [1], has been a popular area of research. This theory takes into account the effect of local rotary inertia and couple stresses arising from practical microrotation action. This theory is applied to suspensions, liquid crystals, polymeric fluids and turbulence. This behavior is familiar in many engineering and physical applications. Many stages in nuclear reactors and MHD generators working under the influence of external magnetic fields could be examined and controlled using the present model. Na and Pop [2] investigated the boundary layer flow of a micropolar fluid past a stretching wall. Desseaux and Kelson [3] studied the flow of a micropolar fluid bounded by a stretching sheet. Hady [4] studied the solution of heat transfer to micropolar fluid from a non-isothermal stretching sheet with injection. In all the above studies, the authors took the stretching sheet to be oriented in horizontal direction. Abo-Eldahab and Ghonaim [5] investigated convective heat transfer in an electrically conducting micropolar fluid at a stretching surface with uniform free stream.

Mohammadein and Gorla [6] studied the heat transfer characteristics of a laminar boundary layer of a micropolar fluid over a linearly stretching sheet with prescribed uniform surface temperature or prescribed wall heat flux and viscous dissipation and internal heat generation. However, of late, the effects of a magnetic field on the micropolar fluid problem are very important. Mohammadein and Gorla [7] presented a numerical study for the boundary layer of a horizontal plate placed in a micropolar fluid. They analyzed the effects of a magnetic field with vectored surface mass transfer and induced buoyancy streamwise pressure gradients on heat transfer. They investigated the impact of the magnetic field, mass transfer, buoyancy, and material parameters on the surface friction and heat transfer rates.

Siddheshwar and Pranesh [8] investigated magneto-convection in a micropolar fluid.

The present work investigates the effects of joule heating on a laminar micropolar fluid with variable electric conductivity past a linearly stretching, continuous sheet in the presence of a uniform magnetic field. The study considers the surface with prescribed wall heat flux varying with distance using a numerical technique based on the shooting method.

The effects of the magnetic parameter (M_n), suction parameter (f_w), Eckert number (E) and microrotation parameter (Δ) on the velocity of the fluid, temperature distribution and angular velocity of microstructures as well as the coefficient of heat flux and shearing stress at the plate are investigated at specific values of Prandtl number ($Pr = 0.72$), ($B_1 = 0.1$). Different values of physical parameters are tabulated and discussed numerically and graphically.

2. **Formulation of the problem**

A steady, incompressible laminar two-dimensional boundary layer of an incompressible electrically conducting micropolar fluid spreading over a permeable plane surface is considered. The applied magnetic field is primarily in the y-direction and varies in strength as a function of x and is defined as:

$$\underline{B} = (0, B(x)) \ . \tag{2.1}$$

Let us consider the Cartesian coordinates (x, y) introduced for the description of the magneto-hydrodynamic flow (Figure 1). The sheet is located at $y = 0$ and its leading edge is the origin of the Cartesian coordinate system.

The external electric field is assumed to be zero and the magnetic Reynolds number is assumed to be small. Hence, the induced magnetic field is small compared with the external magnetic field. Moreover, the electrical conductivity σ is assumed to have the form:

$$\sigma = \sigma_0 u \ , \tag{2.2}$$

where σ_0 is a constant.

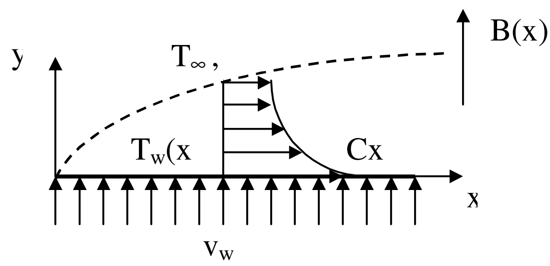

Figure 1. Flow model and coordinate system

The fluid of density (ρ) is at rest and the motion is created by stretching the sheet with a speed proportional to the distance from the fixed origin ($x = 0$). The viscosity coefficient (μ) remains constant, the pressure gradient and body forces are negligible in the presence of viscous dissipation and internal heat generation. The effects of uniform mass and heat transfer characteristics in stationary surroundings are investigated. Under these assumptions, the governing equations within the boundary layer are given by:

1. Continuity equation:

$$\frac{\partial u}{\partial x} + \frac{\partial v}{\partial y} = 0\ , \tag{2.3}$$

2. Momentum equation:

$$u\frac{\partial u}{\partial x} + v\frac{\partial u}{\partial y} = (\nu + \frac{K}{\rho})\frac{\partial^2 u}{\partial y^2} + \frac{K}{\rho}\frac{\partial N}{\partial y} - \frac{\sigma\left(B\left(x\right)\right)^2 u}{\rho}\ , \tag{2.4}$$

3. Angular momentum:

$$u\frac{\partial N}{\partial x} + v\frac{\partial N}{\partial y} = \frac{\gamma}{\rho j}\frac{\partial^2 N}{\partial y^2} - \frac{K}{\rho j}(2N + \frac{\partial u}{\partial y})\ , \tag{2.5}$$

where u and v are the velocity components along the x and y axes, respectively, N is angular velocity, K is vortex viscosity, ν is kinematic viscosity, γ is spin gradient viscosity, and j is the micro inertia per unit mass.

For the flow under study, it is relevant to assume that the applied magnetic field strength; $B\left(x\right)$ has the form [9]:

$$B\left(x\right) = \frac{B_0}{\sqrt{x}}, \quad B_0 \quad \text{is constant.} \tag{2.6}$$

The third term in equation (2.4), taking into account equations (2.2) and (2.6) can be rewritten as:

$$\frac{\sigma\left(B\left(x\right)\right)^2 u}{\rho} = \frac{\sigma_0 B_0^2 u^2}{\rho x}\ . \tag{2.7}$$

By substituting from equation (2.7) in equation (2.4), the momentum equation can be rewritten as:

$$u\frac{\partial u}{\partial x}+v\frac{\partial u}{\partial y}=(\nu+\frac{K}{\rho})\frac{\partial^2 u}{\partial y^2}+\frac{K}{\rho}\frac{\partial N}{\partial y}-\frac{\sigma_0 B_0^2}{\rho x}u^2\ . \tag{2.8}$$

The appropriate boundary conditions are given by:

$$u=Cx,\ v=v_w,\ N=-s\frac{\partial u}{\partial y}\quad \text{at}\quad y=0\quad \&\quad u=0,\ N=0\quad \text{as}\quad y\to\infty\ . \tag{2.9}$$

Positive and negative values for v_w indicate blowing and suction respectively, while $v_w=0$ corresponds to an impermeable sheet.

A comment on the boundary conditions used for the microrotation term will be made here. When $s=0$, we obtain from the boundary condition (2.9) for the microrotation that $N(x,0)=0$, which represents the case of concentrated particle flows in which the microelements close to the wall are not able to rotate as was stated by Jena and Mathur [10]. The case corresponding to $s=1/2$ results in the vanishing of the antisymmetric part of the stress tensor and represents weak concentrations and the case corresponding to s =1 is representative of turbulent boundary layer flows.

A stream function $\psi(x,y)$ is now defined which satisfies the continuity equation (2.3) with

$$u=\frac{\partial\psi}{\partial y},v=-\frac{\partial\psi}{\partial x}\ . \tag{2.10}$$

Proceeding with the analysis, the following transformations are introduced:

$$\eta=\sqrt{\frac{C}{v}}y,\quad \psi=\sqrt{Cv}xf(\eta),\quad N=C\sqrt{\frac{C}{v}}xg(\eta)\ . \tag{2.11}$$

Hence,

$$u=Cxf'(\eta),\quad v=-\sqrt{Cv}f(\eta)\ , \tag{2.12}$$

where primes denote differentiation with respect to η, and the velocity components u and v satisfy the continuity equation (2.3).

The momentum and angular momentum equations can be rewritten as:

$$(1+\Delta)\,f'''+\Delta g'+ff''-M_n\,[f']^2=0\ , \tag{2.13}$$

$$\lambda g''-\Delta B_1\,(2g+f'')-gf'+fg'=0\ , \tag{2.14}$$

where

$$\Delta=\frac{K}{\mu},\quad Mn=1+\frac{\sigma_0 B_0^2}{\rho},\quad \lambda=\frac{\gamma}{\mu j},\quad B_1=\frac{\nu}{Cj}\ , \tag{2.15}$$

in which M_n is the magnetic parameter and Δ is the microrotation parameter. The latter represents a measure of the relative importance of microrotation and viscous effects.

The corresponding boundary conditions are

$$f\,(0)=-\frac{v_w}{\sqrt{Cv}}=f_w\ ,\quad f'\,(0)=1\ ,\quad g\,(0)=0\ , \tag{2.16}$$

$$f'\,(\infty)=0\quad \text{and}\quad g\,(\infty)=0\ . \tag{2.17}$$

The case corresponding to $f_w < 0$ ($v_w > 0$) implies blowing, $f_w > 0$ ($v_w < 0$) implies suction and $f_w = 0$ ($v_w = 0$) corresponds to an impermeable stretching sheet.

The shearing stress at the sheet is given by:

$$\tau_w = \left[(\mu + K) \frac{\partial u}{\partial y} + KN \right]_{y=0} = \mu C \sqrt{\frac{C}{v}} x \left[(1+\Delta) f''(0) + \Delta g(0) \right] . \tag{2.18}$$

It is clear that the wall shear stress will increase with increasing x. The skin friction coefficient C_f takes the form:

$$C_f = -\frac{\tau_w}{\frac{1}{2}\rho (Cx)^2} = \frac{-2}{(Re_x)^{1/2}} \left[(1+\Delta) f''(0) + \Delta g(0) \right] , \tag{2.19}$$

where

$$Re_x = \frac{Cx^2}{\nu} \tag{2.20}$$

is the local Reynolds number.

4. Energy equation:

Including the microrotation dissipation effects, which are quite important in the thermal boundary layer region, modifies the energy equation:

$$u\frac{\partial T}{\partial x} + v\frac{\partial T}{\partial y} = \frac{k}{\rho C_P}\frac{\partial^2 T}{\partial y^2} + \frac{(\mu+K)}{\rho C_P}\left(\frac{\partial u}{\partial y}\right)^2 + \frac{\sigma (B(x))^2}{\rho C_P} u^2 , \tag{2.21}$$

where T is temperature, k is thermal conductivity, C_P is specific heat at constant pressure.

The viscous dissipation term $\frac{\nu}{C_P}\left(\frac{\partial u}{\partial y}\right)^2$ in equation (2.21) is valid for a viscous fluid in the boundary layer:

$$u\frac{\partial T}{\partial x} + v\frac{\partial T}{\partial y} = \frac{k}{\rho C_P}\frac{\partial^2 T}{\partial y^2} + \frac{(\mu+K)}{\rho C_P}\left(\frac{\partial u}{\partial y}\right)^2 + \frac{\sigma_0 B_0^2}{\rho C_P x} u^3 . \tag{2.22}$$

The thermal boundary conditions depend on the type of heating process being considered, which is prescribed heat flux.

The boundary conditions are

$$-k\left(\frac{\partial T}{\partial y}\right) = q_w(x) = bx^m \quad \text{at} \quad y = 0 \quad \& \quad T = T_\infty \quad \text{as} \quad y \to \infty . \tag{2.23}$$

Defining the temperature distribution as

$$T - T_\infty = \frac{D}{k}\sqrt{\frac{v}{C}}\left(\frac{x}{L}\right)^2 \theta(\eta) , \tag{2.24}$$

where T_∞ is a constant temperature of the ambient fluid far from the sheet.

Using the similar variables in equations (2.11) and (2.12), the energy equation (2.22) can be transformed into an ordinary differential equation with the aid of the boundary conditions (2.23) and non-dimensional temperature (2.24) to get

$$\frac{1}{\Pr}\theta'' + E(1+\Delta)(f'')^2 - 2\theta f' + f\theta' + E(Mn-1)(f')^3 = 0 , \tag{2.25}$$

in which the Eckert number is defined as

$$E = \frac{k}{D} \frac{L^2}{\sqrt{Cv}} \frac{C^3}{C_p} \ . \tag{2.26}$$

The transformed boundary conditions may be written as

$$\theta' (0) = -\frac{b}{D} L^2 x^{m-2}, \theta (\infty) = 0 \ . \tag{2.27}$$

But as $\theta'(0)$ must be equal to -1, this implies (as could be concluded from equation (2.27)) that $m = 2$ and b should satisfy the following relation

$$b = D/L^2 \ . \tag{2.28}$$

The set of transformed governing equations (2.13-2.14) and (2.25) are solved using a fourth order Runge-Kutta method of numerical integration.

In order to start a solution, the values of boundary conditions at $\eta = 0$ are substituted and integration must be carried out up to some large η to see if the boundary conditions at infinity are satisfied.

3. Results and discussion

The present work generalized the problem of joule heating effects on a boundary layer of a micropolar fluid over a stretching sheet with variable electric conductivity in the presence of a magnetic field. After some transformations, a numerical solution has been obtained by the fourth order Runge-Kutta method. Results are obtained for a range of Eckert number, magnetic, joule heating and microrotation parameters by applying a numerical technique based on the Shooting method. The sheet is assumed to be non-isothermal with prescribed heat flux varying with length.

The velocity (f'), microrotation (g) and temperature gradient (θ') are plotted versus η for various values of Δ and specific values of the physical parameters [$f_w = 0.2$, $E = 0.5$, $M_n = 1.0$] in Figures 2-4, for various values of M_n and [$\Delta = 1.5$, $f_w = 0.2$, $E = 0.5$] in Figures 5-7 and for various values of f_w and [$\Delta = 0.0$, $E = 0.01$, $M_n = 0.5$] in Figures 9-11. The temperature gradient (θ') is plotted versus η for various values of Eckert number (E) and ($\Delta = 0.5$, $f_w = 0.2$, $M_n = 1.0$) in Figure 8.

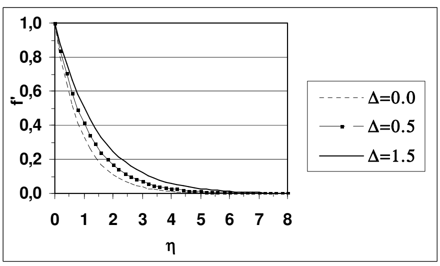

Figure 2. Velocity variation ($f_w = 0.2$, $E = 0.5$, $M_n = 1.0$)

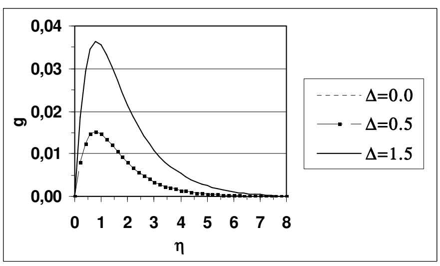

Figure 3. Microrotation variation ($f_w = 0.2$, $E = 0.5$, $M_n = 1.0$)

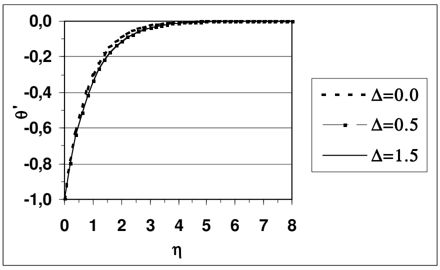

Figure 4. Temperature gradient variation ($f_w = 0.2$, $E = 0.5$, $M_n = 1.0$)

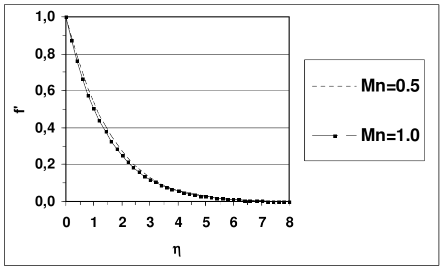

Figure 5. Velocity variation ($\Delta = 1.5$, $f_w = 0.2$, $E = 0.5$)

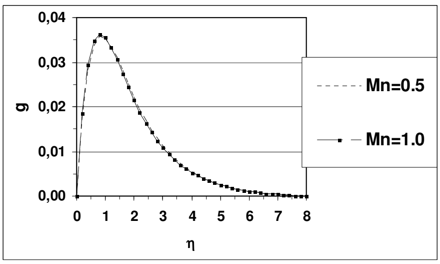

Figure 6. Microrotation variation ($\Delta = 1.5$, $f_w = 0.2$, $E = 0.5$)

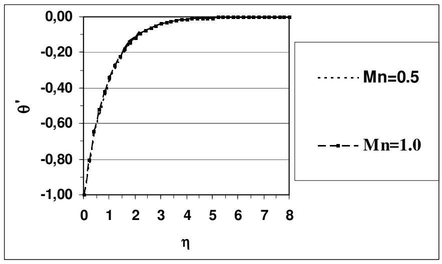

Figure 7. Temperature gradient variation ($\Delta = 1.5$, $f_w = 0.2$, $E = 0.5$)

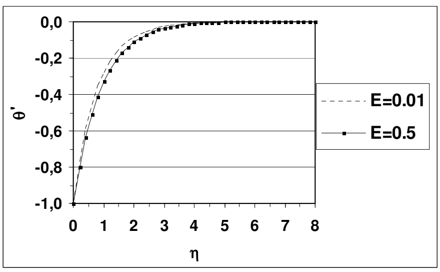

Figure 8. Temperature gradient variation ($\Delta = 0.5$, $f_w = 0.2$, $M_n = 1.0$)

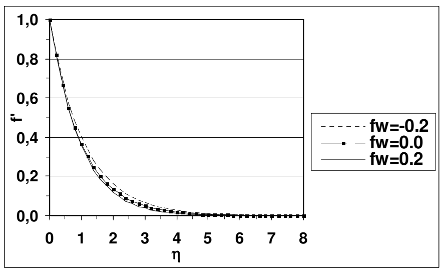

Figure 9. Velocity variation ($\Delta = 0.0$, $E = 0.0.01$, $M_n = 0.5$)

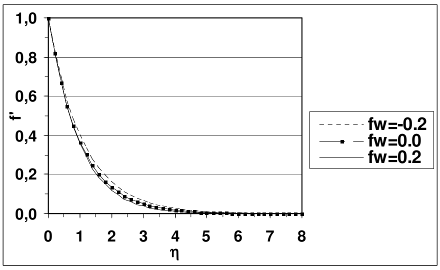

Figure 10. Temperature gradient variation ($\Delta = 0.5$, $f_w = 0.2$, $M_n = 1.0$)

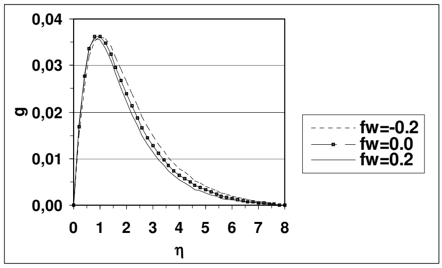

Figure 11. Velocity variation ($\Delta = 0.0$, $E = 0.0.01$, $M_n = 0.5$)

Table 1. Wall values of temperature and gradients of velocity and microrotation gradient.

Δ	f_w	E	M_n	$-f''(0)$	$\theta(0)$	$g'(0)$
0.0				0.83	0.9257	0
0.5	0.0	0.01	0.5	0.6755	0.8695	0.0408
1.5				0.5155	0.8309	0.0935
0.0				1.0001	0.9543	0
0.5	0.0	0.01	1.0	0.8141	0.8906	0.0438
1.5				0.6219	0.8456	0.1018
0.0				0.9051	0.9931	0
0.5	-0.2	0.01	1.0	0.7501	0.9394	0.0384
1.5				0.5829	0.8968	0.0892
0.0				0.9421	0.8946	0
0.5	0.2	0.01	0.5	0.7497	0.8263	0.0466
1.5				0.56	0.7849	0.107
0.0				1.105	0.9201	0
0.5	0.2	0.01	1.0	0.8836	0.8444	0.0493
1.5				0.6635	0.7972	0.1149
0.0				0.83	1.095	0
0.5	0.0	0.5	0.5	0.6755	1.0462	0.0408
1.5				0.5155	1.0244	0.0935
0.0				1.0001	1.0789	0
0.5	0.0	0.5	1.0	0.8141	1.0204	0.0438
1.5				0.6219	0.9878	0.1018
0.0				0.9421	1.0755	0
0.5	0.2	0.5	0.5	0.7497	1.0096	0.0466
1.5				0.56	0.9826	0.107
0.0				1.105	1.0616	0
0.5	0.2	0.5	1.0	0.8836	0.9859	0.0493
1.5				0.6635	0.9483	0.1149
0.0				0.9051	1.1025	0
0.5	-0.2	0.5	1.0	0.7501	1.0576	0.0384
1.5				0.5829	1.0297	0.0892

It may be concluded from Figures 4 and 8 that the absolute value of the temperature gradient (θ‘) decreases with increasing η and increases with increasing Δ and Eckert number (E). Figure 7 illustrates that the temperature gradient (θ‘) decreases with increasing M_n up to a certain η (~ 2.4). For further increase in η, M_n has no effect on the temperature gradient. The transition value of η increases with increasing Δ. It may be remarked from Figure 11 that the absolute value of the temperature gradient in the case of blowing is greater than that of suction. It may be concluded also from the results that the Eckert number (E) does not affect f’, g, f”.

It may be remarked that in general M_n has an adverse effect to that of Δ. This may be attributed to the fact that M_n has the same effect on the flow field as increasing viscosity.

The dimensionless wall values of velocity, temperature gradient and microrotation gradient are shown in Table 1 for various parameters, Δ, M_n, E and f_w.

It may be noted that the wall temperature ($\theta(0)$) decreases as Δ increases, which agrees with findings mentioned in [6].

The skin friction (C_f), which is a physical quantity of a great practical interest, can be obtained from equation (2.19) by specifying the local Reynolds number (Re_x) which is in Table 2.

Table 2. Variation of $C_f\sqrt{Re_x}$

E	f_w	M_n	$\Delta = 0.0$	$\Delta = 0.5$	$\Delta = 1.5$
0.01	-0.2	0.5	1.8102	2.2503	2.9145
	0		2.0002	2.4423	3.1095
	0.2		1.8842	2.2491	2.8
0.5	0.2	0.5	1.8842	2.2491	2.8
		1	2.21	2.6508	3.3175

It is clear that the Eckert number has no effect on skin friction (C_f), and that C_f is dependent on Δ and M_n. The increase of Δ or M_n leads to an increase in the skin friction coefficient of the sheet. Increasing Δ leads to an increase in buoyancy force, which increases the wall shear stress hence increasing the skin friction coefficient. This is a consequence of the existence of a favorable pressure gradient above the sheet due to the buoyancy effects and the wall shear stress is larger than the non-buoyant case. This matches the conclusion by Mohammadein and Gorla [6]. The increase of skin friction is due to the increase in the magnetic field, which may be attributed to the fact stated earlier that an increasing magnetic field is comparable to increasing the flow viscosity, which leads to skin friction increase. This coincides with findings by Helmy [11].

4. **Concluding remarks**

In this work, the equations governing the MHD and joule heating effects on the wall jet flow of a laminar micropolar fluid past a linearly stretching, continuous sheet are solved. The sheet is assumed to be non-isothermal with a prescribed wall heat flux varying with distance. The effects of the magnetic parameter, suction parameter, Eckert number and microrotation parameter are investigated. It was found that the velocity decreases with increasing magnetic parameter, and increases with increasing microrotation parameter. It may be concluded that the increase in the magnetic field has the same influence on the flow field as increasing viscosity. The skin friction coefficient, which is an important physical quantity, increases with increasing both the microrotation parameter and the magnetic field parameter, which effect is analogous to increasing of viscous effect. It is evident that the temperature increases with an increasing Eckert number and magnetic parameter.

References

1. Eringen, A. C.: Theory of micropolar fluids. *Journal of Mathematics and Mechanics*, **16**, (1966), 1-18.
2. Na, T. Y. and Pop, I.: Boundary-layer flow of micropolar fluid due to a stretching wall. *Archives of Applied Mechanics*, **67**(4), (1997), 229-236.
3. Desseaux, A. and Kelson, N. A.: Flow of a micropolar fluid bounded by a stretching sheet. Anziam J., **42**(E), (2000), C536-C560.
4. Hady, F. M.: On the solution of heat transfer to micropolar fluid from a non-isothermal stretching sheet with injection. *International Journal of Numerical Methods for Heat and Fluid Flow*, **6**(6), (1966), 99-104.
5. Abo-Eldahab, E. M. and Ghonaim, A. F.: Convective heat transfer in an electrically conducting micropolar fluid at a stretching surface with uniform free stream. *Appl. Math. Comput.*, **137**, (2003), 323-336.
6. Mohammadein, A. A. and Gorla, R.: Heat transfer in a micropolar fluid over a stretching sheet with viscous dissipation and internal heat generation. *International Journal of Numerical Methods for Heat and Fluid Flow*, **11**(1), (2001), 50-58.
7. Mohammadein, A. A. and Gorla, R. S. R.: Effects of transverse magnetic field on mixed convection in a micropolar fluid on a horizontal plate with vectored mass transfer. *Acta Mechanica*, **118**, (1996), 1-12.
8. Siddheshwar, P. G. and Pranesh, S.: Magneto convection in a micropolar fluid. *Int. J. Engng. Sci.*, 36(10), (1998), 1173-1181.
9. Helmy, K. A.: MHD Boundary layer equations for power law fluids with variable electric conductivity. *Mechanica*, **30**, (1995), 187-200.
10. Jena, S. K. and Mathur, M. N.: Similarity solutions for laminar free convection flow of a thermomicropolar fluid past a non-isothermal vertical flat plate. *Int. J. Enging. Sci.*, **19**, (1981), 1431-1442.
11. Helmy, K. A.: Effects of the magnetic field on a non-Newtonian conducting fluid past a stretching plate. *Can. J. Phys.*, **72**, (1994), 290-292.

NOMENCLATURE

$B(x)$	Strength of the transverse magnetic field	x	Distance measured along the surface
B_0	A constant which first occurs in equation (2.6)	y	Distance measured perpendicularly to the surface
C	A constant which first occurs in equation (2.9)	Δ	Microrotation parameter
C_f	Local skin friction coefficient	γ	Spin gradient viscosity
C_p	Specific heat at constant pressure	η	Similarity space variable
D	A constant which first occurs in equation (2.24)	μ	Viscosity coefficient
E	Eckert number	ν	Kinematic viscosity
f	Dimensionless velocity function	θ	Non - dimensional temperature
g	Dimensionless microrotation	ρ	Fluid density
J	Micro inertia per unit mass	σ	Electrical conductivity of the fluid
k	Thermal coductivity	σ_0	A constant which first occurs in equation (2.2)
K	Vortex viscosity	τ	Shear stress
L	Characteristic length	ψ	Stream function
m	Exponent in the power law variation of the surface heat flux		
M_n	Magnetic parameter		
N	Angular velocity	Subscripts	
Pr	Prandtl number	w	Surface conditions
q	Heat flux.	∞	Conditions away from the surface
Re_x	Local Reynolds number		
T	Temperature	Superscripts	
u	Velocity component in the x direction	$'$	Differentiation with respect to η

Journal of Computational and Applied Mechanics, Vol. 6., No. 1., (2005), pp. 15–25

SIMILARITY SOLUTION FOR MHD FLOW THROUGH VERTICAL POROUS PLATE WITH SUCTION

Mohammad Ferdows, Masahiro Ota
Department of Mechanical Engineering, Tokyo Metropolitan University
1-1 Minami-osawa, Hachioji, Tokyo 192-0397, Japan
ferdows@comp.metro-u.ac.jp, ota-masahiro@c.metro-u.ac.jp

Abdus Sattar
Department of Computer Science and Engineering
North South University, Dhaka, Bangladesh
asattar@northsouth.edu

Mahamud Alam
Department of Mathematics, Khulna University
Khulna, Bangladesh
ku@bdonline.com

[Received: October 28, 2004]

Abstract. In this paper a similarity analysis is made for the forced and free convection boundary layer flow in a semi-infinite expanse of an electrically conducting viscous incompressible fluid past a semi-infinite non-conducting porous plate with suction. A uniform magnetic field is applied normal to the plate. A time dependent suction is also introduced. The governing equations of the problems are then reduced to linear similarity equations, which are made local by introducing suitable similarity parameters. These local similarity equations are solved numerically by an adapting shooting method which uses the Nachtsheim-swigert interaction technique. Effects of various parameters on the velocity and temperature fields across the boundary layer are investigated. Numerical results for the velocity and temperature distributions are shown graphically.

Mathematical Subject Classification: 76W05
Keywords: magneto-hydrodynamics, forced and free convection, porous plate, magnetic field

1. Introduction

Magneto-hydrodynamics (MHD) is the branch of continuum mechanics which deals with the flow of electrically conducting fluids in electric and magnetic fields. Many natural phenomena and engineering problems are worth being subjected to an MHD analysis. Magneto-hydrodynamic equations are ordinary electromagnetic and hydrodynamic equations modified to take into account the interaction between the motion of the fluid and the electromagnetic field. The formulation of the electromagnetic theory in a mathematical form is known as Maxwell's equation.

The effect of the gravity field is always present in forced flow heat transfer as a result of the buoyancy forces connected with the temperature differences. Usually they are of a small order of magnitude so that the external forces may be neglected.

There has recently been a considerable interest in the effect of body forces on forced convection phenomena. The effect of the gravity field is always present in forced flow heat transfer as a result of the buoyancy forces caused by temperature differences. Usually they are small and can be neglected. In certain engineering problems, however, they cannot be left out of consideration. It is important to realize that the heat transfer in mixed convection can be significantly different from that both in pure natural convection and in pure forced convection.

The study of forced and free convection flow and heat transfer for electrically conducting fluids past a semi-infinite porous plate under the influence of a magnetic field has attracted the interest of many investigators in view of its applications in many engineering problems such as geophysics, astrophysics, boundary layer control in the field of aerodynamics (Soundalgekar et al. 1977 [1]). The physical model and geometrical coordinates are shown in Figure 1.

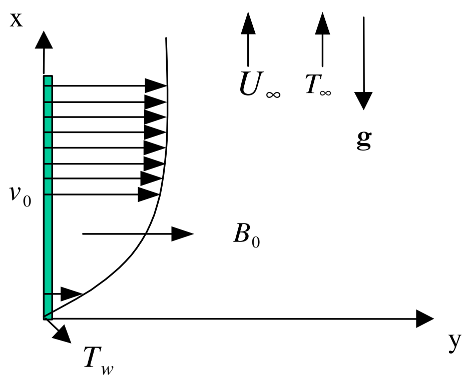

Figure 1. The physical model

In many practical fields, we found significant temperature differences between the surface of the hot body and the free stream. These temperature differences cause density gradients in the fluid medium and in presence of gravitational forced free convection effects become important. by applying transverse magnetic field Agrawal *et al.* [2] found that the rate of heat transfer from the plate to the fluid decreases as the suction velocity increases and the skin friction decreases with increasing Hartman number. Georgantopulos et al. [3], Raptis et al. [4, 5], Soundalgekar and Takher [1] and many others elucidated the various aspects of MHD free convection flows with suction. Some of the earlier works were done by Sparrow et al. [6], Lloyad and Sparrow [7], Wilks [8], Chen et al. [9], Tingwei et al. [10], and Raju et al.

[11]. In addition to the above, studies about convective flows in a porous medium have attracted considerable interest owing to their applications in geophysical and geothermal problems. Theoretical studies of such a flow under free convection were done among others by Bestmen [12, 13], Raptis [4, 5] and Perdikis [14]. Sattar [15] obtained an analytic solution of the free and forced convection flow through a porous medium near the leading edge by a perturbation method adopted by Singh and Dikshit [16]. Soundalgekar et al. [17], Perdiks [14], Sattar [18] made analytical studies on the combined forced and free convection flow in a porous medium. In these studies it has been generally recognized that $\gamma = G_r/R_e^2$ (where G_r is the Grashof number and R_e is the Reynolds number) is the governing parameter for a vertical plate. In the present work, therefore the effect of the large suction on the MHD forced and free convection flow past a vertical porous plate is studied. Solutions to the problem posed are found numerically for the whole range of the buoyancy parameter γ that is considered to be the driving force of the whole range of the combined forced and free convection.

2. Governing equations of the flow and mathematical analysis

Consider the forced and free convection flow of an incompressible viscous and electrically conducting fluid past a heated semi-infinite vertical porous plate.

The fluid is permeated by a strong magnetic field $\vec{B} = [0, B_0(x), 0]$. T_∞, U_∞ are the temperature and velocity of the uniform flow, respectively. The induced magnetic field is assumed to be negligible. This assumption is justified by the fact that the magnetic Reynolds number is very small. Further, since no external electric field is applied, the effect of polarization of the ionized fluid is negligible and it may also be assumed that the electric field $\vec{E} = 0$. Regarding the convection as a result of the effects of thermal diffusion, the equations of motion without Hall effects can be put into the following forms:

The continuity equation:

$$\frac{\partial u}{\partial x} + \frac{\partial v}{\partial y} = 0 \,. \tag{1}$$

The momentum equation:

$$u\frac{\partial u}{\partial x} + v\frac{\partial u}{\partial y} = \upsilon\frac{\partial^2 u}{\partial y^2} + g\beta\,(T - T_\infty) + \frac{\sigma_0 B_0^2(x)}{\rho}\,(U_\infty - u) \,. \tag{2}$$

The energy equation:

$$u\frac{\partial T}{\partial x} + v\frac{\partial T}{\partial y} = \frac{\kappa}{\rho C_p}\frac{\partial^2 T}{\partial y^2} \,. \tag{3}$$

The boundary conditions for the present problem are as follows

$$\begin{array}{llll} u = 0, & v = v_0(x), & T = T_w, & \text{if } y = 0 \,; \\ u = U_\infty, & v = 0, & T = T_\infty, & \text{if } y \to \infty \,, \end{array} \tag{4}$$

where $v_0(x)$ is the velocity of suction and U_∞ is the free steam velocity.

Equations (1)-(3) constitute the basic equations which govern the physical problem considered here. Our next task is to make an approach that will lead to the solutions of these equations provided that the boundary conditions are given by equations (4).

In order to attain a similarity solution to our problem, the following transformations are applied:

$$lll\eta = y\sqrt{\frac{U_\infty}{2\upsilon x}}, \quad u = U_\infty f'(\eta), \quad f_w = v_0(x)\sqrt{\frac{2x}{\upsilon U_\infty}}\,, \qquad \theta = \frac{T - T_\infty}{T_W - T_\infty}\,, \tag{5}$$

where f_w is the transpiration parameter.

We now introduce the following dimensionless local parameters in the above equation:

$$G_{rx} = \frac{U_\infty g\beta\,(T_w - T_\infty)\,x^2}{\upsilon v_0^2\,(x)}\,,\ R_{ex} = \frac{U_\infty x}{\upsilon}\quad , f_w = v_0(x)\sqrt{\frac{2x}{\upsilon U_\infty}}\,,$$
$$\gamma = \frac{G_{rx}}{R_{ex}^2}\,,\ M = \frac{\sigma_0 B_0^2\,(x)\,2x}{U_\infty \rho\, f_w^2}\ .$$

After performing the transformations we obtain the differential equations

$$f''' + ff'' + f_w^2 M(1 - f') = -\gamma f_w^2 \theta\,, \tag{6}$$
$$\theta'' + P_r f\theta' = 0\ . \tag{7}$$

Making use of the dimensionless variables (5) the boundary conditions (4) can be manipulated into form

$$\begin{array}{llll} f = f_w, & f' = 0, & \theta = 1 & \text{if } \eta = 0\,; \\ f' = 1, & & \theta = 0, & \text{if } \eta \to \infty\,. \end{array} \tag{8}$$

It is interesting to note that when suction is absent, i.e. $f_w = 0$, equation (6) reduces to the ordinary Blasius equation. The solutions of the Blasius equation are referred to as the Blasius solutions. They have also been studied by Schlichting [19].

On the other, hand if $\gamma \to 0$, R_e is large and the forced convection is dominating, equation (6) corresponds to the ordinary Falkner and Skan equation. In this case the boundary conditions differ largely from those of the original Falkner and Skan equation.

3. **Numerical scheme and procedure:**

Equations (6) and (7) with boundary conditions (8) are solved numerically using a standard initial value solver, i.e., the shooting method. For the purpose of this method, we applied the Nacthsheim-Swigert iteration technique (Nachtsheim & Swigert, 1965).

In a shooting method, the missing (unspecified) initial condition at the initial point of the interval is assumed and the differential equation is integrated numerically as an initial value problem to the terminal point. The accuracy of the assumed missing initial condition is then checked by comparing the calculated value of the dependent variable at the terminal point with its given value there. If a difference exists, another value of the missing initial condition must be assumed and the process is repeated. This process is continued until the agreement between the calculated and the given condition at the terminal point is within the specified degree of accuracy. For this type of iterative approach, one naturally inquires whether or not there is a systematic way of finding each succeeding (assumed) value of the missing initial condition.

The boundary conditions (8) associated with the linear ordinary differential equations (6) and (7) of the boundary layer type are of the two-point asymptotic class. Two-point boundary conditions have values of the dependent variable specified at two different values of the independent variable. Specification of an asymptotic boundary condition implies the value of velocity approaches to unity and the value of temperature approaches to zero as the outer specified value of the independent variable is approached. The method of numerically integrating two-point asymptotic boundary value problem of the boundary layer type, the initial value method, requires that the problem be recast as an initial value problem. Thus it is necessary to set up as many boundary conditions at the surface as there are at infinity. The governing differential equations are then integrated with these assumed surface boundary conditions. If the required outer boundary condition is satisfied, a solution has beeen achieved. However, this is not generally the case. Hence a method must be devised to logically estimate the new surface boundary conditions for the next trial integration. Asymptotic boundary value problems such as those governing the boundary layer equations are further complicated by the fact that the outer boundary condition is specified at infinity. In the trial integration infinity is numerically approximated by some large value of the independent variable. There is no a priori general method of estimating this value. Selection of too small a maximum value for the independent variable may not allow the solution to asymptotically converge to the required accuracy. Selecting a large value may result in divergence of the trial integration or in slow convergence of surface boundary conditions required satisfying the asymptotic outer boundary condition. Selecting too large a value of the independent variable is expensive in terms of computer time. Nachtsheim-Swigert developed an iteration method, which overcomes these difficulties. Extension of the Nachtsheim-Swigert iteration shell to above equation system of differential equations (6) and (7) is straightforward. In equation (8) there are two asymptotic boundary conditions and hence two unknown surface conditions $f'(0)$ and $\theta'(0)$.

4. **Results and discussion**

In this paper we have attempted to solve the combined free and forced convection flow in a semi-infinite vertical porous plate with suction. Locally similar solutions of this problem have been obtained by introducing a similarity parameter taken to be a time dependent scale. The suction velocity is taken to be a function of time. Under these conditions the solutions to the problem are finally obtained by employing a numerical technique.

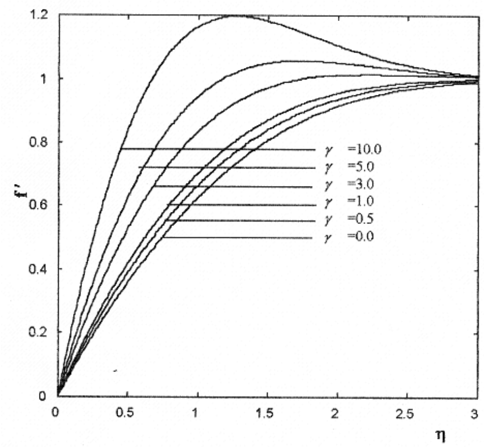

Figure 2. Dimensionless velocity for different values of γ and $P_r = 0.71,\ f_w = 0.5,\ M = 2.0$

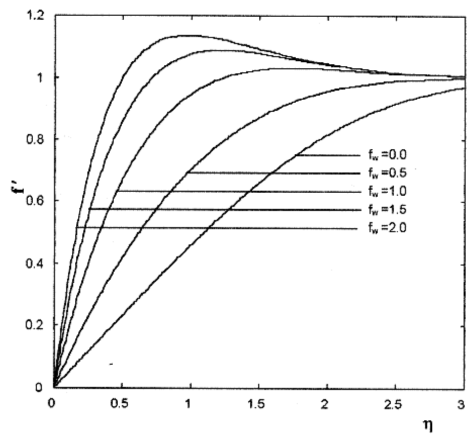

Figure 3. Dimensionless velocity for different values of f_w and $P_r = 0.71,\ \gamma = 1.0,\ M = 2.0$

For the purpose of discussing the numerical solutions, the effects of various parameters on the flow behavior have been determined for different values of the buoyancy parameter γ, suction/ injection parameter f_w, Prandtl number P_r and magnetic parameter M. Since there are four parameters of interest in the present problem, which can be varied, we have focused attention on the values $\gamma = 0.0,\ 0.5,\ 1.0,\ 3.0,\ 5.0,\ 10.0$; $f_w = 0.0,\ 0.5,\ 1.0,\ 1.5,\ 2.0$; $P_r = 0.71,\ 1.0,\ 7.0$ and $M = 2,\ 4, 6$.

In Figure 2, the effects of the driving parameter γ on the velocity profiles are shown. It is obvious from this Figure that the velocity increases with the increasing values of γ, which signifies that the velocity is higher in the case of pure free convection than

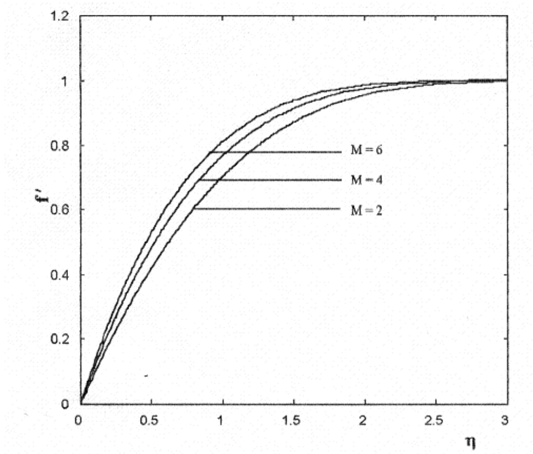

Figure 4. Dimensionless velocity for different values of M and $P_r = 0.71,\ \gamma = 1.0,\ f_w = 0.5$

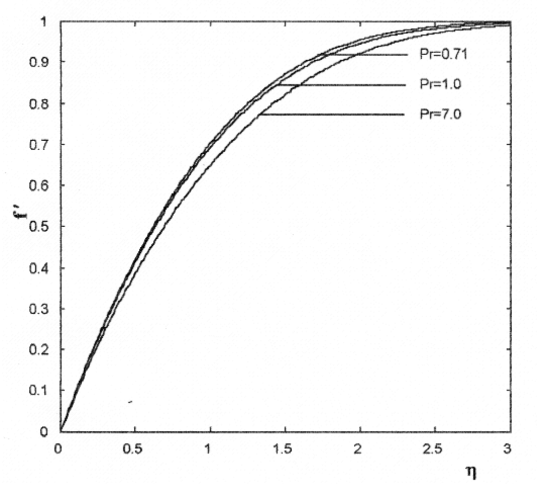

Figure 5. Dimensionless velocity for different values of P_r and $M = 2.0,\ \gamma = 1.0,\ f_w = 0.5$

for pure forced convection. Moreover, in the case of pure free convection, the *velocity* is found to overshoot.

In the case of mixed convection ($\gamma = 1$) a rise in f_w (suction) causes a rise in the velocity as shown in Figure 3. As is shown in the Figure, if suction increases, there is a decrease in the boundary layer growth, which indicates that suction destabilizes the boundary layer.

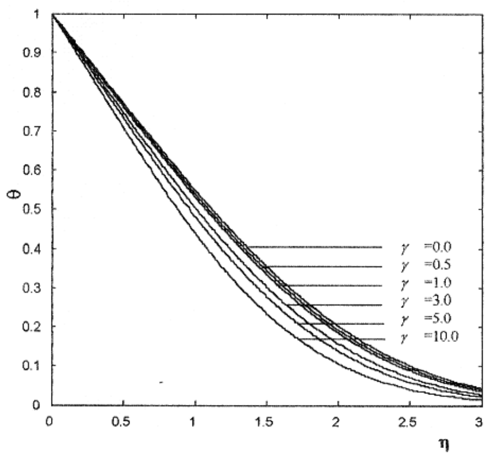

Figure 6. Dimensionless temperature for different values of γ and $M = 2.0,\ P_r = 0.71,\ f_w = 0.5$

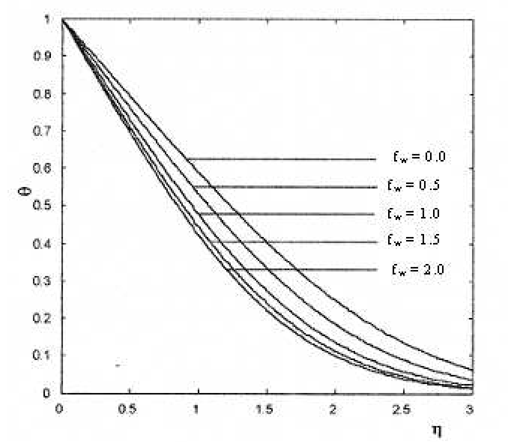

Figure 7. Dimensionless temperature for different values of f_w and $M = 2.0,\ P_r = 0.71,\ \gamma = 1.0$

The effects of the magnetic parameter on the velocity profiles are displayed in Figure 4, which shows that the velocity increases with the increase of the magnetic parameter.

In Figure 5 the effects of the Prandtl number on the velocity profiles are shown. It can be seen from this Figure that the velocity profiles decrease due to the increasing values of the Prandtl number.

In Figure 6, the effects of the buoyancy parameter γ on the temperature profiles are shown. From this Figure it can be seen that the temperature decreases with the increase of γ.

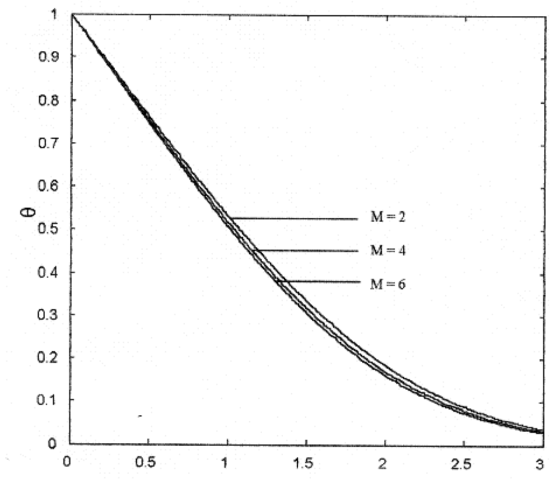

Figure 8. Dimensionless temperature for different values of M and $P_r = 0.71,\ \gamma = 1.0,\ f_w = 0.5$

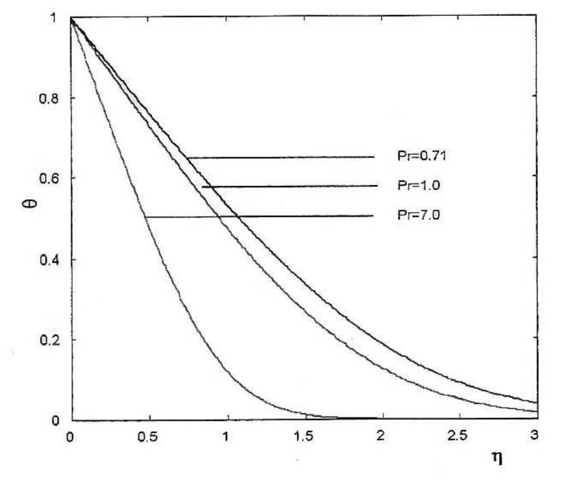

Figure 9. Dimensionless temperature for different values of P_r and $\gamma = 1.0,\ f_w = 0.5,\ M = 2.0$

In Figure 7, the effects of the suction parameter on the temperature profiles are shown. From this Figure it can be seen that the temperature decreases with the increase of the suction parameter.

In Figure 8, the effects of the magnetic parameter on the temperature profiles are shown. From this Figure it can be seen that the temperature decreases with the increase of magnetic parameter.

The effects of the Prandtl number on the temperature are depicted in Figure 9. From this Figure it can be noted that the temperature profiles decrease with the increase in the Prandtl number. These effects are the same as those for velocity profiles.

5. **Conclusion**

We have examined the governing equations for an unsteady incompressible fluid past a semi-infinite vertical porous plate embedded in a porous medium and subjected to the presence of a transverse magnetic field. Numerical results are presented to illustrate the details of the various parameters. The values of driving parameter γ as shown above, however, correspond to three regimes, namely the predominantly forced convection regime, the mixed convection regime and the predominantly free convection regime. For γ=0,the gravity induced free convection is absent and the flow is completely forced over the surface. For low values of γ ($0 < \gamma < 1$), the forced convection dominates and the local similarity solutions are the same as those in the case of forced convection only, which was studied by Narain and Uberoi [20]. The large values of $\gamma \gg 1$) are interesting from a physical point of view. For this purpose, value of $\gamma = 5$ can be essentially treated as the free convection representation.

Appendix A. **Nomenclature**

x, y, z	cartesian coordinates	g	gravitational acceleration
t	time	G_r	Grashof number
f_w	transpiration parameter	C_p	specific heat
u, v	fluid velocities	R_{ex}	Reynolds number
V_0	velocity of suction	T	temperature
μ	kinematics viscosity	γ	buoyancy parameter
η	similarity variable	T_w	plate temperature
υ	coefficient of kinematics viscosity	T_∞	free steam temperature
θ	dimensionless temperature	T_0	reference temperature
ρ	fluid density	κ	heat diffusivity coefficient
$\overrightarrow{B}$	magnetic field	U_∞	free steam velocity
β	coefficient of volume expansion	$\eta = y\sqrt{\frac{U_\infty}{2\upsilon x}}$	similarity variable
$\overrightarrow{E}$	electric field	$\theta = \frac{T-T_\infty}{T_w-T_\infty}$	dimensionless temperature

References

1. Soundalgekar Patil, M. R. and Takhar, H. S.: MHD flow past a vertical oscillating plate. *Nuclear Engineering and Design*, **64**, (1981), 43-48.

2. Agrawal, H. L., Ram, P. C. and Singh, S. S.: Combined buoyancy effects of thermal and mass diffusion on mhd natural convection flows. *Canadian Journal of Chemical Engineering*, **58**, (1980), 131-133.
3. Georgantopulos, G. A.: Effects of free convection on the hydromagnetic accelerated flow past a vertical porous limiting surface. *Astrophysics and Space Science*, **65**(2), (1979), 433-441.
4. Raptis, A. and Singh, A. K.: Rotation effects on MHD free convection flow past an accelerated vertical plate. *Mech. Res. Communication*, **12**(1), (1985), 31-40.
5. Raptis, A.: Flow through a porous medium in the presence of a magnetic field. *Int. J. Energy Research*, **10**, (1986), 97-100.
6. Sparrow, E. M. and Gregg, J. L.: Buoyancy effects in forced convection flow and heat transfer. *ASME, J. Appl. Mech.*, **26**, (1959), 133-134.
7. Lloyad, J. R. and Sparrow, E. M.: Combined forced and free convection flow on vertical surface. *Int. J. Heat and Mass Transfer*, **13**, (1970), 434-438.
8. Wilks, G.: Combined forced and free convection flow on vertical surfaces. *Int. J. Heat and Mass Transfer*, **16**, (1973), 1958-1964.
9. Chen, J. L. S.: Natural convection from needles with variable wall heat flux, *J. Heat Transfer*, **105**, (1983), 403-406.
10. Tingwei, G., Bachrum, R. and Dagguent, M.: Influence de la convection naturelle sur la convection forcee au-dessus dune surface plane verticale soumise a un flux de rayonnement, *Int. J. Heat and Mass Transfer*, **25**(5-8) , (1982), 1061-1065.
11. Raju, M. S., Liu, X. R. and Law, C. K.: A formulation of combined forced and free convection past horizontal and vertical surfaces. *International Journal of Heat and Mass Transfer*, **27**(9-12), (1984), 2215-2224.
12. Bestman, A. R.: Natural convection boundary layer with suction and mass transfer in a porous medium. *International J. Energy Resch.*, **14**, (1990), 389-396.
13. Bestman, A. R.: The boundary layer flow past a semi-infinite heated porous plate for a two-component plasma. *Astrophysics and Space Science*, **173**, (1990), 93-100.
14. Raptis A. and Perdikis, C.: Unsteady flow through a porous medium in the presence of free convection. *Int. Comm. Heat Mass Trans.*, **12**, (1985), 697-704 .
15. Sattar M. A.: Free and forced convection flow through a porous medium near the leading edge. *Astrophysics and Space Science*, **191**, (1992), 323-328.
16. Sing and Dikshit.: Hydromagnetic flow past a continuously moving semi-infinite plate for large suction. *Astrophysics and Space Sci.*, **148**, (1988), 249-256.
17. Soundalgekar, V. M. and Takhar, H. S.: MHD forced and free convection flow past a semi-infinite plate. *AIAA Journal*, **15**, (1977), 457-458.
18. Sattar M.A.: Free and forced convection boundary layer flow through a porous medium with large suction. *International Journal of Energy Research*, **17**, (1993), 1- 7.
19. Schichting, H.: *Boundary Layer Theory.* McGraw Hill Book Co., New York, 1968.
20. Narain, J. P. and Uberoi, M. S.: Forced heat transfer over thin needles. *J. Heat Transfer*, **94**, (1972), 240-242.

Journal of Computational and Applied Mechanics, Vol. 6., No. 1., (2005), pp. 27–37

NONLINEAR HYDROMAGNETIC FLOW, HEAT AND MASS TRANSFER OVER AN ACCELERATING VERTICAL SURFACE WITH INTERNAL HEAT GENERATION AND THERMAL STRATIFICATION EFFECTS

Ramasamy Kandasamy
Department of Mathematics, Institute of Road and Transport Technology
Erode-638 316, India
kandan_kkk@yahoo.co.in

Karuppannan Periasamy
Institute of Road and Transport Technology
Erode-638 316, India
kp_trtt@yahoo.co.in

[Received: April 22, 2003]

Abstract. The study of heat and mass transfer on nonlinear hydromagnetic flow is of great practical importance to engineers because of its almost universal occurrence in many branches of science and engineering and hence a large amount of research work has been reported in this field. In particular, the study of heat and mass transfer with heat source and thermal stratification is of considerable importance in chemical and hydrometallurgical industries and this work deals with a problem of such study. Steady flow of an incompressible, viscous, electrically conducting and Boussinesq fluid over an accelerating vertical plate with heat source and thermal stratification effect is considered in the presence of an uniform transverse magnetic field. The problem is considered to be of MHD laminar boundary layer type. The similarity transformation has been utilized to convert the governing partial differential equations into ordinary differential equations and then the numerical solution of the problem is drawn using R.K.Gill method. The velocity, temperature and concentration of the fluid are shown graphically to observe the effects of parameters entering the problem. Finally a sufficient discussion of different results is presented.

Mathematical Subject Classification: 80A20, 76W05
Keywords: heat and mass transfer, hydromagnetic flow, laminar boundary layer, similarity transformation

1. Introduction

Mixed convection flow occurs frequently in nature. The temperature distribution varies from layer to layer and these types of flows have wide applications in industry, agriculture and oceanography. Further, they are especially used in dyeing-industries.

One of the most significant types of flow which has many practical applications in industrial manufacturing processes is the boundary layer behavior over a continuous moving solid surface. For example, heat treated material travelling on a conveyor belt possesses the characteristics of a continuous moving surface.

Heat and mass transfer for an electrically conducting fluid flow under the influence of a magnetic field is considered to be of significant importance due to its application in many engineering problems such as nuclear reactors and those dealing with liquid metals. MHD flows have been of much interest to the engineering community only since the introduction of liquid metal heat exchangers, whereas the thermal instability investigations are directly applicable to the problems in geophysics and astrophysics.

The effects of power-law surface temperature and power-law surface heat flux in the heat transfer characteristics of a continuous linear stretching surface were investigated by Chen and Char [1]. Processes involving the mass transfer effect have long been recognized as important, principally in chemical processing equipment. Crane [2], Vlegger [3] and Gupta and Gupta [4] analyzed the temperature distribution for the problem of a stretching surface. Georgantopoulos et. al [5]have studied the effects of free convection and mass transfer in a conducting liquid, when the fluid is subjected to a transverse magnetic field. Recently, Acharya et. al [6] have studied heat and mass transfer on an accelerating surface subjected to both power-law surface temperature and power-law heat flux variations with a temperature dependent heat source in the presence of suction and blowing.

2. Nomenclature

B_o^2	Magnetic field of strength	P_r	Prandtl number
C	Species concentration in the fluid	R_e	Reynolds number
C_∞	Species concentration in the fluid away from the surface	S_c	Schmidt number
C_w	Species concentration near the surface	T_w	Temperature of the wall
c_p	Specific heat at constant pressure	T_∞	Temperature far away from the wall
D	Chemical molecular diffusivity	u, v	Velocity components
g	Acceleration due to gravity	α	Thermal diffusivity
G_r	Grashof number	β	Coefficient of volumetric thermal expansion
G_c	Modified Grashof number	ν	Kinematic viscosity
K	Thermal conductivity	ρ	Density of the fluid

Heat and mass transfer on MHD laminar boundary-layer flow over an accelerating surface with internal heat source and thermal stratification effects is investigated in the present work. The fluid is assumed to be viscous, incompressible and electrically conducting with a magnetic field applied transversely to the direction of the flow. The similarity transformation has been utilized to convert the governing partial differential equations into ordinary differential equations and then the numerical solution of the problem is drawn using R.K.Gill method. This method has the following advantages over other available methods: (i) It utilizes less storage registers. (ii) It controls the growth of rounding errors and is usually stable. (iii) It is computationally economical. In the absence of chemical reaction and magnetic effects, the results are in excellent agreement with those in [6]. Numerical calculations for different values of dimensionless parameters entering the problem under consideration are carried out for the purpose of illustrating the results graphically. Examination of such flow models reveals the influence of the Schmidt number, thermal stratification and magnetic field on flow field.

3. **Mathematical analysis**

Consider a steady, viscous, incompressible and electrically conducting fluid flowing over an accelerating surface in the presence of a temperature dependent heat source. The problem is considered to be of laminar boundary layer type and two-dimensional. According to the coordinate system, the x-axis is parallel to the vertical surface and the y-axis is chosen normal to it. A transverse magnetic field of strength B_o is applied parallel to the y-axis. The fluid properties are assumed to be constant in a limited temperature range. The concentration of species far from the wall, C_∞ is infinitesimally very small [8] and hence the Soret and Dufour effects are neglected. The physical properties ρ , μ and D are constant throughout the fluid. In writing the following equations, it is assumed that the induced magnetic field, the external electric field and the electric field due to the polarization of charges are negligible. Under these conditions, the governing boundary layer equations of momentum, energy and diffusion for free convection flow with Joule's dissipation (neglecting viscous dissipation) and under Boussinesq's approximation are:

$$\frac{\partial u}{\partial x} + \frac{\partial v}{\partial y} = 0 \,, \tag{1}$$

$$u\frac{\partial u}{\partial x} + v\frac{\partial v}{\partial y} = v\frac{\partial^2 u}{\partial y^2} + g\beta\left(T - T_\infty\right) + g\beta^*\left(C - C_\infty\right) - \frac{\sigma B_o^2}{\rho}u \,, \tag{2}$$

$$u\frac{\partial T}{\partial x} + v\frac{\partial T}{\partial y} = \alpha\frac{\partial^2 T}{\partial y^2} + \frac{\beta_1 u}{\rho c_p}\left(T_\infty - T\right) \,, \tag{3}$$

$$u\frac{\partial C}{\partial x} + v\frac{\partial C}{\partial y} = D\frac{\partial^2 C}{\partial y^2} \,. \tag{4}$$

The boundary conditions are

$$\begin{array}{llll} u = ax\,, \quad v = 0\,, & C = C_\infty + A_o x^r\,, & T = T_\infty + A_1 x^r & \text{at} \quad y = 0\,; \\ u = 0\,, & C = C_\infty\,, & T = T_\infty(x) = (1-n)T_o + nT_w(x) & \text{at} \quad y \to 0\,; \end{array} \tag{5}$$

where n is constant, such that $0 \leq n < 1$. The parameter n is defined as thermal stratification parameter and is equal to $m_1/(1+m_1)$ – see [7] – where m_1 is a constant. T_o is a constant reference temperature, say $T_\infty(0)$. The suffixes w and ∞ denote surface and ambient conditions, a is a constant and r is the temperature parameter.

A_o, A_1 and β are also constants, β is the volumetric coefficient of thermal expansion, β^* is the volumetric coefficient with concentration and σ is electrical conductivity.

We introduce the following new variables

$$\Psi(x,y) = (\upsilon a)^{1/2} f(\eta) \ , \qquad \eta(x,y) = y\sqrt{\frac{a}{\upsilon}} \,, \tag{6}$$

where $f(\eta)$ is the dimensionless stream function. If the velocity components are given by

$$u = \frac{\partial \Psi}{\partial y} \,, \qquad v = -\frac{\partial \Psi}{\partial x} \tag{7}$$

one can easily verify that the continuity equation (1) is identically satisfied and thus the concentration of species far from the wall is infinitesimally small. The following non-dimensional quantities are introduced

$$\theta = \frac{T - T_\infty}{T_w - T_\infty} \,, \tag{8}$$

$$\phi = \frac{C - C_\infty}{C_w - C_\infty} \,, \tag{9}$$

$$\delta = \frac{\beta_1}{\rho c_p} x \qquad \text{(longitudinal coordinate)} \,, \tag{10}$$

$$R_e = \frac{U}{\sqrt{a\upsilon}} \qquad \text{(Reynolds number)} \,, \tag{11}$$

$$G_r = \frac{\nu g \beta}{U^3} (T_w - T_\infty) \qquad \text{(Grashof number)} \,, \tag{12}$$

$$G_c = \frac{\nu g \beta^*}{U^3} (C_w - C_\infty) \qquad \text{(modified Grashof number)} \,, \tag{13}$$

$$P_r = \frac{\mu c_\rho}{k} \qquad \text{(Prandtl number)} \,, \tag{14}$$

$$S_c = \frac{\upsilon}{D} \qquad \text{(Schmidt number)} \,, \tag{15}$$

$$M^2 = \frac{\sigma B_o^2}{\rho c K^2} \qquad \text{(magnetic parameter)} \,. \tag{16}$$

Making use of equations (6)–(16) we obtain from equations (2)–(4) that

$$f''' + G_c R_e \phi + G_r R_e \theta + f f'' - (f')^2 - \frac{M^2}{R_e}(1 - f') = 0 \,, \tag{17}$$

$$\theta'' - P_r \left(\theta - \frac{n}{1-n} \right) f' - P_r \theta (r + \delta) f' + P_r f \theta' = 0 \,, \tag{18}$$

$$\phi'' - S_c f' \phi r + S_c f \phi' = 0 \,. \tag{19}$$

These equations are associated with the following boundary conditions

$$\begin{array}{llll} f(0) = 0 \,, & f'(0) = 1 \,, & \phi(0) = 1 \,, & \theta(0) = 1 \,, \\ f'(\infty) = 0 \,, & & \phi(\infty) = 0 \,, & \theta(\infty) = 0 \,. \end{array} \tag{20}$$

Equations (17) to (19) with boundary conditions (20) are integrated using the Runge-Kutta Gill method. Results of the problem are obtained for different values of the

Schmidt number, magnetic and thermal stratification parameters and they are discussed in detail in the following section.

4. **Results and discussion**

In order to get a clear insight of the physical problem, numerical results are displayed with the help of graphical illustrations. In the absence of chemical reaction and magnetic effects, the results have been compared with those in a previous work [6] and it is found that they are in good agreement. The numerical results we have obtained are illustrated by means of Figures 1-12.

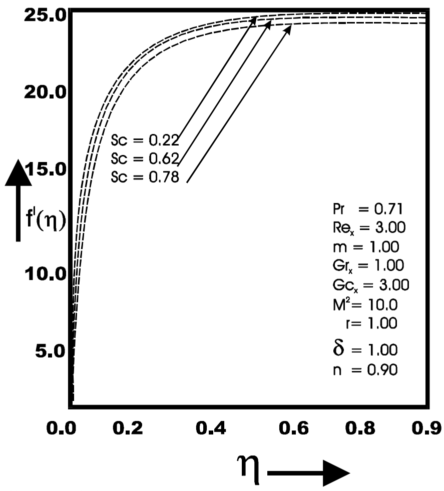

Figure 1. Effect of Schmidt number over the velocity profiles

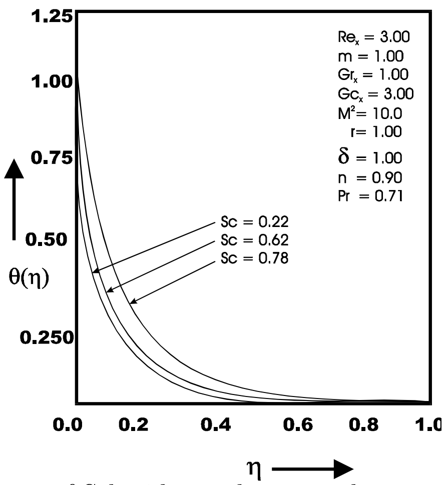

Figure 2. Influence of Schmidt number over the temperature profiles

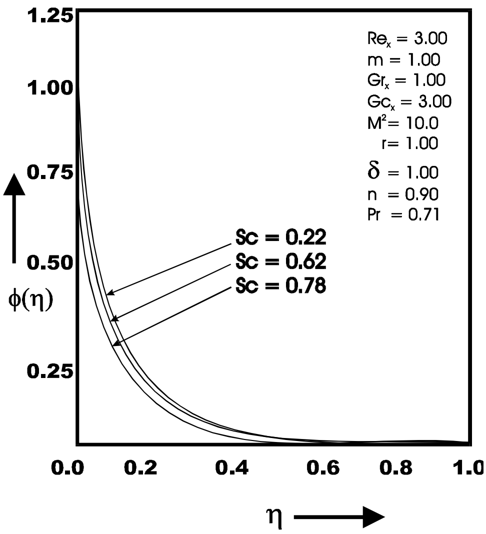

Figure 3. Effects of Schmidt number over the concentration profiles

In the presence of a uniform thermal stratification parameter with constant magnetic field, it is clear that the velocity and the concentration decrease and the temperature of the fluid increases with increase of the Schmidt number and these are displayed through the Figures 1, 2 and 3, respectively.

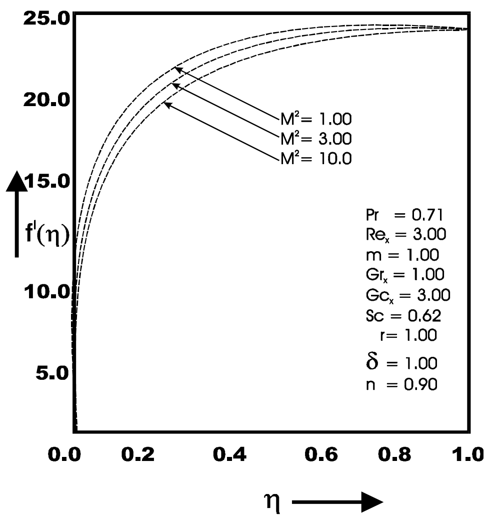

Figure 4. Influence of magnetic field over the velocity profiles

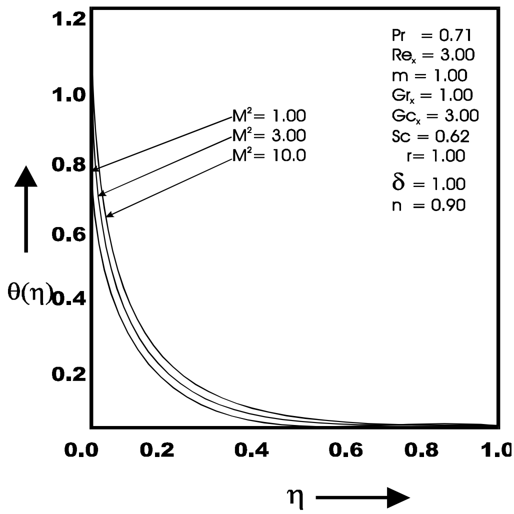

Figure 5. Effect of magnetic field over the temperature profiles

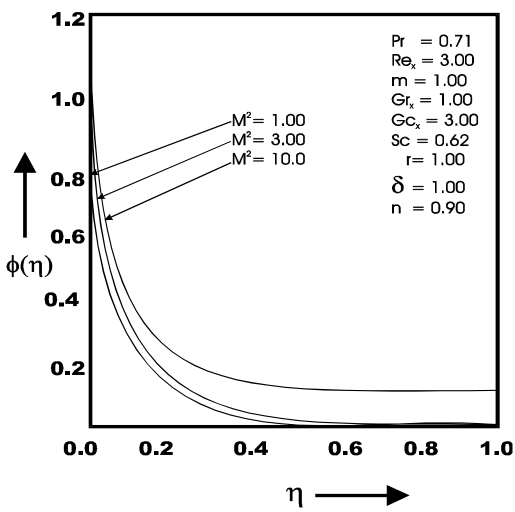

Figure 6. Influence of magnetic field over the concentration profiles

In the presence of a uniform Schmidt number and thermal stratification parameter, it is seen that the increase in the strength of a magnetic field, leads to a fall in the velocity of the fluid and a rise in the temperature and concentration of the fluid along the accelerating surface and are shown in Figures 4, 5 and 6, respectively.

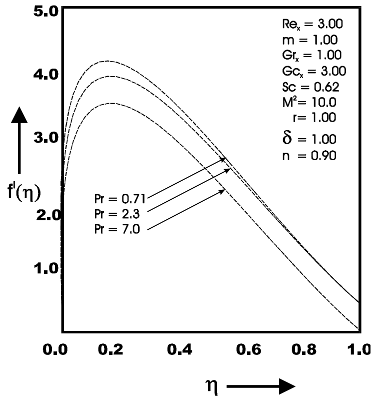

Figure 7. Effect of Prandtl number over the velocity profiles

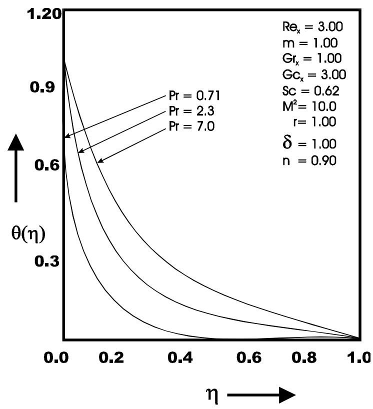

Figure 8. Influence of Prandtl number over the temperature profiles

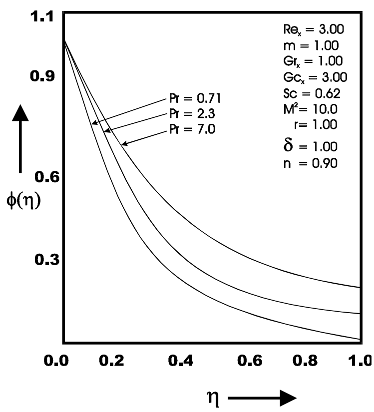

Figure 9. Effect of Prandtl number over the concentration profiles

Figure 7 depicts the dimensionless velocity profiles for different values of the Prandtl number with constant Schmidt number and magnetic field. It is observed that the velocity of the fluid decreases. The temperature and concentration of the fluid increase along the accelerating surface with increase of the Prandtl number and these are displayed through Figures 8 and 9.

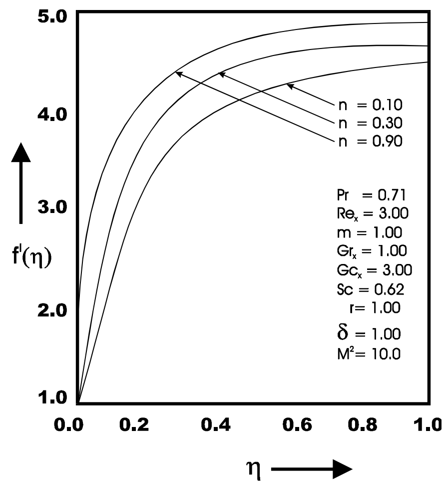

Figure 10. Effect of thermal stratification over the velocity profiles

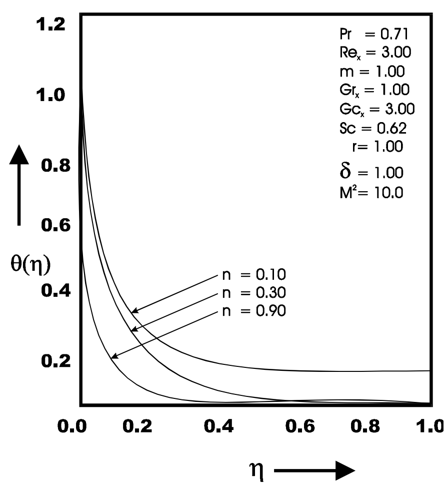

Figure 11. Influence of thermal stratification over the temperature profiles

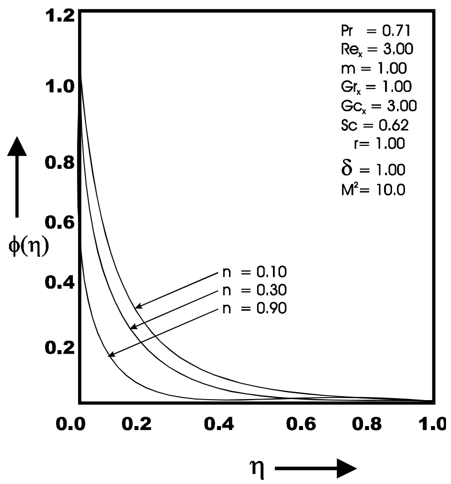

Figure 12. Effect of thermal stratification over the concentration profiles

In the case of the constant Schmidt number with a uniform magnetic field, it is observed that the increase of thermal stratification parameter accelerates the fluid motion and decelerates the temperature and concentration of the fluid along the accelerating surface and these are vivid through Figures 10, 11 and 12, respectively.

5. **Conclusions**

- In the presence of a uniform Schmidt number and magnetic field, the velocity decreases and the temperature and concentration of the fluid increase with an increase of the Prandtl number.
- Due to the constant thermal stratification parameter with a uniform magnetic field, the velocity and the concentration decrease and the temperature of the fluid increases with an increase of the Schmidt number.
- An increase in the strength of a magnetic field leads to a fall in the velocity and rise in the temperature and concentration of the fluid along the surface.
- The velocity increases and the temperature and concentration of the fluid decrease with increase of the thermal stratification parameter.
- In the presence of water vapour ($S_c = 0.62$) and the uniform magnetic field, it is noted that the velocity of the fluid increases and the temperature and concentration of the fluid decrease near the plate, respectively.
- In the presence of air ($P_r = 0.71$), it is interesting to note that the velocity of the fluid increases near the plate and thereafter decreases.
- The temperature and concentration of the fluid decrease at a very fast rate in the case of water ($P_r = 7.0$) in comparison to air ($P_r = 0.71$).
- In the case of a uniform thermal stratification parameter, it is noted that the velocity of the fluid increases and the temperature and concentration of the fluid decrease at a fast rate near the plate.

- In the presence of a uniform magnetic field and air ($P_r = 0.71$), the velocity of the fluid increases due to an increase in S_c showing that it decreases gradually as it is replaced by hydrogen ($S_c = 0.22$), by water vapor ($S_c = 0.62$) and ammonia ($S_c = 0.78$).
- The temperature and concentration decrease due to increase in Sc indicating that it increases as it is replaced by hydrogen ($S_c = 0.22$), by water vapor ($S_c = 0.62$) and ammonia ($S_c = 0.78$).

References

1. Chao-Kuang Chen and Ming-I Char: Heat transfer of a continuous stretching surface with suction or blowing. *Journal of Applied Mathematics and Physics*, **135**, (1988), 568-580.
2. Crane, L.J.: Flow past a stretching plate. *Angewandte Zeitschrift für Mathematik and Physik*, **21**, (1970), 645-657.
3. Vlegger, J.: Laminar boundary layer behavior on continuous accelerating surfaces. *Chemical Engineering Science*, **32** (1977), 1517-1529.
4. Gupta, P.S. and Gupta, A.S.: Heat and mass transfer on a stretching sheet with suction or blowing. *The Canadian Journal of Chemical Engineering*, **55**, (1977), 744-746.
5. Georgantopoulos, G.A.: Free convective and mass transfer in a conducting liquid. *Astrophysics Space Science*, **74**, (1981), 359-371.
6. Acharya, M., Singh, L.P. and Dash, G.C.: Heat and mass transfer over an accelerating surface with heat source in presence of suction/blowing. *International Journal of Engineering Science*, **37**, (1999), 189-201.
7. Akira Nakayama and Hitoshi Koyama: Similarity solutions for buoyancy induced flows over a non-isothermal curved surface in a thermally stratified porous medium. *Applied Scientific Research*, **46**, (1989), 309-314.
8. Byron B,R., Stewart W.E. and Lightfoot E.N.: *Transport phenomena*, New York, John Wiley and Sons, 1992.

Journal of Computational and Applied Mechanics, Vol. 6., No. 1., (2005), pp. 39–52

SHAPE FINDING OF AN EXTREMELY TWISTED RING

Zsolt Gáspár[1,2], Robert Németh[1,3]
[1]Department of Structural Mechanics
[2]HAS Research Group for Computational Structural Mechanics
[3]Center for Applied Mathematics and Computational Physics
Budapest University of Technology and Economics
H-1521 Budapest, Műegyetem rkp. 3., Hungary
gaspar@ep-mech.me.bme.hu, nemeth.robert@gmx.net

[Received: June 2, 2004]

Abstract. The Kirchhoff rod is a widely used model in describing configurations of DNA chains. In the simplest case of such research the molecule-chain is represented by a twisted-bent rod. In this paper we will present an application of this rod model for describing the shapes of the DNA chain in a special configuration. Here, two finite segments of the rod are in contact with each other. The contact region is closed on each end by terminal loops. These configurations can be represented by four parameters. The equilibrium path is computed in the four-dimensional space of the parameters using the path-following simplex method. The paper shows the system of equations applied during the path-following, equilibrium path from a generalized solution, and some numerical results with different rod lengths. At last we show how our results should be connected to configurations of former research.

Mathematical Subject Classification: 70G45
Keywords: twisted ring, large displacements, DNA

1. Introduction

Let us consider an initially straight rod a with circular cross-section of radius r. The rod is long, i.e. $L >> r$, where L is the length of the rod. The rod is made of a homogenous, linearly elastic material with the modulus of elasticity E and the shear modulus of elasticity G. Bending stiffness is characterized by the constant $A = EI_x$, where $I_x = \frac{r^4\pi}{4}$, and the twist stiffness by $C = GI_p$, where $I_p = \frac{r^4\pi}{2}$. The rod is supposed to be inextensible and unshearable. First, the rod is bent to a ring with a pair of moments acting on the end-sections. Then the end-sections are twisted in the opposite direction, while they stay in contact. By a small twist rate the ring holds its planar shape. Above a critical value of twist, the ring loses its stability, and the rod takes a spatial shape. The critical value of twist rate was first estimated by Zajac [1]. Dichmann et al. [2] presents critical values even for overlapping rings. Another, symmetry-based examination of all configurations of self-penetrable rods was presented by Domokos [3]. If the rod is impenetrable, self-contact can arise. The contact may destroy some symmetry properties of the solutions. The self-contact can arise in contact points, or along a contact-line. Coleman et al. [4] determined equilibrium paths of the rod with self-contact, with detailed analysis of the stability of solutions. In addition to the classification of different contact configurations, Swigon et al. [5] derived the differential equation of the generalized helix, which occurs in the case of self-contact along a line, and its analytical solution. An extension of their work was made by Thompson et al. [6], where the generalized helix is loaded by a wrench.

In the above mentioned research the elastic rod is treated as a continuous mechanical model of DNA molecules, where the rod axis is equivalent to the duplex axis of the DNA. This modelling is validated through similarity between computed rod shapes and real DNA configurations taken from electron-microscope photos.

In this paper we want to give an extension to the former results. The first configuration on the first non-trivial equilibrium path of the impenetrable rod has one point of contact. In a contact point a concentrated contact force arises. This configuration is denoted by A_1, where A means the first non-trivial path, while 1 is the number of contact point(s). The following shapes on this path have 2 and 3 contact points, these are denoted by A_2 and A_3. Further increasing of the twist leads to the A_4 configuration. The A_4 configuration differs from the previous configurations in a contact line between the inner contact points. In the contact line a distributed contact force arises. However, a contact line contains an infinite number of contact points. We refer to a point as a contact point only if there a concentrated (finite) force arises. Further increasing of the twist rate leads to a longer contact line, while the free segment between the outer and inner contact points decreases, so does the length of the terminal loop. We suspect that at extreme high twist the free segment disappears. Then we will have a configuration with two contact points, but, unlike the A_2 configuration, there will be a contact line between the contact points. So, we will refer to this configuration as A_{2+}. Our goal is to find the equilibrium path of this configuration. We do not deal with the stability of the solutions.

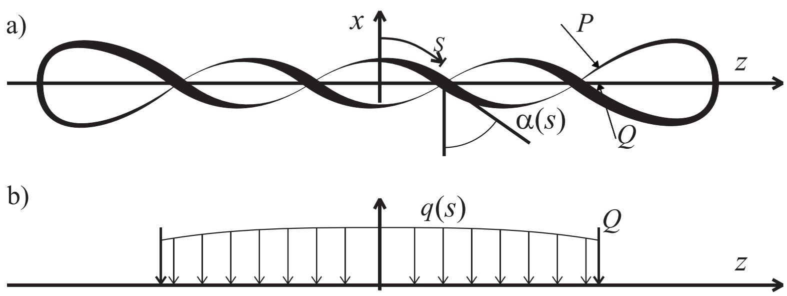

Figure 1. (a) Sketch of the analyzed configuration with the global reference system. (b) Intensity of the assumed distributed ($q(s)$) and concentrated (Q) contact forces along the contact line

The axis of an A_{2+} configuration is sketched in the Figure 1a. The configuration is symmetric to the contact line, we refer to this axis by z. We set its 0 to the middle of the contact line. So, the rod axis crosses the plane $z = 0$ in two points. Through these points goes axis x, which is also an axis of symmetry. The third axis of our reference system will be axis y. The coordinate system $[xyz]$ is a right-handed one, therefore axis y points out of the plane in Figure 1a.

Every configuration can be represented by the space curve of the rod axis. This curve will be given by the co-ordinates in the system $[xyz]$, as a function of the arc length s. The point $s = 0$ should be where the rod axis crosses the plane $z = 0$ at a positive value of x. The rod is directed in such a way that a small increase in the arc-length parameter leads to a point in the positive eighth of the reference system. (This happens if we twist the rod in clockwise direction.) In the contact region the rod axis describes a generalized helix. The rise angle ($\alpha(s)$) of this helix depends on s, and is defined as the angle between the tangent of the rod axis and a plane normal to z. In the examined configuration it is sufficient to examine the segment from $s = 0$ to $s = L/4$. The last point is the top of the closing loop on the right side.

We divide the examined part of the A_{2+} configuration into two different parts. The first is the helix, where the rod is in contact with another part of the rod. On the contact line arises the distributed contact force $q(s)$, which points from axis z to the rod axis. The last cross-section of contact is at the arc-length s_P. The second part is the terminal loop. In the loop there are no external forces acting on the rod. At the common boundary of these two parts a concentrated contact force (Q) arises (Figure 1b.).

In Section 2 we will show the differential equations used for finding a rod shape, then, in Section 3 we will present the equation system to be solved for the equilibrium path. In Section 4 the applied numerical methods of computation will be introduced. Numerical results and their conclusions will be presented in Section 5.

2. Differential equations applied

2.1. **Differential equation of the generalized helix.** The differential equation of the generalized helix is derived from the geometrical, equilibrium and constitutive equations of the rod. The whole derivation can be found in [5], [6] and [7], interested readers are directed to those works. Here we only present the start-up and the definitions of the terms used.

The turn of the rod around the contact line is measured through the function $\varphi(s)$, as it is shown in Figure 2a. So the co-ordinates of the rod axis at the arc-length s are:

$$\mathbf{r}(s) = \begin{bmatrix} r \cdot \cos\varphi(s) \\ r \cdot \sin\varphi(s) \\ z(s) \end{bmatrix}.$$

Figure 2b helps us to write the first and second derivatives of $\mathbf{r}(s)$. The length of the latter is the curvature of the curve.

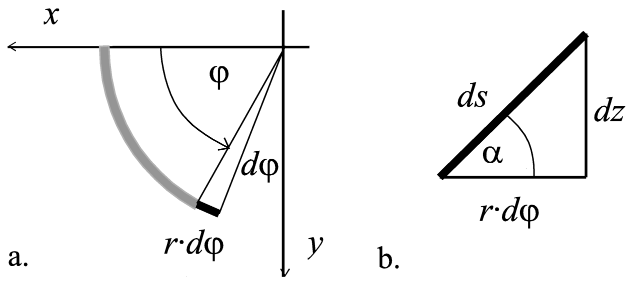

Figure 2. Geometry of generalized helix. View of an elementary segment (a) from axis z (b) from a radial direction

The simplest way of writing the six differential equations of equilibrium is to use a cylindrical reference system. We have only three equations of material behavior, because the effect of normal and shear forces is neglected. The first one is the relationship between the twist ω and the torque M_T:

$$\omega = \frac{M_T}{C}, \tag{2.1}$$

the second one describes the relationship between the curvature κ and the bending moment M_B

$$\kappa = \frac{M_B}{A}, \tag{2.2}$$

and the third one states that the moment vector $\mathbf{M}$ is orthogonal to the principal normal vector $\mathbf{r}''$:

$$\mathbf{M} \cdot \mathbf{r}'' = 0, \tag{2.3}$$

where $'$ denotes differentiation with respect to s.

From these equations one can derive the differential equation of the generalized helix:

$$0 = \alpha''' + \alpha' \frac{2r^2\alpha'' \sin 2\alpha + 8\cos^6\alpha - 12\cos^4\alpha + 6\cos^2\alpha}{r^2 \cos 2\alpha}. \tag{2.4}$$

This differential equation can be written in a second order form, where the constant torque appears as a free parameter:

$$\alpha'' = \frac{M_T \cdot \cos 2\alpha}{A \cdot r} - \frac{\sin 2\alpha \cdot \cos^2\alpha}{r^2}. \tag{2.5}$$

2.2. **System of differential equations of a free segment.** In the case of a free segment the first step of the computation of the shape (namely the function $\mathbf{r}(s)$) is to compute the inner forces and moments. There are no external forces acting on the rod, so the equilibria of a segment of arbitrary length causes the resultant of the inner forces to be constant along the segment. This resultant will be reduced to the origin of the reference system, and the force and moment components will be denoted by vectors $\mathbf{P}_0$ and $\mathbf{M}_0$. The effect of normal and shear forces is neglected, so we need the moments in the cross-sections only. Their vector can be computed by the form:

$$\mathbf{M}(s) = \mathbf{M}_0 + \mathbf{P}_0 \times \mathbf{r}(s). \tag{2.6}$$

It is a well-known fact that the torque and the specific twist are constant in the initially straight rod of homogenous cross-section. So the twist of a segment can be computed from the specific twist and the length. The bending part of the moment vector causes a change in the tangent of the rod, which can be computed from:

$$\mathbf{r}^{''}(s) = \frac{1}{A}\mathbf{M}(s) \times \mathbf{r}^{'}(s). \tag{2.7}$$

3. Closing conditions of rod

3.1. **Equation system of closing.** We use the symmetry of the rod in our computation, so we examine only a quarter of the whole rod. The shape of a rod can be specified by four parameters. Three of these parameters are connected to the helix, the fourth parameter belongs to the contact point. In the point $s = 0$ the initial value of the rise angle (α_0) and its first and second derivatives ($\alpha_0^{'}$ and $\alpha_0^{"}$) determine the shape of the helix. The symmetry causes $\alpha_0^{'} = 0$, so here we have only α_0 and $\alpha_0^{"}$ as free initial values. The third parameter of the helix is its length, denoted by s_P. The fourth parameter is the concentrated contact force Q at the end of the helix. The function of the inner forces in the helix can be computed from the three parameters α_0, $\alpha_0^{"}$ and s_P, their radial force component is modified at the end point by Q.

Any set of the above parameters allows the computation of a rod shape. First the helix-form must be computed as an initial value problem from $s = 0$ up to $s = s_P$. Then the radial component of the inner forces must be modified by Q, and the system of differential equations of the closing loop must be solved until $s = L/4$. The parameters lead to a closed rod, if this point is the top of the loop, namely the rod crosses axis z in this point orthogonally. This can be mathematically formulated with three equations: $x(L/4) = 0$, $y(L/4) = 0$ and $z^{'}(L/4) = 0$.

(Note: The helix has a third-order differential equation, so the whole helix can be defined by four values, the length of the helix and three initial values. The same helix could be defined by other values, for example by the length, the rise angle in the end points, and the first derivative in the start-point. Naturally, the latter must be equal to zero, as before.)

3.2. **Possible shapes.** On the basis of the previous subsection, four parameters define a rod shape. We call this rod shape a mathematically possible solution, if the three equations for closing are satisfied.

Physically acceptable solutions are those mathematically possible solutions for which the following conditions are fulfilled:

- the rod does not cross itself,
- no tension arises in contacts.

The first condition is satisfied, if the largest curvature is smaller than the reciprocate of the radius of the rod, and the rise angle of the helix causes no self-intersection (which in [8] occurs at $\alpha = 45°$). The second condition means, that Q and the minima of q cannot be negative.

4. Numerical method of solution

The first step of the solution is to find the mathematically possible shapes, then the physically unacceptable solutions will be filtered out. The units of lengths and forces are chosen to have $r = 1$ and $A = 1$.

4.1. **The Path-Following Simplex Algorithm.** In order to determine the mathematically possible shapes, we have to find the common zero places of $n-1 = 3$ functions, depending on $n = 4$ parameters. The number of functions and parameters suggests that the solution set is a one dimensional set in the space of parameters. This type of problems can be easily solved by the Path-Following Simplex Algorithm [9]. We set a simplex in the space of the parameters with one side over a known solution. Then we compute the values of the error-functions (the left sides of the closing equations, i.e. $x(L/4)$, $y(L/4)$ and $z^{'}(L/4)$) in the vertices of the simplex and interpolate them. So, each function will have a solution set of $n-1$ dimensional hyperplane. The common crossing line of these planes will be a line. This way we linearize the solution. The linearization gives a good approximation of the solution inside the simplex. The linearized solution crosses two simplex sides. One side is where the known result lies, the other one is a new solution point. We mirror the simplex on this side, then we have a new simplex with a solution on one of its sides. Now we can linearize the solution inside this simplex, just as we did with the previous one, but now we have to compute the error-functions in only one vertex, because the mirroring does not change the position of the mirroring side. The persistent use of the above steps leads to a whole solution (or, at least its good approximation by a piecewise linear curve).

The path following requires a starting point. Domokos and Szeberényi [10] present a method, where the path following is combined with scanning the parameter space. We can also fix the value of one parameter, then, an iterative method provides one solution point of the equation system. The drawback of this method is that a change in the length of the rod causes change in the initial solution.

A different reading of parameters can result an universal solution point. If the rise angle of the helix is constant (providing $\alpha_0 = \alpha_P$), then the internal forces and moments are also constant. So they do not depend on the length of the helix, and the terminal loop is also independent of L. In other words, the value of s_P changes, but $L/4 - s_P$ remains unattended. So we have to compute the free segment of length $L/4 - s_P$ connecting to a helix of constant rise angle α_0 with the inner forces determined by the helix and the modifier contact force Q. The three variables mentioned above have to be computed according to the connecting equations.

The problem can be solved even with two unknown parameters only, if we compute the free segment until the third equation, namely $z^{'}(L/4) = 0$ comes true. Then we only have to solve the equation system $x = 0$, $y = 0$ for the variables α_0 and Q, while $L/4 - s_P$ will be the arc-length, belonging to the solution. The result of this computation is:

$$\alpha_0 = 0.9733982, \qquad L/4 - s_P = 3.5773973, \qquad Q = 0.3212820.$$

These data determine the starting point of the path following. But this starting point is only a mathematically possible solution, because on the top of the loop the rod would have too high a curvature. This would lead to an overlap at the top of the loop, as can be seen in Figure 3.

Figure 3. The physically non-acceptable terminal loop at universal starting point

4.2. **Finite differences of variable length.**

4.2.1. *Reason of using FDVL.* The generalized helix has a third-order differential equation. In order to compute the error-functions of the simplex path-following, one has to solve this differential equation. The analytical solution of the differential equation is given in the paper by Coleman et al. [11]. This solution contains elliptic integrals, and has singularity at our desired starting point and is numerically instable in its neighborhood. That is the reason why we choose a numerical method for solving the boundary value problem of the helix. The helix is then determined through its length s_p, its rise angles in start and end-points (α_0, α_P) and the first derivatives of the rise angle (which is equal to 0). The differential equation can be transformed into a first-order form:

$$(\alpha')^2 = \frac{M_T \cdot \sin 2\alpha}{A \cdot r} + \frac{\cos^4 \alpha}{r^2} - \frac{M_T \cdot \sin 2\alpha_0}{A \cdot r} - \frac{\cos^4 \alpha_0}{r^2}. \tag{4.1}$$

This form contains M_T as an unknown parameter, and satisfies the $\alpha_0' = 0$ condition. From the analytical solution of the helix one can show, that the function $\alpha(s)$ changes monotonous in the interval $[0, s_P]$, so the sign of the first derivatives equals to the difference of $\alpha_P - \alpha_0$. The function does not leave the interval of α_0 and α_P, as another consequence of monotony.

4.2.2. *Computational form of the finite differences.* We divide the interval $s = [0, s_p]$ into N_d sections. The length of the ith section is denoted by Δs_i. The analytic solution shows that the function changes less at small s; a sketch of the function can be found in the paper by Thompson et al. [6]. It is preferable to choose the sections so that the changees of the function over the sections are approximately the same in size. This condition needs longer sections at smaller changes of function and shorter sections at greater changes of function. Let the lengths of sections Δs_i make a geometrical series. The quotient of two consecutive sections' length $\Delta s_{i+1}/\Delta s_i$ is denoted by $q \leq 1$, so the last (the N_dth) section's length is $\Omega = q^{(N_d-1)}$ times the first section's length. So the sum of all sections, i.e. the length of the helix is:

$$s_P = \Sigma_{i=1}^{N_d} \Delta s_i = \Delta s_1 \cdot \Sigma_{i=1}^{N_d} q^{i-1},$$

while the length of first section (Δs_1) is:

$$\Delta s_1 = s_p \cdot \frac{1-q}{1-q^{N_d}} \ .$$

We want to compute the function values α_i in the end-points of the sections. (This notation leaves α_0 unchanged, as a continuation of the series, while at the end of the helix $\alpha_{N_d} = \alpha_P$.) There are $N_d - 1$ unknown α_i values in the divider points, and we do not know M_T yet. One can write $N_d - 1$ equations with the finite differences (one for each divider point), and one more for the start-point of the helix, using the symmetry of function $\alpha(s)$.

We write the difference equation of the ith divider point. The truncated Taylor-series of α at that point is:

$$\alpha(s_i + S) = \alpha_i + \alpha_i' \cdot S + \alpha_i'' \cdot \frac{S^2}{2},$$

so we can write α_{i-1} and α_{i+1}:

$$\alpha_{i-1} = \alpha_i - \alpha_i' \cdot \Delta s_i + \alpha_i'' \cdot \frac{\Delta s_i^2}{2},$$

$$\alpha_{i+1} = \alpha_i + \alpha_i' \cdot \Delta s_i \cdot q + \alpha_i'' \cdot \frac{\Delta s_i^2}{2} \cdot q^2.$$

These lead to the following expression for ${\alpha''}_i$:

$${\alpha_i}'' = \frac{2}{q \cdot (q+1) \cdot \Delta s_i^2} \left(q \cdot \alpha_{i-1} - (q+1) \cdot \alpha_i + \alpha_{i+1} \right),$$

which must be equal to the formula given by (2.5), i.e.

$$M_T \cdot \cos 2\alpha_i - \sin 2\alpha_i \cdot \cos^2 \alpha_i = \tag{4.2}$$

$$= \frac{2}{q \cdot (q+1) \cdot \Delta s_i^2} \cdot \left(q \cdot \alpha_{i-1} - (q+1) \cdot \alpha_i + \alpha_{i+1}\right) \ . \tag{4.3}$$

This equation can be written for $N_d - 1$ points. In the 'zeroth' point a fictitious -1st point helps to write the following equation:

$$M_T \cdot \cos 2\alpha_0 - \sin 2\alpha_0 \cdot \cos^2 \alpha_0 = \frac{2}{\Delta s_1^2} \cdot (\alpha_1 - \alpha_0). \tag{4.4}$$

The helix is computed by the solution of equations (4.2) and (4.4). The N_d equations are solved with an iterative method.

4.2.3. *Iterative solution of the equation system of finite differences.* The function values in the divider points can be set initially in order to make a second order parabola. Initial values of α_i-s will be

$$\alpha_i = \alpha_0 + \left(\frac{\Sigma_{j=1}^{i} \Delta s_j}{s_p}\right)^2 (\alpha_P - \alpha_0),$$

and the initial value of M_T is computed from Eq. (4.4). In every iteration step we change

- α_i-s by the formula

$$\alpha_i^{new} = \frac{q \cdot \alpha_{i-1} + \alpha_{i+1}}{q+1} - (M_T \cdot \cos 2\alpha_i - \sin 2\alpha_i \cdot \cos 2\alpha_i) \cdot \frac{q \cdot \Delta s_i^2}{2}, \tag{4.5}$$

  $i = 1, ..., N_{d-1}$, which was expressed from Eq. (4.2) (where on the right side we use the modified value of α_{i-1}, but the old values of α_i and α_{i+1}),
- M_T from Eq. (4.4).

If the greatest change of α_i-s is smaller than a prescribed limit $\Delta\alpha$, we stop the iteration.

$\alpha^{'}(s)$, $\alpha^{''}(s)$ and the internal forces can be computed at the end-point of the helix from the accepted values of α_i-s.

5. **Numerical results**

5.1. **Equilibrium paths and configurations.** We choose the length of the rod to $L = 244$, and $C = 2/3$, in order to reach comparable results with previous results in [4]. The helix was divided into 250 sections, the quotient of the largest and smallest section was 30, i.e. $q = 30^{-1/249} \approx 0.9864334$. Figure 4. shows two dimensional projections of the mathematically possible solutions. On the upper vertical axes the rise angles are in the middle of the helix, on the lower axes are the lengths of the half-loop. The horizontal axes represent the rise angle at the end-point of the helix on the left side, and the contact force on the right side.

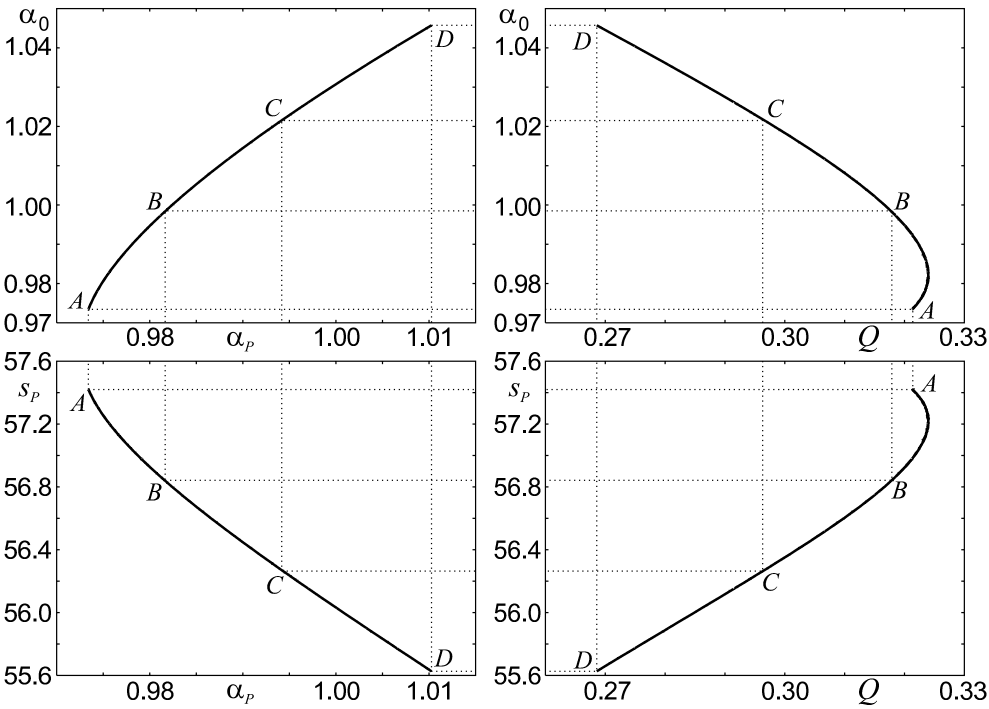

Figure 4. Two dimensional projections of the equilibrium path of the rod with $A = 1$, $L = 244r$.

We mark four points in each diagram. Point A is the starting point of the path following procedure. The smallest curvature is 1 in point B, and the minimum of the distributed contact force is 0 in point D. Physically acceptable shapes belongs to points of segment BD. One example for that is point C.

Figure 5a-d represents four rod shapes from the equilibrium path, namely the configurations in points A, B, C and D, respectively. The series of the presented shapes can be reached through an unloading process during which the twist rate decreases from B to D. (It decreases even from A, but those are physically non-acceptable solutions, hence they are out of our interest.) But the smaller twists are still very high, as the following short computation will show.

We calculate the characteristic values of the space curve of the configuration of Figure 5c. In this configuration the torque equals $M_T = -0.533444$, the rise angle of the helix in its mid-point is $\alpha_0 = 1.021554$ and the arc-length of the helix is $s_P = 56.269746$. The characteristic values are the twist (Tw), the writhe (Wr) and the link (Lk). Their meanings for a space curve and a rod can be found in the works by White [12] and Fuller [13]. The twist can be computed from the torque, and, as

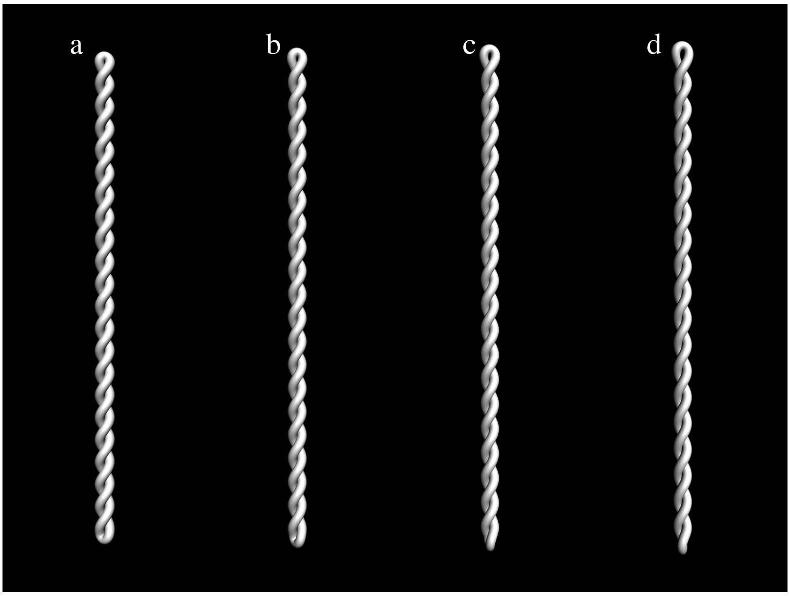

Figure 5. Equilibrium shapes of the rod, corresponding to the points A, B, C, D of the eq. path

already mentioned, it is constant along the rod, so it can be computed via

$$Tw = \frac{M_T}{C}\frac{L}{2\pi} \ . \tag{5.1}$$

C depends on the material of the rod, and until now it has not had any influence on the computation. The earlier mentioned C results $Tw = -31.08$.

The writhe is computed with an approximate method presented by Thompson et al. in [6]. We assume that the bulk of writhe is in the helix, and neglect the writhe that would be computed from the loop. We can also neglect the small change of the rise angle, so we compute the writhe on a helix of constant rise angle α_0 via:

$$Wr = \frac{2s_P \cos^2\alpha_0}{\pi} = -9.77 \ . \tag{5.2}$$

The link number is the measure of the twist of the end sections against each other:

$$Lk = Tw + Wr = -40.85 \ . \tag{5.3}$$

Comparing these results with the graphs of Coleman et al. in [11] one can prove the intuition that our analyzed shapes arise at a very high twist.

5.2. **Connection to former results.** The characteristic values of the configuration D can be computed in the same way, as we did in the previous subsection. Then we had the link number $Lk = -34.05$. In this configuration the minimum of distributed contact force equals zero. Further decreasing of the twist results in the need

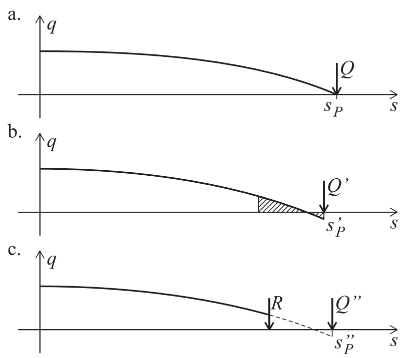

Figure 6. Change of distributed contact forces (a) in D state, (b) in a physically non-acceptable state after decreasing the twist, (c) in a possible new configuration (A_4)

of tensional forces between the strands of the helix. Since this is not a physically acceptable configuration, no A_{2+} configuration exists with a lower link number than configuration D.

We present some theoretical considerations on what kind of configuration may arise if we decrease the twist in state D. The twist of the end-sections against each other is measured with the link number. Decreasing the twist means decreasing the link, i.e. the rod has to change to a new configuration, but this new configuration has nearly the same link number.

The character of the intensity of the distributed contact force is sketched on Figure 6. Configuration D with vanishing contact force at its end is in Figure 6a., while Figure 6b. shows the necessary distribution, when the twist is decreased and we use the same equations. In physically acceptable solutions no negative contact force arises, so a part of the rod will shove off its contacting part. We suspect that the contact ends in the hatched region, and at the end of the remaining contact a second concentrated force arises instead of the contact forces of the hatched region. This force is denoted by R in Figure 6c. That means that the follower configuration in the un-twisting process could have a line contact, closed by the concentrated contact force R, then a skip-fly segment, followed by the force Q'', then it is closed by the terminal loop. In short, this will be an A_4 configuration with link number -34.05.

As we presented the analyzed A_{2+} configuration arises only at very high twist values. In this state a secondary buckled shape is also possible. In the resulting configuration the double helix wraps around itself. This would be the third helical form, as the rod itself is the model of the double-helix of the DNA, it creates the generalized helix we have presented, and the generalized helix produces a more complex helix with a very complicated contact situation.

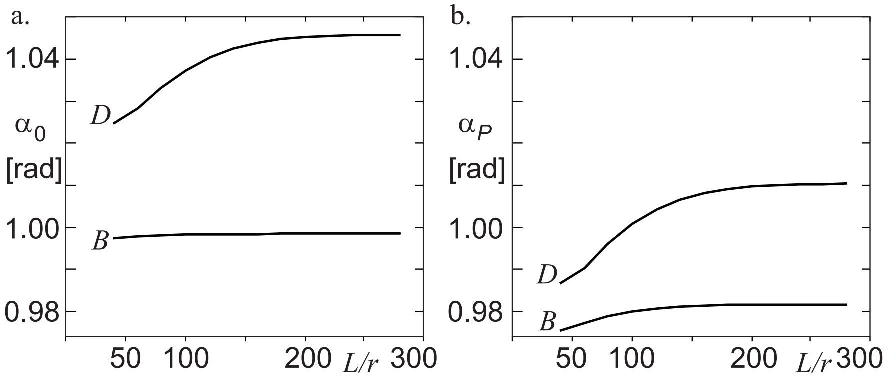

Figure 7. The rise angle in the middle (a) and at the end (b) of the helix in terms of the function of rod length. The upper and lower linse represent states D and B, respectively.

5.3. **Effect of change in the rod length.** We analyzed the effect of rod length. Figure 7 shows two graphs of results. Both graphs present a change of the rise angle as a function of the rod length, Figure 7a at the middle of helix, while Figure 7b at the end. The physically unacceptable universal starting point of path following has a constant value of 0.9733982. From there all angles are increasing until state B, which is the lower graph in both figures. The maximum of attainable angles arises in state D, which are shown by the upper lines.

The rod length was changed between 40 and 280. It can be seen that the interval of physically acceptable states increases with increasing rod length. We can see from the graphs that for long rods the angles vary only by a small value and it seems that all four curves have a horizontal asymptote. This is valid for relatively long rods, where the twisted part is long enough to result in very small derivatives even in case of larger difference between the rise angle in the middle and at the end of the helix. Moreover, the longer the rod is, the longer part of it lies in the helix, in accordance with the assumption made by the approximate computation of the writhe.

In the case $L = 4 \cdot 3.5773973 = 14.3095892$ the length of the contact line would be equal to 0. The un-twisting process should decrease this length, but it cannot be negative, so this is a theoretical lower end of the diagrams. This configuration could also be treated as an A_1 configuration of a short rod. However, this configuration is physically non-acceptable, as its curvature is greater than $1/r$; an unloading process of the rod can reach possible shapes of the rod, but this is beyond the scope of this paper.

5.4. **Conclusions.** We presented the numerical computation of a twisted elastic ring in a configuration with self-contact along a line, where no skip-fly segment arises between the contact line and the terminal loop. The equilibrium path of the rod shape was computed with the Path-Following Simplex Algorithm in the space of the parameters defining the rod shape. An universal starting point, independent of the rod length was given to the path-following. Using an approximate method for computing the twist and writhe of the spatial curve, we proved that the assumed configuration arises at very high twist rates beyond the interests of former research work.

Acknowledgement. The authors gratefully acknowledge the useful discussions with G. Domokos and the support of the Hungarian Grants FKFP-0177/2001 and OTKA-T37880.

References

1. Zajac, E. E.: Stability of two planar loop elasticas. *J. Appl. Mech.*, **29**, (1962), 136-142.
2. Dichmann, D. J., Li, Y. and Maddocks, J. H.: Hamiltonian formulations and symmetries in rod mechanics. In: J. P. Mesirov, K. Schulten, D. W. Sumners, eds., *Mathematical Approaches to Biomolecular Structure and Dynamics*, Springer, New York, 1996, 71-113.
3. Domokos, G.: A group theoretic approach to the geometry of elastic rings. *J. Nonlinear Science*, **5**, (1995), 453-478.
4. Coleman, B. D., Swigon, D. and Tobias, I.: Elastic stability of DNA configurations. II. Supercoiled plasmids with self-contact. *Physical Review E*, **61**, (2000), 759-770.
5. Swigon, D., Coleman, B. D. and Tobias, I.: The elastic rod model for DNA and its application to the tertiary structure of DNA minicircles and mononucleosonmes. *Biophysical Journal*, **74**, (1998), 2515-2530.
6. Thompson, J. M. T., van der Heijden G. H. M. and Neukirch, S.: Super-Coiling of DNA-Plasmids: the Generalised Ply. *Proc. R. Soc. Lond., Series A*, **458**, (2002), 959-985.
7. Gáspár, Z. and Németh, R.: A special shape of a twisted ring. *Proc. of 2nd European Conference on Computational Mechanics*, CD p. 11, 2001.
8. Przybyl, S. and Pieranski, P.: In search of ideal knots III Application of Maple V.4 to the problem of two ropes tightly twisted together. *Pro Dialog*, **6**, (1998), 18. (in Polish)
9. Domokos, G. and Gáspár, Z.: A global, direct algorithm for path-following and active static control of elastic bar structures. *Int. J. of Structures and Machines*, **23**, (1995), 549-571.
10. Domokos, G. and Szeberényi, I.: A hybrid parallel approach to nonlinear boundary value problem. *Computer Assisted Mechanics and Engineering Sciences*, **11**, (2004), 15-34.
11. Coleman, B. D. and Swigon, D.: Theory of supercoiled elastic rings with self-contact and its application to DNA plasmids. *J. Elasticity*, **60**: (2000), 173-221.
12. White, J. H.: Self-linking and the Gauss integral in higher dimensions. *Am. J. Math.*, **91**, (1969), 693-728.
13. Fuller, F. B.: The writhing number of a space curve. *Proc. Natl. Acad. Sci. USA.*, **68**, (1971), 815-819.

Journal of Computational and Applied Mechanics, Vol. 6., No. 1., (2005), pp. 53–65

ANALYSIS, OPTIMIZATION AND IDENTIFICATION OF COMPOSITE STRUCTURES USING BOUNDARY ELEMENT METHOD

Radosław Górski and Piotr Fedelinski
Silesian University of Technology
Department for Strength of Materials and Computational Mechanics
Konarskiego, 18a, 44-100 Gliwice, Poland
Radoslaw.Gorski@polsl.pl, Piotr.Fedelinski@polsl.pl

[Received: December 9, 2003]

Abstract. In the paper the formulation and application of the subregion boundary element method (BEM) to static and dynamic analysis, optimization and identification of two-dimensional bodies are presented. The subregion method allows modeling of composite structures by assuming different material properties of particular regions. The governing BEM equations for all regions are combined using the condition of compatibility of displacements and equilibrium of tractions between the common interfaces. The transient problem is solved using the dual reciprocity method (DRM). The problem of optimization or identification is solved by the evolutionary algorithm (EA). Numerical examples showing the application of the combined BEM and EA are presented. The position of the interface in a two-zone composite plate is optimized in order to minimize support or interface tractions. The position and length of a crack between two materials are identified.

Mathematical Subject Classification: 74S15
Keywords: boundary element method, subregion method, evolutionary algorithms, composite materials, dynamics, optimization, identification

1. **Introduction**

Structures which consist of two or more different materials, are called composite materials. In recent years a great interest in composite materials having new properties has been observed. They usually have better mechanical properties than the traditional homogenous materials, for example, high stiffness, strength and simultaneously small weight. Nowadays, composite materials are very often used in modern structures, especially in the aircraft industry, where light and highly resistant structures are required. New methods of analysis of such materials are still developed.

In the present paper composite structures are analyzed using the subregion method [1,2] and the dual reciprocity boundary element method (DRBEM) [3]. The DRBEM is the fastest approach in the dynamic analysis by the BEM [4] and it has been applied in different fields of mechanics mainly to homogeneous materials. The subregion BEM allows modeling of composite structures by dividing a body into subregions of different material properties. Each subregion is considered separately and the equations for the whole structure are combined using the condition of compatibility of displacements and equilibrium of tractions between the common interfaces. The method can be used in the analysis of cracked homogeneous and composite structures. High concentrations of stresses are usually present at the interface between different materials in composites. The subregion BEM allows the determination of displacements and stresses at the interface very accurately because they are directly incorporated in the formulation of the method. The application of the DRBEM and the subregion method in the static and dynamic analysis of composite structures is presented in [5,6,7]. A comparison of the BEM results with analytical solutions and computed by the finite element method (FEM) is presented in [5,6] showing a very good agreement.

The identification and optimization of composite structures are important problems of mechanical engineering. Good properties of composites can be additionally improved by a proper choice of materials and their structure using the optimization process. The application of the subregion BEM to optimization and identification of statically loaded structures was presented in several works [8,9,10]. The problems were solved using gradient methods, which require sensitivities of objective functions.

The shape optimization of the interface between different materials for plane and axisymmetrical problems is presented in [8]. The problem was solved using sensitivity analysis and the shape variation was represented using the material derivative concept. The functionals depending on displacements, tractions and the von Mises stresses at the interface were used as criteria of optimization. The optimal shape of the interface of endosseous implants in dentistry was searched for.

The identification of shape and material properties in two-dimensional finite bodies is presented in [9]. The method was based on the minimization of the least square errors between measured and computed displacements. The regularization function was added to the error function in order to overcome ill-posedness of the inverse problem. The problem was solved by recursive quadratic programming with the line search method. The method was applied in identification of different shapes and material properties of inclusions and crack-like voids.

The identification and optimization of the position of a deformable inclusion is presented in [10]. The aim of optimization was the maximization of stiffness of the matrix-inclusion system characterized by its strain energy. The gradient of the objective function was computed by implicit differentiation.

Recently optimization and identification problems are solved using the evolutionary methods, which imitate evolutionary processes in nature [11,12]. Contrary to the gradient methods of optimization, the evolutionary methods can be simply implemented because they need only the values of objective functions. Examples of optimization of statically and dynamically loaded homogeneous bodies using the evolutionary methods are presented for instance in [13]. Examples of maximization of stiffness of composite structures by the combined DRBEM and the EA are presented in [6,14]. The results of minimization of support and interface tractions are presented in [7,15]. The results of identification of material defects in the form of inclusions and cracks are presented in [6,16] and [7], respectively.

In the present work the formulation and application of the subregion DRBEM and the EA for problems of analysis, optimization and identification are presented. Several numerical examples are shown, in which statically or dynamically loaded rectangular plates consisting of different materials are considered. The aim of optimization is the minimization of tractions at the fixed boundary or at the interface. The aim of identification is to find the position and length of a crack between two different materials. The constraints on design variables defining geometry of composites are imposed. The variation of tractions or displacements on design variables is investigated by the systematic search method.

2. **Subregion dual reciprocity boundary element method**

In many cases bodies consist of several homogeneous and isotropic domains. Such structures subjected to dynamic loads can be analyzed using the subregion DRBEM. Consider a linear-elastic body subjected to dynamic load and consisting of two isotropic and homogeneous materials as shown in Figure 1. The materials occupy domains Ω^1 and Ω^2, the external boundaries are Γ^1 and Γ^2 and the internal boundary (interface) is Γ^{12}. On the external boundary $\Gamma = \Gamma^1 \cup \Gamma^2$ the displacement field $\mathbf{U}(\mathbf{x}, t)$ and the traction field $\mathbf{P}(\mathbf{x}, t)$ are prescribed.

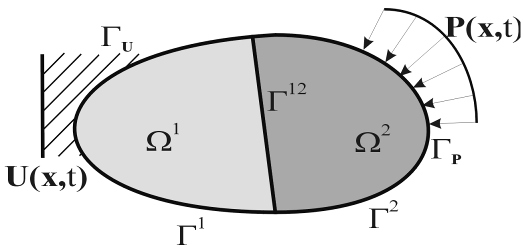

Figure 1. A body made of two different materials

In DRBEM the numerical solution is obtained after dividing a body into boundary elements. For some problems more accurate results can be obtained by using additional internal points. The DRBEM allows the formulation of the system of equations of motion in a matrix form, similar to the FEM. For a simple connected region the equation system to be solved is:

$$\mathbf{M}\ddot{\mathbf{U}} + \mathbf{H}\mathbf{U} = \mathbf{G}\mathbf{P}, \tag{1}$$

where $\mathbf{H}$ and $\mathbf{G}$ are the BEM coefficient matrices, $\mathbf{M}$ represents the mass matrix, $\mathbf{U}$, $\ddot{\mathbf{U}}$ and $\mathbf{P}$ are displacement, acceleration and traction vectors of all boundary nodes, respectively. The elements of matrices $\mathbf{H}$, $\mathbf{G}$ and $\mathbf{M}$ depend on the geometry of a structure and material properties. Contrary to the FEM, the matrices are non-symmetric and fully populated.

The subregion DRBEM requires discretization of the boundary displacements, tractions and coordinates of all regions, including the interfaces which separate them. For the structure in Figure 1, equation (1) is applied to each subregion in turn as if they were independent of each other. The final set of equations for the whole structure is assembled using the condition of compatibility of displacements and equilibrium of tractions between the common interface Γ^{12}:

$$\mathbf{U}^{12} = \mathbf{U}^{21}, \quad \mathbf{P}^{12} = -\mathbf{P}^{21}. \tag{2}$$

Using the above conditions, the whole system of equations for the composite structure in Figure 1 can be rearranged as:

$$\begin{bmatrix} \mathbf{M}^1 & \mathbf{M}^{12} & 0 \\ 0 & \mathbf{M}^{21} & \mathbf{M}^2 \end{bmatrix} \begin{Bmatrix} \ddot{\mathbf{U}}^1 \\ \ddot{\mathbf{U}}^{12} \\ \ddot{\mathbf{U}}^2 \end{Bmatrix} + \begin{bmatrix} \mathbf{H}^1 & \mathbf{H}^{12} & \mathbf{0} & -\mathbf{G}^{12} \\ \mathbf{0} & \mathbf{H}^{21} & \mathbf{H}^2 & \mathbf{G}^{21} \end{bmatrix} \begin{Bmatrix} \mathbf{U}^1 \\ \mathbf{U}^{12} \\ \mathbf{U}^2 \\ \mathbf{P}^{12} \end{Bmatrix} = \\ = \begin{bmatrix} \mathbf{G}^1 & \mathbf{0} \\ \mathbf{0} & \mathbf{G}^2 \end{bmatrix} \begin{Bmatrix} \mathbf{P}^1 \\ \mathbf{P}^2 \end{Bmatrix} \tag{3}$$

where the superscripts 1, 2 and 12 (21) denote the matrices that correspond to the appropriate boundaries. The above system of equations is rearranged according to the boundary conditions and solved step-by-step giving the unknown displacements and tractions on the external boundary and the interface at each time step. The total number of unknowns is equal to the number of nodal degrees of freedom over the external boundaries plus twice the number of nodal degrees of freedom over the internal boundary. On the basis of the procedure described, a computer program which solves the multi-domain problems for the external time dependent tractions has been implemented.

3. Evolutionary algorithm

Evolutionary methods imitate evolutionary processes in nature. These methods are based on evolution of species and survival of the best individuals. The class of algorithms which is based on evolution principles is called genetic algorithms (GAs), evolutionary algorithms (EAs) or evolutionary programs (EPs) [11,12]. In such algorithms a population of individuals (chromosomes) is modified using genetic operators like crossovers and mutations. All chromosomes in a population are estimated using a fitness function which is the value of an objective function. The next populations are created using a selection. The individuals which are well adapted (better value of a fitness function) have a greater chance to form the next population.

In the paper a modified simple genetic algorithm (SGA) is used [11]. The classical SGA uses binary coding, crossover and mutation. A modified SGA, which is also called the EA or EP, uses the floating point coding for representation of the population of chromosomes. The classical binary genetic operators (simple crossover and simple mutation) are modified in accordance with the floating point coding. In the evolutionary algorithms usually new genetic operators are also formulated (evolutionary operators).

The choice of parameters of the EA (probability of evolutionary operators, number of chromosomes) is arbitrary and finding their optimal values is not easy because they usually depend on a problem, for instance the number of design variables and the form of an objective function.

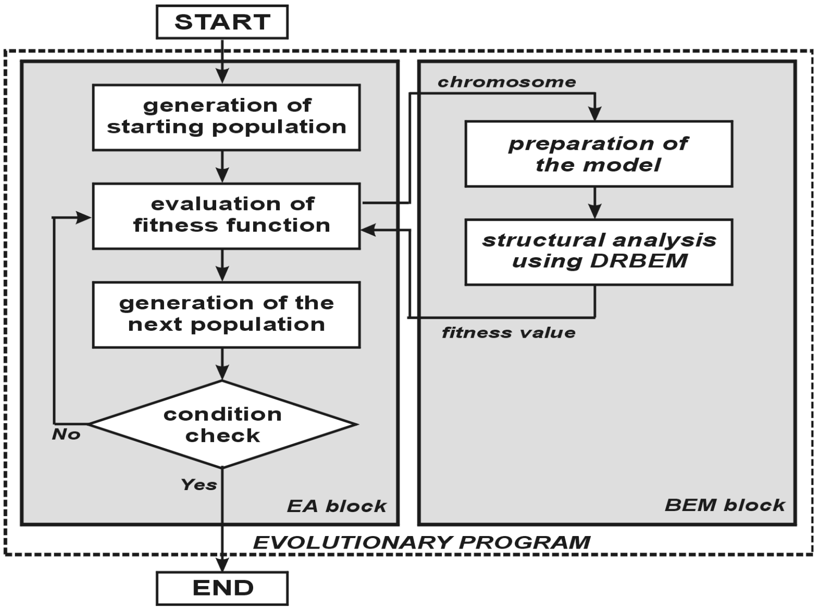

Figure 2. Evolutionary program

A scheme of the EP used in the paper for the optimization and identification is presented in Figure 2. It consists of two main blocks: 1) the block of the EA, in which the operations on the population of chromosomes are performed and 2) the block of the BEM, in which the value of a fitness function is evaluated using the subregion DRBEM.

The initial population of chromosomes is randomly generated from the feasible domain in the first block. Each chromosome consists of genes (design variables) and represents one potential solution of the problem. Appropriate constraints are imposed on genes. The design variables of each chromosome define the shape of one composite structure. The structures are analyzed in the second block by the subregion DRBEM and the values of displacements and tractions on the external boundary and the interface are obtained. The value of a fitness function (an objective function) for each chromosome in the population is evaluated using boundary displacements or tractions (stresses). Then the next population is created using the genetic operators and the selection. The mutation changes the value of genes of the chromosome and the crossover exchanges genes between different chromosomes. This procedure is repeated until the optimal solution is reached. The best chromosome of all generations represents the solution of the problem and its genes define the geometry of the optimal structure. The process of optimization is usually stopped after a fixed number of generations.

4. **Numerical examples**

In order to demonstrate the applications and accuracy of the proposed method in the analysis, optimization and identification, three numerical examples are presented. The linear-elastic and non-homogeneous rectangular plates subjected to static or dynamic (Heaviside function) loads as shown in Figure 3 are considered.

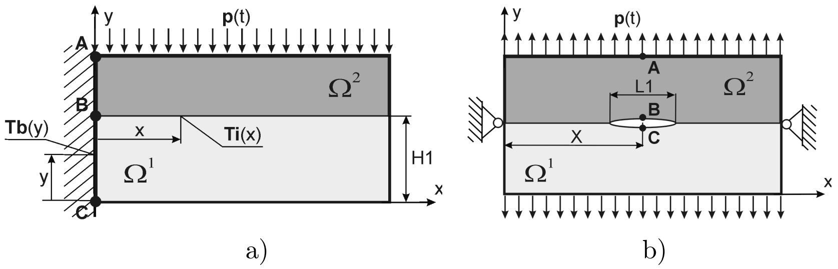

Figure 3. Composite plates: a) two-zone cantilever plate, b) two-zone plate with a crack

Position $H1$ of the straight interface in the plate in Figure 3a is optimized. The objective function – the maximum resultant traction Tb at the fixed boundary or Ti at the interface (for statics and dynamics) – is minimized with respect to design variable $H1$.

Position X and length $L1$ of the crack in the plate in Figure 3b is identified. The objective function is minimized with respect to design variables X and $L1$. It depends on the difference between the measured and the computed values of boundary displacements (for statics and dynamics). The measurement is simulated numerically. Sensor points, in which displacements are measured along the y axis, are placed at all nodes on the upper and lower boundary of the plate (where the non-zero tractions are prescribed).

During the optimization and identification, the number of boundary elements is constant and their size changes, which simplifies the boundary discretization. In order to avoid significant differences in the size of the elements, which can decrease the accuracy of the solution, appropriate constraints are imposed. In order to investigate the influence of the initial populations on the final results, five tests are performed for each problem.

The length and the height of each plate is 10 cm and 5 cm respectively. The interface in the plate in Figure 3a is defined by design variable $H1$ and the interface is at half of the height in the plate in Figure 3b. The value of variable $H1$ belongs to the interval from 1 to 4 cm. The coordinate of the center of the crack is X and its length is $L1$. Variables X and $L1$ belong to the intervals from 2.5 to 7.5 cm and 1 to 4 cm, respectively. The value of the load is 1 MPa. The time of BEM analysis (Houbolt scheme) is 600 μs and the time step is $\Delta t = 2\mu s$. The values of the material properties for the zone Ω^l (aluminum) and Ω^2 (steel) are: modulus of elasticity $E_1 = 70\,GPa$ and $E_2 = 210\,GPa$, Poisson's ratio $\nu_1 = 0.34$ and $\nu_2 = 0.3$, density $\rho_1 = 2700\,kg/m^3$ and $\rho_2 = 7860\,kg/m^3$, respectively. Plane strain state is assumed. The total number of boundary elements is 50 and 52 (with 10 and 8 elements on the interface) for the plates in Figure 3a and Figure 3b, respectively.

In the present evolutionary algorithm the following evolutionary operators with the corresponding values of probability are used: Gauss mutation (62.5%), uniform mutation (25%), arithmetic and simple crossover (6.25%). In all examples the number of chromosomes in the population is 10.

Example 1: minimization of the support tractions. The composite plate shown in Figure 3a is considered. The results of the static and dynamic analysis and the optimization are presented. The criterion of optimization is minimization of tractions at the fixed boundary with respect to position of the interface $H1$.

The distribution of static tractions *Tb(y)* along the fixed boundary for different positions of the interface $H1$ is presented in Figure 4.

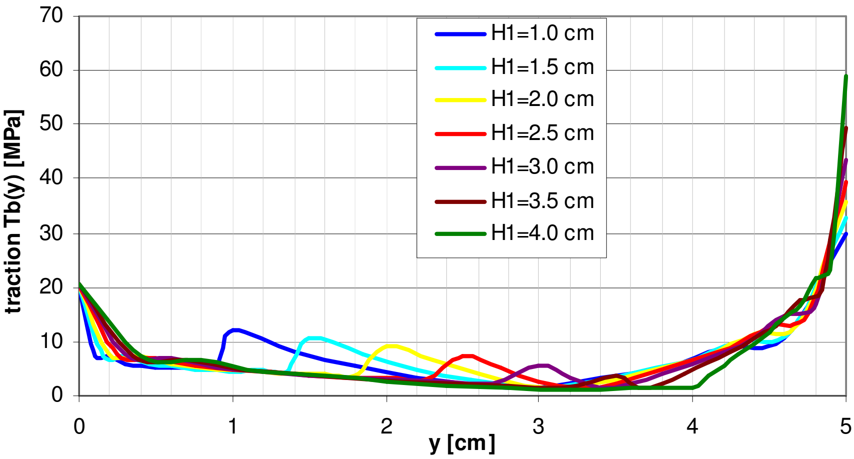

Figure 4. Distribution of static tractions *Tb(y)* along the fixed boundary for different positions of the interface $H1$

The value of traction increases at point A, decreases at point B and does not change at point C (see Figure 3a) when the variable $H1$ increases. Due to different material properties of the two subregions connected at the interface, jumps in the tractions at point B can be observed. The tractions are greater on the boundary of the stiffer material (steel) and they increase when the area of this material increases. It can be noticed that the traction is minimum at point A for $H1$=1 cm and the value of the objective function is $Tb = 29.88\,MPa$.

The time history of tractions $Tb(y,t)$ at point A for three positions of the interface is presented in Figure 5. The dynamic tractions are also maximum at point A and the peak values are about two times greater than the static ones for the corresponding positions of the interface. The optimal solution is for $H1 = 1$ cm and the value of the objective function is $Tb = 54.72\,MPa$ for time $t = 462\mu s$.

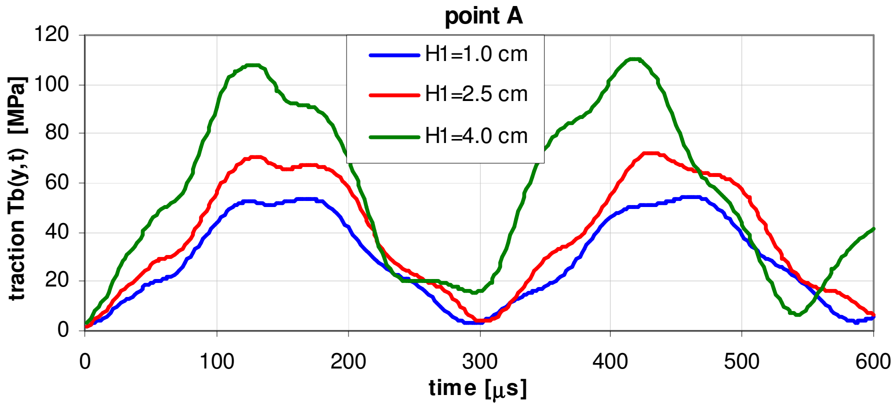

Figure 5. Dynamic tractions $Tb(y,t)$ at point A for three positions of the interface $H1$

The results of optimization after 10 generations obtained by the EA are compared with the exact solution obtained by the systematic search method and are presented in Table 1. The convergence of the solutions is very fast because only one design variable is used and the range of its variability is small. The results in Table 1 are the exact solutions (see Figures 4 and 5). It can be observed that one of the constraints imposed on the variable $H1$ is active.

Test No.	Statics		Dynamics	
	$H1$ [cm]	Tb [MPa]	$H1$ [cm]	Tb [MPa]
1	1.00	29.88	1.00	54.72
2	1.00	29.88	1.00	54.72
3	1.00	29.88	1.00	54.72
4	1.00	29.88	1.00	54.72
5	1.00	29.88	1.00	54.72
Exact	1.00	29.88	1.00	54.72

Table 1. Results of optimization – minimization of the support tractions

Example 2: minimization of the interface tractions. The composite cantilever plate shown in Figure 3a is considered. The results of the static analysis and the optimization are presented. The criterion of optimization is minimization of tractions at the interface with respect to its position $H1$.

The distribution of static tractions $Ti(x)$ along the interface for its different positions $H1$ is presented in Figure 6. The greatest values of tractions are obtained at the nodes close to the fixed boundary. The optimum obtained by the systematic search method is at the point for which the coordinate $x = 1$ cm and the position of the interface is $H1 = 3.5\,cm$ (see Figure 6).

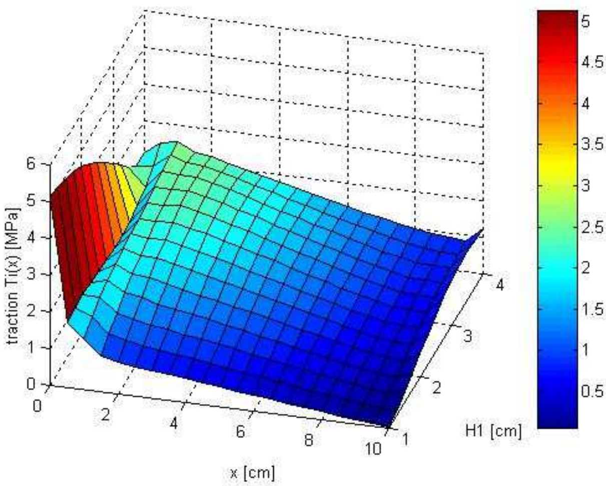

Figure 6. Static tractions $Ti(x)$ along the interface for its different positions $H1$

The results of optimization after 10 and 100 generations obtained by the EA for the static and dynamic problems are presented in Table 2. As in the previous example, the convergence of the solutions is very fast. The solutions obtained after 100 generations are more precise than the results after 10 generations but the difference between them is small. In this example the constraints imposed on design variable $H1$ are not active.

Test No.	Statics				Dynamics			
	10 generations		100 generations		10 generations		100 generations	
	$H1$ [cm]	Ti [MPa]	$H1$ [cm]	Ti [MPa]	$H1$ [cm]	Ti [MPa]	$H1$ [cm]	Ti [MPa]
1	3.5040	2.4535	3.4895	2.4487	3.5580	4.6710	3.5576	4.6708
2	3.4936	2.4501	3.4878	2.4482	3.5575	4.6708	3.5575	4.6708
3	3.4956	2.4507	3.4882	2.4483	3.5515	4.6730	3.5571	4.6708
4	3.4966	2.4511	3.4918	2.4495	3.5690	4.6760	3.5573	4.6708
5	3.4977	2.4515	3.4877	2.4481	3.5535	4.6723	3.5563	4.6712

Table 2: Results of optimization – minimization of the interface tractions

Example 3: identification of the crack. The composite plate with the crack shown in Figure 3b is considered. The results of the static and dynamic analysis and the identification are presented. Position X and length $L1$ of the crack between two materials are identified by minimization of difference between the measured and the computed boundary displacements.

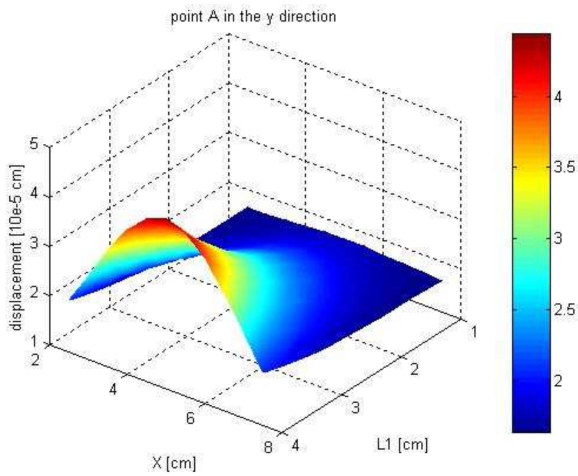

Figure 7. The variation of the static displacement at point A with respect to position X and length $L1$ of the crack

The influence of the center of the crack X and its length $L1$ on the static displacement at point A is presented in Figure 7. For a fixed value of the variable X or $L1$, the variation of displacement is great when the crack is long or it is near the center of the plate, respectively. If length $L1$ is small and the crack is near the left or the right boundary of the plate, the values of displacement at point A are small. The form of the variation function for a middle node located on the lower boundary is very similar to that in Figure 7. In this case greater values of displacements are obtained due to the smaller stiffness of aluminum.

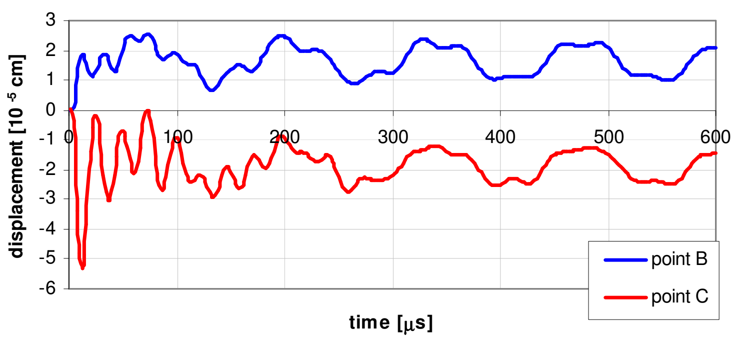

Figure 8. Dynamic displacements at points B and C

The static and dynamic displacements are computed for nodes B and C (see Figure 3b). The analysis is performed for $X = 5$ cm and $L1 = 2$ cm. The values of the static displacements along the y axis obtained for these points are $u_B = 1.64$ and $u_C = -1.87$ [10^{-5} cm], respectively. It can be noticed that due to the applied boundary conditions as shown in Figure 3b, the crack surfaces are not in contact (values of displacements have opposite signs). The time history of the dynamic displacements at points B and C along the y axis is presented in Figure 8. In this case the crack is also open during the whole time of the analysis. Fast oscillations of displacements, especially at point C (aluminum), can be observed during the initial period of time.

The results of identification after 10 and 100 generations obtained by the EA for the static and dynamic problems are presented in Table 3. The convergence of the solutions is fast. As in the previous example, the solutions obtained after 10 and 100 generations are good. The results after 1000 generations (not included in the paper) are very precise and for most of them the real solution (exact) is reached.

TestNo.	Statics				Dynamics			
	10 generations		100 generations		10 generations		100 generations	
	X[cm]	$L1$ [cm]	X[cm]	$L1$ [cm]	X[cm]	$L1$[cm]	X[cm]	$L1$ [cm]
1	4.9606	2.0156	5.0014	2.0014	4.9885	1.9464	5.0007	1.9989
2	5.0070	1.9747	4.9991	1.9971	4.9858	1.9893	4.9986	2.0004
3	5.0098	1.9842	4.9983	2.0000	5.0115	2.0111	5.0009	1.9989
4	4.9649	1.9830	4.9953	2.0000	4.9854	1.9531	5.0064	1.9993
5	4.9664	1.9521	4.9994	1.9970	4.9999	2.0071	4.9999	1.9996
Real sol.	5.0000	2.0000	5.0000	2.0000	5.0000	2.0000	5.0000	2.0000

Table 3. Results of identification of the crack

5. **Conclusions**

In the paper the subregion dual reciprocity boundary element method and the evolutionary algorithm are used in the static and dynamic analysis, optimization and identification of composite structures. The transient problem is solved using the dual reciprocity method. The problem of optimization or identification is solved by the evolutionary algorithm.

The composite cantilever plate and the plate with a crack consisting of different materials (steel and aluminum) are analyzed. The static or dynamic tractions and displacements for selected points of structures are presented. For the cantilever composite plate the tractions at the fixed boundary are about one order of magnitude greater than the tractions at the interface and the value of the prescribed load. The maximal support tractions are present at the corner point which belongs to the stiffer material (steel). The maximal interface tractions are present at nodes close to the fixed boundary. The crack in the second composite plate is located on the interface between two materials. The influence of the position and length of the crack on displacements at boundary nodes located at half of the length of the plate is investigated.

The variation of static displacements is great when the crack is long and it is at the center of the plate.

The numerical results of optimization and identification (for one or two design variables) obtained by the evolutionary algorithm are shown. The position of the horizontal interface in the cantilever composite plate defined by one design variable is optimized using two criteria: 1) the minimization of tractions at the fixed boundary and 2) the minimization of tractions at the interface. The support tractions are minimum when the area of steel is maximum. The interface tractions are minimum when the area of aluminum is greater than the area of steel (but not maximum). The interface crack defined by two design variables is identified by the evolutionary algorithm very accurately.

The numerical examples considered are simple therefore the evolutionary algorithm results can be compared with the known solutions obtained by investigation of the objective functions by the systematic search method. The influence of the initial populations of chromosomes (which are random) on the solutions obtained by the evolutionary algorithm is investigated by solving five tests for each problem. For all numerical tests of the particular problem the accuracy of the results is very good. Generally, in the presented examples the initial populations do not influence the final results obtained by the algorithm but usually a greater number of generations is required to obtain more accurate results.

The examples of optimization and identification show that the boundary element method is very useful in problems which require many changes of boundaries. The modification of boundary discretization and the preparation of all needed data are very simple. The results obtained by the evolutionary algorithm for a small number of design variables (one or two) are very accurate and the convergence of the results to the exact solutions is fast. The advantage of the evolutionary methods is that they can be implemented simply because they require only the values of objective functions.

Acknowledgement. The scientific research is financed by the State Committee for Scientific Research in years 2003-2005 by the grant No. 5-T07A-048-25.

References

1. Brebbia, C.A. and Dominguez, J.: *Boundary Elements. An Introductory Course.* 2^{nd} ed., CMP and McGraw-Hill, Southampton and New York, 1992.
2. Kane, J.H.: *Boundary Element Analysis in Engineering Continuum Mechanics.* Prentice Hall, Englewood Cliffs, New Jersey, 1994.
3. Dominguez, J.: *Boundary Elements in Dynamics.* CMP, Southampton, 1993.
4. Fedelinski, P.: Boundary element method in dynamic analysis of cracked structures. *Scientific Papers of Silesian University of Technology, Mechanics*, No. 137, Gliwice, (2000). (in Polish)
5. Górski, R. and Fedelinski, P.: Subregion boundary element method for two-dimensional transient elastodynamics. *Scientific Papers of Rzeszów University of Technology, Mechanics*, **60**(197), (2002), 227-234.

6. Fedelinski, P., Górski, R. and Czyz, T.: Subregion boundary element method in optimization and identification of structures. 15^{th} *International Conference on Computer Methods in Mechanics CMM-2003*, Short Papers (eds Burczyński T., Fedelinski P., Majchrzak E.), Gliwice/Wisła, (2003), 125-126 (CD-ROM Proceedings: 8 pages).
7. Górski, R. and Fedelinski, P.: Analysis, optimization and identification of composite structures using boundary element method. 9^{th} *International Conference on Numerical Methods in Continuum Mechanics NMCM-2003*, Proceedings of the Extended Abstracts (eds Kompis V., Sladek J., Zmindak M.), Zilina, (2003), 44-45 (CD-ROM Proceedings: pp. 14).
8. Choi, J. H., Lee, B. Y. and Han, J. S.: Boundary integral method for shape optimization of interface problems and its application to implant design in dentistry. *Computer Methods in Applied Mechanics and Engineering*, **190**, (2001), 6909-6926.
9. Lee, H. S., Park, C. J. and Park, H. W.: Identification of geometric shapes and material properties of inclusions in two-dimensional finite bodies by boundary parameterization. *Computer Methods in Applied Mechanics and Engineering*, **181**, (2000), 1-20.
10. Mallardo, V. and Alessandri, C.: Inverse problems in the presence of inclusions and unilateral constraints: a boundary element approach. *Computational Mechanics*, **26**, (2000), 571-581.
11. Michalewicz, Z.: *Genetic algorithms + data structures = evolution programs.* Springer-Verlag, Berlin, 1996.
12. Goldberg, D. E.: *Genetic Algorithms in Search, Optimization and Machine Learning.* Addison Publishing Company, Inc, Reading, 1998.
13. Burczyński, T. (editor): Computational sensitivity analysis and evolutionary optimization of systems with geometrical singularities. *Scientific Papers of the Department of Strength of Materials and Computational Mechanics*, No. 1, Gliwice, (2002).
14. Górski, R. and Fedelinski, P.: Optimization of composite structures using boundary element method. *Scientific Papers of the Department of Applied Mechanics, Gliwice*, **20**, (2003), 135-140.
15. Fedelinski, P., Górski, R. and Kuś, W.: Evolutionary algorithms in minimization of support and interface tractions. *Methods of Artificial Intelligence AI-METH 2003*, (eds Burczyński T., Cholewa W., Moczulski W.), Gliwice, (2003), 129-132.
16. Fedelinski, P., Górski, R. and Kuś, W.: Evolutionary algorithms in identification of inclusions. *Methods of Artificial Intelligence*, Gliwice, (2002), 59-60 (CD-ROM Proceedings: pp. 4).

Journal of Computational and Applied Mechanics, Vol. 6., No. 1., (2005), pp. 67–82

ANALYSIS OF NONLINEAR ULTRAACOUSTIC WAVE PROPERTIES IN GERMANIUM MONOCRYSTAL

Kristina Kurennaya and Valery Storozhev
Department of Mathematics
Donetsk National University
Donetsk, 83055, Ukraine
kurinna@math.uni-potsdam.de, storozhev@matfak.dongu.donetsk.ua

[Received: January 14, 2004]

Abstract. The present paper investigates the properties of the second harmonics of monochromatic symmetrical normal waves. The analytical representations for nonharmonic distortion of normal waves with a free propagation direction in the plane of a cubic anisotropic monocrystal germanium layer have been obtained. The intensity of the second harmonics and the wave motion forms have been analyzed for nonelastic equivalent propagation directions.

Mathematical Subject Classification: 74J30
Keywords: elastic wave, second harmonics, dynamic deformations

1. **Introduction**

In the present paper nonlinear effects, which appear when stationary stress waves spread in elastic mediums, have been investigated. One of the widely used conceptions of such a study is the determination of the so-called higher orders harmonics, which describe nonlinear, i.e., nonharmonic effects. This conception is effectively used to investigate nonlinear elastic waves with low intensity, and on its base a great number of fundamental scientific and applied results are obtained. The most important features of this conception can be found in papers [1-3]. The procedure we apply is based on the representation of the elastic wave displacements in a series in terms of the acoustic Mach number, which can be regarded as a small parameter.

We obtain appropriate equations for the different members of the series from the nonlinear equations of dynamics written in terms of displacements. The solutions to these equations are referred to as second, third and fourth order harmonics, respectively. By applying this approach we want to determine the second harmonics of monochromatic elastic waves, which belong to one of the wave motions mode for the waveguide considered, or the compound second harmonics of linear waves. The latter belong to two different waveguide modes. In the second case, the question about the normal waves' three-phonon interaction deserves special attention.

Works [1-9] are devoted to the solution methods and provide a number of results for the propagation of the second harmonics of elastic waves in anisotropic bodies. In these works a geometrically nonlinear model is selected and the effect of the propagation medium on the equations of motion is also clarified. The issues of how to obtain the solutions, how to describe the second harmonics and the basic physical-mechanical effects for the nonlinear wave phenomena have all been analyzed both theoretically and experimentally. In the above works the second harmonics of longitudinal and shift bulk waves in isotropic mediums, the second harmonics of compound monochromatic waves in crystalline mediums in a number of crystal systems have been obtained. The questions about three-phonon interaction of bulk elastic waves in anisotropic and isotropic mediums have also been considered. In paper [10] the second harmonics are found for Relay-type surface waves in an isotropic medium.

There are only a few works devoted to the problem of how to obtain and analyze the second harmonics of normal waves in waveguides of different geometry with cross-section dimension, restricted at least on one coordinate. For example, in paper [11] the analysis of nonharmonic effects for the propagation of flexure elastic waves in a thin isotropic lamina is considered.

2. **The model and basic equations of the wave process**

Indicial notations are employed in a Cartesian coordinate system throughout this paper. In accordance with the general rules of indicial notations summation over repeated indices is implied and subscripts preceded by a colon denote differentiation with respect to the corresponding coordinate. Latin indices range over the integers 1, 2 and 3.

Nonlinear elastic wave propagation has been investigated in an arbitrary direction in the plane of the waveguide. The volume V under consideration is given by

$$V = \{-\infty < x_1, x_2 < \infty, |x_3| \leq h\}, \tag{2.1}$$

where x_1, x_2 and x_3 are non-dimensional coordinates.

The body under consideration is homogenous and anisotropic. The problem is a dynamic one. Components ε_{ij} of the Lagrange deformation tensor in terms of displacements u_i are given by the equation

$$\varepsilon_{ij} = \frac{1}{2}(u_{i,j} + u_{j,i} + u_{l,i}u_{l,j}). \tag{2.2}$$

It is assumed that the elastic potential has the form

$$U = \frac{1}{2}c_{ijkl}\varepsilon_{ij}\varepsilon_{kl} + \frac{1}{6}c_{ijklmn}\varepsilon_{ij}\varepsilon_{kl}\varepsilon_{mn}, \tag{2.3}$$

in which c_{ijkl} and c_{ijklmn} are the tensors of elastic constants. The second Piola–Kirchoff stress tensor σ_{jq} can be divided into two parts:

$$\sigma_{jq} = \partial U/\partial(u_{j,q}) = \sigma_{jq}^{(l)} + \sigma_{jq}^{(n)}, \tag{2.4}$$

where

$$\sigma_{jq}^{(l)} = c_{jqik}u_{i,k}, \quad \sigma_{jq}^{(n)} = \tfrac{1}{2}c_{jqik}u_{l,i}u_{l,k} + c_{pqik}u_{j,p}u_{i,k} + \tfrac{1}{2}c_{jqiklm}u_{i,k}u_{l,m}. \tag{2.5}$$

The density and elastic properties of the O^h class monocrystal cubic system layer under consideration are characterized by the following second and third order nonzero elastic constants:

$$\begin{gathered}
\tilde{\rho} = \rho\rho_*; \quad \tilde{c}_{11} = \tilde{c}_{22} = \tilde{c}_{33} = c_{11}c_*; \\
\tilde{c}_{12} = \tilde{c}_{13} = \tilde{c}_{21} = \tilde{c}_{23} = \tilde{c}_{31} = \tilde{c}_{32} = c_{12}c_*; \\
\tilde{c}_{44} = \tilde{c}_{55} = \tilde{c}_{66} = c_{44}c_*; \quad \tilde{c}_{111} = \tilde{c}_{222} = \tilde{c}_{333} = c_{111}c_*; \\
\tilde{c}_{112} = \tilde{c}_{113} = \tilde{c}_{122} = \tilde{c}_{133} = \tilde{c}_{223} = \tilde{c}_{233} = c_{112}c_*; \\
\tilde{c}_{144} = \tilde{c}_{255} = \tilde{c}_{366} = c_{144}c_*; \quad \tilde{c}_{123} = c_{123}c_*; \quad \tilde{c}_{456} = c_{456}c_*; \\
\tilde{c}_{155} = \tilde{c}_{166} = \tilde{c}_{244} = \tilde{c}_{266} = \tilde{c}_{344} = \tilde{c}_{355} = c_{155}c_*,
\end{gathered} \tag{2.6}$$

where the values of the normalizing parameters are $c_* = 10^{10}$ Pa, $\rho_* = 10^3$ kg/m^3.

The elastic potential in quadratic and cubic terms of $u_{i,j}$ for the monocrystal layer has the form

$$\begin{gathered}
U = \tfrac{1}{2}c_{11}\textstyle\sum_{k=1}^{3} u_{k,k}^2 + \tfrac{1}{2}c_{44}\sum_{k,l=1,\, k\neq l}^{3} u_{k,l}^2 + \\
+c_{44}\textstyle\sum_{k,l=1,\, k<l}^{3} u_{k,l}u_{l,k} + c_{12}\sum_{k,l=1,\, k<l}^{3} u_{k,k}u_{l,l} + \\
+\tfrac{1}{2}\Delta_3\textstyle\sum_{k,l=1,\, k\neq l}^{3} u_{k,k}u_{l,k}^2 + \tfrac{1}{2}\Delta_2\sum_{k,l=1,\, k\neq l}^{3} u_{k,k}u_{k,l}^2 + \\
+\Delta_6\textstyle\sum_{k,l,m=1,\, k\neq l,m,\, l<m}^{3} u_{k,l}u_{k,m}(u_{l,m}+u_{m,l}) + \\
+\tfrac{1}{6}\Delta_1\textstyle\sum_{k=1}^{3} u_{k,k}^3 + \tfrac{1}{2}\Delta_5\sum_{k,l=1,\, k\neq l}^{3} u_{k,k}u_{l,l}^2 + \\
+\tfrac{1}{2}\Delta_7\textstyle\sum_{k,l,m=1,\, k\neq l,m,\, l\neq m}^{3} u_{k,k}u_{l,m}^2 + \\
+c_{144}\textstyle\sum_{k,l,m=1,\, k\neq l,m,\, l<m}^{3} u_{k,k}u_{l,m}u_{m,l} + \\
+\Delta_4\textstyle\sum_{k,l=1,\, k<l}^{3} u_{k,k}u_{k,l}u_{l,k} + \\
+\textstyle\sum_{k,l,m=1,\, k\neq l,m,\, l\neq m}^{3} u_{k,l}u_{k,m}u_{m,l} + \\
+c_{456}\textstyle\sum_{l,m=2,\, l\neq m}^{3} u_{1,l}u_{l,m}u_{m,1},
\end{gathered} \tag{2.7}$$

where

$$\begin{gathered}
\Delta_1 = 3\,c_{11} + c_{111}; \quad \Delta_2 = c_{12} + 2\,c_{44} + c_{155}; \quad \Delta_3 = c_{11} + c_{155}; \\
\Delta_4 = c_{44} + c_{155}; \quad \Delta_5 = c_{12} + c_{112}; \quad \Delta_6 = c_{44} + c_{456}; \quad \Delta_7 = c_{12} + c_{144}.
\end{gathered} \tag{2.8}$$

The equations of motion in terms of displacements are obtained from the equation of motion

$$\sigma_{ij,j} = \rho_0\ddot{u}_i \tag{2.9}$$

and have the form

$$\rho_0 \ddot{u}_j - \Delta_8(u_{l,lj} + u_{k,kj}) - c_{44}(u_{j,ll} + u_{j,kk}) - c_{11}u_{j,jj} =$$
$$= \Delta_1 u_{j,j}u_{j,jj} + \Delta_2(2u_{j,l}u_{j,lj} + 2u_{j,k}u_{j,kj} + u_{j,j}u_{j,ll} + u_{j,j}u_{j,kk}) +$$
$$+\Delta_3(u_{l,j}u_{l,jj} + u_{k,j}u_{k,jj} + u_{l,l}u_{j,ll} + u_{j,l}u_{l,ll} + u_{k,k}u_{j,kk} + u_{j,k}u_{k,kk}) +$$
$$+\Delta_4(2u_{l,j}u_{j,lj} + u_{j,l}u_{l,jj} + 2u_{k,j}u_{j,kj} + u_{j,k}u_{k,jj} + u_{l,j}u_{l,ll} + u_{k,j}u_{k,kk}) +$$
$$+\Delta_5(u_{l,l}u_{j,jj} + u_{k,k}u_{j,jj}) +$$
$$+\Delta_9(u_{k,l}u_{l,kj} + u_{l,k}u_{k,lj} + u_{k,j}u_{l,kl} + u_{l,j}u_{k,lk}) + \tag{2.10}$$
$$+\Delta_{10}(u_{k,k}u_{l,lj} + u_{l,l}u_{k,kj}) +$$
$$+\Delta_6(u_{k,j}u_{k,ll} + 2u_{k,l}u_{j,kl} + u_{j,k}u_{k,ll} + 2u_{l,k}u_{j,lk} + u_{j,l}u_{l,kk} + u_{l,j}u_{l,kk}) +$$
$$+\Delta_7(u_{k,k}u_{j,ll} + u_{l,l}u_{j,kk}) +$$
$$+(\Delta_4 + \Delta_5)(u_{l,l}u_{l,lj} + u_{j,j}u_{l,lj} + u_{j,j}u_{k,kj} + u_{k,k}u_{k,kj}) +$$
$$+(\Delta_6 + \Delta_7)(u_{l,k}u_{l,kj} + u_{k,l}u_{k,lj} + u_{j,k}\ u_{l,kl} + u_{j,l}u_{k,lk}) \quad (j = \overline{1,3}),$$

where

$$l = \begin{cases} 1, & j = 2,3; \\ 2, & j = 1; \end{cases} \qquad k = \begin{cases} 3, & j = 1,2; \\ 2, & j = 3; \end{cases} \tag{2.11}$$

$$\Delta_8 = c_{12} + c_{44}; \quad \Delta_9 = c_{144} + c_{456}; \quad \Delta_{10} = c_{123} + c_{144}. \tag{2.12}$$

Our main objective is to find the analytical representations for second harmonics of normal three-partial waves. More precisely we would like to determine what forms the linear three-partial waves' second harmonics have and to investigate the intensity levels of the second harmonics.

3. Analytical solution of a homogeneous problem for linear waves

After giving the elastic displacements u_j as a sum of the linear harmonic terms $u_j^{(l)}$ and its inharmonic distortion $u_j^{(n)}$ – the latter is proportional to the acoustic Mach number of the first degree – we can determine the expressions for $u_j^{(l)}$ and $u_j^{(n)}$ from the first and the second boundary value problems:

$$\begin{gathered} \rho_0 \ddot{u}_j^{(l)} - c_{jsrk}u_{s,k}^{(l)} = 0, \\ (c_{3srk}u_{r,k}^{(l)})_{x_3=\pm h} = 0; \end{gathered} \tag{3.1}$$

$$\rho_0 \ddot{u}_j^{(n)} - c_{jdik} u_{i,dk}^{(n)} = c_{jdik} u_{l,dk}^{(l)} u_{l,i}^{(l)} + c_{pdik} (u_{j,dp}^{(l)} u_{i,k}^{(l)} +$$

$$+ u_{i,dk}^{(l)} u_{j,p}^{(l)}) + c_{jdiklm} u_{i,dk}^{(l)} u_{l,m}^{(l)},$$

$$(c_{3dik} u_{i,k}^{(n)})_{x_3=\pm h} = -(\tfrac{1}{2} c_{3dik} u_{l,i}^{(l)} u_{l,k}^{(l)} + \tag{3.2}$$

$$+ c_{pdik} u_{3,p}^{(l)} u_{i,k}^{(l)} + \tfrac{1}{2} c_{3diklm} u_{i,k}^{(l)} u_{l,m}^{(l)})_{x_3=\pm h}.$$

Partial displacement functions of the linear normal waves, which propagate in the waveguide plain in an arbitrary direction characterized by the angle φ and the vector $\mathbf{n}$, can be represented in a complex exponential form

$$u_j^{(l)}(x_1, x_2, x_3, t) = f_j(x_3) \exp\{-i(\omega t - k(n_1 x_1 + n_2 x_2))\} \quad (j = \overline{1,3}), \tag{3.3}$$

where

$f_j(x_3)$ is the complex amplitude function;

ω is the circular frequency of the wave;

k is a non-dimensional normalized wave number;

$n_1 = \cos\varphi$ and $n_2 = \sin\varphi$ are the components of the wave vector $\mathbf{n}$.

Equations for the amplitude functions $f_j(x_3)$ are obtained from (3.1):

$$\begin{cases} f_1''(x_3) + A_{11} f_1(x_3) + A_{12} f_2(x_3) + A_{13} f_3'(x_3) = 0, \\ A_{21} f_1(x_3) + f_2''(x_3) + A_{22} f_2(x_3) + A_{23} f_3'(x_3) = 0, \\ A_{31} f_1'(x_3) + A_{32} f_2'(x_3) + f_3''(x_3) + A_{33} f_3(x_3) = 0; \end{cases} \tag{3.4}$$

$$\begin{cases} (i n_1 f_3(x_3) + f_1'(x_3))_{x_3=\pm h} = 0, \\ (i n_2 f_3(x_3) + f_2'(x_3))_{x_3=\pm h} = 0, \\ (c_{12} i (n_1 f_1(x_3) + n_2 f_2(x_3)) + c_{11} f_3'(x_3))_{x_3=\pm h} = 0. \end{cases} \tag{3.5}$$

In the above equations A_{ij} are the elements of the Christoffel matrix for the cubic medium:

$$\begin{gathered} A_{11} = (\Omega^2 - k^2(c_{11} n_1^2 + c_{44} n_2^2))/c_{44}, \\ A_{22} = (\Omega^2 - k^2(c_{44} n_1^2 + c_{11} n_2^2))/c_{44}, \\ A_{33} = (\Omega^2 - c_{44} k^2 (n_1^2 + n_2^2))/c_{44}, \\ A_{12} = A_{21} = -k^2 n_1 n_2 \Delta_8 / c_{44}, \\ A_{13} = A_{31} = -ikn_1 \Delta_8 / c_{44}, \\ A_{23} = A_{32} = -ikn_2 \Delta_8 / c_{44}. \end{gathered} \tag{3.6}$$

Here $\Omega^2 = \rho\omega^2 R_*^2/C_*$ ($C_* = h$ m) is the non-dimensional frequency parameter.

The characteristic equation for the equation system (3.4) takes the form

$$\begin{vmatrix} \lambda^2 + A_{11} & A_{12} & A_{13} \\ A_{12} & \lambda^2 + A_{22} & A_{23} \\ A_{13} & A_{23} & \lambda^2 + A_{33} \end{vmatrix} = 0\,. \tag{3.7}$$

We will assume such a material for the layer that the characteristic equation (3.7) has three different roots λ_1, λ_2, λ_3 with nonzero real parts. Then the solution to problem (3.4)-(3.5) can be represented as

$$f_j(x_3) = \sum_{m=1}^{3} \beta_{jm} \exp(\lambda_m x_3). \tag{3.8}$$

The relations between the coefficients $\beta_{j,m}$ ($j = 2, 3$) and β_{1m} follow from equation (3.7) and are

$$\beta_{jm} = \frac{Q_{jm}}{D_m}\beta_{1m} \quad (j = \overline{1,3}), \tag{3.9}$$

where

$$\begin{aligned} Q_{1m} &= D_m = (\lambda_m^2 + A_{22})(\lambda_m^2 + A_{33}) - A_{23}^2, \\ Q_{2m} &= A_{13}A_{23} - A_{12}(\lambda_m^2 + A_{33}), \\ Q_{3m} &= A_{12}A_{23} - A_{13}(\lambda_m^2 + A_{22}). \end{aligned} \tag{3.10}$$

Substitution of representation (3.8) into the boundary conditions (3.5) results in a system of linear algebraic equations for the constants β_{1m} ($m = \overline{1,3}$)

$$\mathbf{B} \cdot (\beta_{11},\, \beta_{12},\, \beta_{13})^T = \mathbf{0}. \tag{3.11}$$

The elements of the coefficient matrix $\mathbf{B}$ are

$$\begin{aligned} B_{1m} &= in_1 \exp(h\lambda_m)(Q_{3m}D_m^{-1} + \lambda_m); \\ B_{2m} &= in_2 \exp(h\lambda_m)(Q_{2m}D_m^{-1} + \lambda_m); \\ B_{3m} &= \exp(h\lambda_m)(ic_{12}(n_1 + n_2 Q_{2m}D_m^{-1}) + c_{11}\lambda_m Q_{3m}D_m^{-1}) \quad (m = \overline{1,3}). \end{aligned} \tag{3.12}$$

The coefficients β_{1m} can be expressed from equations (3.11) as

$$\beta_{1m} = \frac{G_m}{M} g_m \quad (m = \overline{1,3}), \tag{3.13}$$

where

$$\begin{aligned} G_1 &= M = B_{22}B_{33} - B_{23}B_{32}, \\ G_2 &= B_{23}B_{31} - B_{21}B_{33}, \\ G_3 &= B_{21}B_{32} - B_{22}B_{31}, \end{aligned} \tag{3.14}$$

and g_m are arbitrary integration constants.

Equation (3.11) has non-trivial solutions if

$$\det \mathbf{B} = 0\,. \tag{3.15}$$

Vanishing of the above determinant yields a transcendental equation for Ω and k, i.e., for the spectrum.

Finally, the complex displacement functions for the normal symmetrical linear waves which propagate in the waveguide plane in an arbitrary direction (n_1, n_2) and belong to the mode q, are

$$\begin{aligned} u_{jq}^{(l)}(x_1,x_2,x_3,t) &= [M_q^{-1} \textstyle\sum_{m=1}^{3} D_{mq}^{-1} g_{mq} Q_{jmq} G_{mq} \beta_{jmq} \exp(\lambda_{mq} x_3)] \times \\ &\times \exp(-i(\omega t - k_q(n_1x_1+n_2x_2))) \quad (j=\overline{1,3}). \end{aligned} \tag{3.16}$$

4. **Analytical solution of a heterogeneous problem for a nonharmonic distortion**

After determining the amplitude functions of linear waves, it becomes possible to obtain the analytical representations for the nonharmonic distortion $u_{jq}^{(n)}$ from (3.2):

$$\begin{aligned} &\rho_0 \ddot{u}_{jq}^{(n)} - c_{jdik} u_{iq,dk}^{(n)} = \textstyle\sum_{l,m=1}^{3} \mu_{jlmq} \exp(-2i(\omega t - \\ &-k_q(n_1x_1+n_2x_2)) + (\lambda_{lq}+\lambda_{mq})x_3); \end{aligned} \tag{4.1}$$

$$\begin{aligned} &(c_{3dik} u_{iq,k}^{(n)})_{x_3=\pm h} = \textstyle\sum_{l,m=1}^{3} \eta_{jlmq} \exp(-2i(\omega t - \\ &-k_q(n_1x_1+n_2x_2)) + (\lambda_{lq}+\lambda_{mq})x_3) \quad (j=\overline{1,3}). \end{aligned} \tag{4.2}$$

In these relations the constants μ_{jlmq} $(j = 1, 2)$ can be written as

$$\begin{aligned} \mu_{jlmq} = a_{jljm}^{lmq} i k_q n_j [2k_q^2(n_j^2\Delta_1 + 3n_k^2\Delta_2) - (\lambda_{lq}^2 + 4\lambda_{lq}\lambda_{mq} + \lambda_{mq}^2)\Delta_2] + \\ + a_{lmml}^{lmq} i k_q [2k_q^2 n_k (n_j^2(2\Delta_4+\Delta_5) + n_k^2\Delta_3) - \\ - n_k(\lambda_{lq}^2\Delta_6 + \lambda_{lq}\lambda_{mq}\ (3\Delta_6+\Delta_7) + \lambda_{mq}^2\Delta_7)] + \\ + a_{llmm}^{lmq} i k_q [2k_q^2 n_k (n_j^2(2\Delta_4+\Delta_5) + n_k^2\Delta_3) - \\ - n_k(\lambda_{lq}^2\Delta_7 + \lambda_{lq}\lambda_{mq}\ (3\Delta_6+\Delta_7) + \lambda_{mq}^2\Delta_6)] + \\ + a_{klkm}^{lmq} i k_q n_j [2k_q^2(n_j^2\Delta_3 + n_k^2(2\Delta_4+\Delta_5)) - \\ - \lambda_{lq}^2\Delta_7 - 2\lambda_{lq}\lambda_{mq}(\Delta_6+\Delta_7) - \lambda_{mq}^2\Delta_6] + \end{aligned}$$

$$+a^{lmq}_{3l3m} ik_q n_j [2k_q^2(n_j^2\Delta_3 + n_k^2(2\Delta_6 + \Delta_7)) - \qquad (4.3)$$
$$-\lambda_{lq}^2\Delta_4 - 2\lambda_{lq}\lambda_{mq}(\Delta_4 + \Delta_5) - \lambda_{mq}^2\Delta_5] +$$
$$+a^{lmq}_{jm3l} k_q^2[(n_j^2(\Delta_4 + 2\Delta_5) + n_k^2(\Delta_6 + 2\Delta_7))\lambda_{lq} +$$
$$+3(n_j^2\Delta_4 + n_k^2\Delta_6)\lambda_{mq} - \lambda_{lq}\lambda_{mq}(\lambda_{lq} + \lambda_{mq})\Delta_3] +$$
$$+a^{lmq}_{jl3m} k_q^2[3(n_j^2\Delta_4 + n_k^2\Delta_6)\lambda_{lq} + (n_j^2(\Delta_4 + 2\Delta_5) +$$
$$+n_k^2(\Delta_6 + 2\Delta_7))\lambda_{mq} - \lambda_{lq}\lambda_{mq}(\lambda_{lq} + \lambda_{mq})\Delta_3] +$$
$$+a^{lmq}_{km3l} k_q^2 n_1 n_2[\lambda_{lq}(\Delta_9 + 2\Delta_{10}) + 3\lambda_{mq}\Delta_9] +$$
$$+a^{lmq}_{kl3m} k_q^2 n_1 n_2[3\lambda_{lq}\Delta_9 + \lambda_{mq}(\Delta_9 + 2\Delta_{10})] \ .$$

If $j = 3$ we have

$$\mu_{3lmq} = 2a^{lmq}_{1m3l} ik_q n_1[k_q^2(n_1^2\Delta_3 + n_2^2(2\Delta_6 + \Delta_7)) -$$
$$-\lambda_{lq}^2\Delta_5 - \lambda_{lq}\lambda_{mq}(3\Delta_4 + \Delta_5) - \lambda_{mq}^2\Delta_4] +$$
$$+2a^{lmq}_{1l3m} ik_q n_1[k_q^2(n_1^2\Delta_3 + n_2^2(2\Delta_6 + \Delta_7)) -$$
$$-\lambda_{lq}^2\Delta_4 - \lambda_{lq}\lambda_{mq}(3\Delta_4 + \Delta_5) - \lambda_{mq}^2\Delta_5] +$$
$$+2a^{lmq}_{2m3l} ik_q n_2[k_q^2(n_2^2\Delta_3 + +n_1^2(2\Delta_6 + \Delta_7)) -$$
$$-\lambda_{lq}^2\Delta_5 - \lambda_{lq}\lambda_{mq}(3\Delta_4 + \Delta_5) - \lambda_{mq}^2\Delta_4] +$$
$$+2a^{lmq}_{2l3m} ik_q n_2[k_q^2(n_2^2\Delta_3 + n_1^2(2\Delta_6 + \Delta_7)) -$$
$$-\lambda_{lq}^2\Delta_4 - \lambda_{lq}\lambda_{mq}(3\Delta_4 + \Delta_5) - \lambda_{mq}^2\Delta_5] +$$
$$+a^{lmq}_{1l1m}(\lambda_{lq} + \lambda_{mq})[k_q^2(n_1^2(2\Delta_4 + \Delta_5) + \qquad (4.4)$$
$$+n_2^2(2\Delta_6 + \Delta_7)) - \lambda_{lq}\lambda_{mq}\Delta_3] +$$
$$+a^{lmq}_{2l2m}(\lambda_{lq} + \lambda_{mq})[k_q^2(n_1^2(2\Delta_6 + \Delta_7) +$$
$$+n_2^2(2\Delta_4 + \Delta_5)) - \lambda_{lq}\lambda_{mq}\Delta_3] +$$
$$+(a^{lmq}_{1m2l} + a^{lmq}_{1l2m})(\lambda_{lq} + \lambda_{mq})k_q^2 n_1 n_2(2\Delta_9 + \Delta_{10}) +$$
$$+a^{lmq}_{3l3m}(\lambda_{lq} + \lambda_{mq})(3k_q^2(n_1^2 + n_2^2)\Delta_2 - \lambda_{lq}\lambda_{mq}\Delta_1).$$

The constants η_{jlmq} $(j=1,2)$ in the boundary conditions (4.2) are

$$\begin{gathered}\eta_{jlmq}=(a^{lmq}_{jm3l}+a^{lmq}_{jl3m})[k_q^2(n_1n_j\Delta_3+n_k^2\Delta_6)-\lambda_{lq}\lambda_{mq}\Delta_4]+\\ +(a^{lmq}_{km3l}+a^{lmq}_{kl3m})k_q^2n_1(n_j\Delta_7+n_2\Delta_6)-\\ -(a^{lmq}_{jljm}n_1\Delta_4+a^{lmq}_{klkm}n_j\Delta_6+a^{lmq}_{3l3m}n_j\Delta_2)ik_q(\lambda_{lq}+\lambda_{mq})-\\ -a^{lmq}_{jllm}ik_q(c_{144}n_1\lambda_{lq}++c_{456}n_k\lambda_{mq})-a^{lmq}_{jmml}ik_q(c_{456}n_k\lambda_{lq}+c_{144}n_1\lambda_{mq})\ .\end{gathered}\tag{4.5}$$

If $j=3$ we have

$$\begin{gathered}\eta_{3lmq}=a^{lmq}_{1l1m}[k_q^2(n_1^2\Delta_5+n_2^2\Delta_7)-\lambda_{lq}\lambda_{mq}\Delta_3]+\\ +a^{lmq}_{2l2m}[k_q^2n_1^2(\Delta_5+\Delta_7)-\lambda_{lq}\lambda_{mq}\Delta_3]+\\ +(a^{lmq}_{1m2l}+a^{lmq}_{1l2m})k_q^2n_1(c_{123}n_1+c_{144}n_2)+\\ +a^{lmq}_{3l3m}[k_q^2(n_1^2+n_2^2)\Delta_2-\lambda_{lq}\lambda_{mq}\Delta_1]-\\ -a^{lmq}_{1m3l}ik_qn_1(\lambda_{lq}\Delta_5+\lambda_{mq}\Delta_4)-a^{lmq}_{1l3m}ik_qn_1(\lambda_{lq}\Delta_4+\lambda_{mq}\Delta_5)-\\ -a^{lmq}_{2m3l}i\times k_q(n_1\lambda_{lq}\Delta_5+n_2\lambda_{mq}\Delta_4)-a^{lmq}_{2l3m}ik_q(n_2\lambda_{lq}\Delta_4+n_1\lambda_{mq}\Delta_5).\end{gathered}\tag{4.6}$$

In equations (4.3)-(4.5)

$$a^{lmq}_{dpsr}=-(2M_q^2D_{lq}D_{mq})^{-1}g_{lq}g_{mq}G_{lq}G_{mq}Q_{dpq}Q_{srq}\beta_{dpq}\beta_{srq};\tag{4.7}$$

$$n_k=\begin{cases}n_1, & j=2;\\ n_2, & j=1.\end{cases}\tag{4.8}$$

Problem (4.1) has the analytical solution of the following structure:

$$\begin{gathered}u^{(n)}_{jq}=[\textstyle\sum_{l,m=1}^3\gamma_{j1lmq}\exp((\lambda_{lq}+\lambda_{mq})x_3)+\\ +\textstyle\sum_{m=1}^3(\gamma_{j2mq}+\gamma_{j3mq}x_3)\exp(2\lambda_{mq}x_3)+\\ +\textstyle\sum_{m=1}^3(\gamma_{j4mq}+\gamma_{j5mq}x_1+\gamma_{j6mq}x_2)\exp(2\lambda_{mq}x_3)]\times\\ \times\exp(-2i(\omega t-k_q(n_1x_1+n_2x_2))).\end{gathered}\tag{4.9}$$

The coefficients γ_{j1lmq} are determined from the linear equation system

$$\mathbf{L}^{(l,m)}\cdot(\gamma_{11lmq},\gamma_{21lmq},\gamma_{31lmq})^T=(\mu_{1lmq},\,\mu_{2lmq},\,\mu_{3lmq})^T\quad(l\neq m),\tag{4.10}$$

where the elements of the matrix $\mathbf{L}^{(l,m)}$ are

$$\begin{gathered} L_{11q}^{(l,m)} = 4k_q^2(c_{11}n_1^2 + c_{44}n_2^2) - c_{44}(\lambda_{lq} + \lambda_{mq})^2 - 4\Omega^2; \\ L_{22q}^{(l,m)} = 4k_q^2(c_{44}n_1^2 + c_{11}n_2^2) - c_{44}(\lambda_{lq} + \lambda_{mq})^2 - 4\Omega^2; \\ L_{33q}^{(l,m)} = 4k_q^2 c_{44}(n_1^2 + n_2^2) - c_{11}(\lambda_{lq} + \lambda_{mq})^2 - 4\Omega^2; \\ L_{12q}^{(l,m)} = L_{21q}^{(l,m)} = 4k_q^2 n_1 n_2 \Delta_8; \\ L_{13q}^{(l,m)} = L_{31q}^{(l,m)} = -2ik_q n_1(\lambda_{lq} + \lambda_{mq})\Delta_8; \\ L_{23q}^{(l,m)} = L_{32q}^{(l,m)} = -2ik_q n_2(\lambda_{lq} + \lambda_{mq})\Delta_8. \end{gathered} \tag{4.11}$$

The coefficients γ_{j2mlq} $(j = \overline{1,3})$ are obtained as

$$\gamma_{j2mq} = \gamma_{12mq} Z_{jmq}^{(2)} (P_{mq}^{(2)})^{-1}, \tag{4.12}$$

where

$$\begin{gathered} Z_{1mq}^{(2)} = P_{mq}^{(2)} = L_{22q}^{(m,m)} L_{33q}^{(m,m)} - (L_{23q}^{(m,m)})^2; \\ Z_{2mq}^{(2)} = [L_{33q}^{(m,m)}(\mu_{2mmq} + \chi_{1mq} - L_{12q}^{(m,m)}\gamma_{12mq}) - \\ -L_{23q}^{(m,m)}(\mu_{3mmq} + \chi_{2mq} - L_{13q}^{(m,m)}\gamma_{12mq})]\gamma_{12mq}^{-1}; \\ Z_{3mq}^{(2)} = [L_{22q}^{(m,m)}(\mu_{3mmq} + \chi_{2mq} - L_{13q}^{(m,m)}\gamma_{12mq}) - \\ -L_{23q}^{(m,m)}(\mu_{2mmq} + \chi_{1mq} - L_{12q}^{(m,m)}\gamma_{12mq})]\gamma_{12mq}^{-1}. \end{gathered} \tag{4.13}$$

The coefficients $L_{srq}^{(m,m)}$ are defined in the same way as in equation (4.11); γ_{12mq} are arbitrary integration constants;

$$\begin{gathered} \chi_{1mq} = 2ik_q n_2 \gamma_{33mq}\Delta_8 + 4c_{44}\gamma_{23mq}\lambda_{mq}; \\ \chi_{2mq} = 2ik_q(n_1\gamma_{13mq} + n_2\gamma_{23mq})\Delta_8 + 4c_{11}\gamma_{33mq}\lambda_{mq}. \end{gathered} \tag{4.14}$$

The coefficients γ_{j3mq} $(j = \overline{1,3})$ have the structure

$$\gamma_{j3mq} = \gamma_{13mq} Z_{jmq}^{(3)} (P_{mq}^{(3)})^{-1}, \tag{4.15}$$

where

$$\begin{gathered} Z_{1mq}^{(3)} = P_{mq}^{(3)} = Z_{1mq}^{(2)}; \\ Z_{2mq}^{(3)} = L_{13q}^{(m,m)} L_{23q}^{(m,m)} - L_{12q}^{(m,m)} L_{33q}^{(m,m)}; \\ Z_{3mq}^{(3)} = L_{12q}^{(m,m)} L_{23q}^{(m,m)} - L_{13q}^{(m,m)} L_{22q}^{(m,m)}, \end{gathered} \tag{4.16}$$

and γ_{13mq} are arbitrary integration constants. The coefficients γ_{j4mq} $(j = 2, 3)$ are

$$\gamma_{j4mq} = \gamma_{14mq} Z_{jmq}^{(4)} (P_{mq}^{(4)})^{-1}, \tag{4.17}$$

where

$$Z_{1mq}^{(4)} = P_{mq}^{(4)} = Z_{1mq}^{(2)};$$

$$Z_{2mq}^{(4)} = [L_{33q}^{(m,m)}(\nu_{1mq} - L_{12q}^{(m,m)}\gamma_{14mq}) -$$

$$-L_{23q}^{(m,m)}(\nu_{2mq} - L_{13q}^{(m,m)}\gamma_{14mq})]\gamma_{14mq}^{-1}; \tag{4.18}$$

$$Z_{3mq}^{(4)} = [L_{22q}^{(m,m)}(\nu_{2mq} - L_{13q}^{(m,m)}\gamma_{14mq}) -$$

$$-L_{23q}^{(m,m)}(\nu_{1mq} - L_{12q}^{(m,m)}\gamma_{14mq})]\gamma_{14mq}^{-1},$$

where the constants ν_{smq} $(s = 1, 2)$ have the structure

$$\nu_{1mq} = 2ik_q(n_1\gamma_{16mq} + n_2\gamma_{15mq})\Delta_8 +$$

$$+4ik_q(n_1\gamma_{25mq}c_{44} + n_2\gamma_{26mq}c_{11}) + 2\gamma_{36mq}\lambda_{mq}\Delta_8, \tag{4.19}$$

$$\nu_{2mq} = 4ik_q c_{44}(n_1\gamma_{35mq} + n_2\gamma_{36mq}) + 2\lambda_{mq}(\gamma_{15mq} + \gamma_{26mq})\Delta_8.$$

The representations for the coefficients γ_{jsmq} $(s = 5, 6)$ are

$$\gamma_{jsmq} = \gamma_{1smq} Z_{jmq}^{(s)} (P_{mq}^{(s)})^{-1},$$

$$Z_{1mq}^{(s)} = P_{mq}^{(s)} = Z_{1mq}^{(2)}; \quad Z_{jmq}^{(s)} = Z_{1mq}^{(3)} \quad (j = 2, 3). \tag{4.20}$$

The coefficients γ_{1s1q} $(s = 5, 6)$ are arbitrary integration constants. The coefficients γ_{1smq} $(s = 5, 6,\ m = 2, 3)$ assume the forms

$$\gamma_{1s2q} = (d_{11q}d_{22q} - d_{12q}^2)^{-1}(d_{22q}\theta_{1sq} - d_{12q}\theta_{2sq});$$

$$\gamma_{1s3q} = (d_{11q}d_{22q} - d_{12q}^2)^{-1}(d_{11q}\theta_{2sq} - d_{21q}\theta_{1sq}), \tag{4.21}$$

where

$$\theta_{1sq} = -i\exp(2h\lambda_{1q})(k_q n_1\gamma_{3s1q} + \lambda_{1q}\gamma_{1s1q}) -$$

$$-ik_q n_1[\exp(2h\lambda_{2q})\gamma_{3s2q} + \exp(2h\lambda_{3q})\gamma_{3s3q}];$$

$$\theta_{2sq} = -c_{12}k_q\exp(2h\lambda_{1q})(n_1\gamma_{1s1q} + n_2\gamma_{2s1q}) -$$

$$-c_{12}k_q n_2[\exp(2h\lambda_{2q})\gamma_{2s2q} + \exp(2h\lambda_{3q})\gamma_{3s3q}] + \tag{4.22}$$

$$+ic_{11}[\lambda_{1q}\exp(2h\lambda_{1q})\gamma_{3s1q} + \lambda_{2q}\exp(2h\lambda_{2q})\gamma_{3s2q} +$$

$$+\lambda_{3q}\exp(2h\lambda_{3q})\gamma_{3s3q}];$$

and

$$d_{1rq} = \lambda_{(r+1)q}\exp(2h\lambda_{(r+1)q});$$

$$d_{2rq} = c_{12}k_q n_1\exp(2h\lambda_{(r+1)q}) \quad (r = 1, 2). \tag{4.23}$$

Finally, the constants γ_{14sq} $(s = \overline{1,3})$ are obtained from the linear equations system

$$\mathbf{H} \cdot (\gamma_{141q}, \gamma_{142q}, \gamma_{143q})^T = (\xi_{1q}, \xi_{2q}, \xi_{3q})^T, \tag{4.24}$$

where the matrix $\mathbf{H}$ is defined as

$$\begin{gathered} H_{1jq} = 2c_{44} \exp(2h\lambda_{jq})(ik_q n_1 Z^{(4)}_{3jq}(P^{(4)}_{jq})^{-1} + \lambda_{jq}); \\ H_{2jq} = 2c_{44} \exp(2h\lambda_{jq})(P^{(4)}_{jq})^{-1}(ik_q n_2 Z^{(4)}_{3jq} + \lambda_{jq} Z^{(4)}_{2jq}); \\ H_{3jq} = 2\exp(2h\lambda_{jq})(ik_q c_{12}(n_1 + Z^{(4)}_{2jq}(P^{(4)}_{jq})^{-1} n_2) + \\ + c_{11} Z^{(4)}_{3jq}(P^{(4)}_{jq})^{-1}) \quad (j = \overline{1,3}). \end{gathered} \tag{4.25}$$

The elements ξ_{jq} $(j = \overline{1,3})$ of the right side (4.24) are

$$\begin{gathered} \xi_{jq} = \textstyle\sum_{l,m=1}^{3} (\eta_{jlmq} - 2ic_{44} k_q n_j \gamma_{31lmq} - \\ - c_{44}(\lambda_{lq} + \lambda_{mq})\gamma_{j1lmq}) \exp((\lambda_{lq} + \lambda_{mq})h) \quad (j = 1, 2); \\ \xi_{3q} = \textstyle\sum_{l,m=1}^{3} (\eta_{3lmq} - 2ic_{12}(n_1 \gamma_{11lmq} + n_2 \gamma_{21lmq}) - \\ - c_{11} \gamma_{31lmq})(\lambda_{lq} + \lambda_{mq}) \exp((\lambda_{lq} + \lambda_{mq})h). \end{gathered} \tag{4.26}$$

Finally, we have obtained closed analytical representations for the second harmonics of normal three-partial waves. These solutions allow us to carry out a detailed analysis of the nonlinear effects for the anisotropic waveguide considered.

5. **Numerical results**

Numerical computations have been made for the cubic system monocrystal germanium layer for waves propagating in the plain Ox_1x_2 along the nonelastoequivalent direction of the crystal, characterized by the angle $\varphi = 15°$.

The analysis of some nonlinear effects for waves which belong to two low linear modes with zero locking frequency has been performed.

For a germanium monocrystal the density and the second and third order nonzero normalized elastic constants have the following values:

$$\begin{gathered} \rho = 5,32; \quad c_{11} = 12,92; \quad c_{12} = 4,79; \quad c_{44} = 6,70; \\ c_{111} = -7,10; \quad c_{112} = -3,89; \quad c_{144} = -2,3; \\ c_{155} = -2,92; \quad c_{123} = -0,18; \quad c_{456} = -0,53. \end{gathered} \tag{5.1}$$

The evaluation of the correlation between the longitudinal and cross horizontal components in the second harmonics of monochromatic normal waves with different frequencies $\Omega_1 = \Omega_4 = 6.92$, $\Omega_2 = \Omega_5 = 9.23$, $\Omega_3 = \Omega_6 = 11.53$ has been obtained. The points j in Figure 1 correspond to the waves with frequencies Ω_j (they have

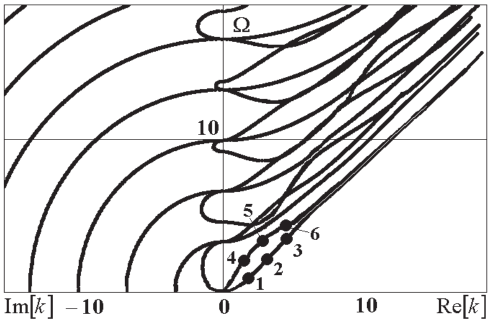

Figure 1. Linear waves spectrum for monocrystal germanium layer

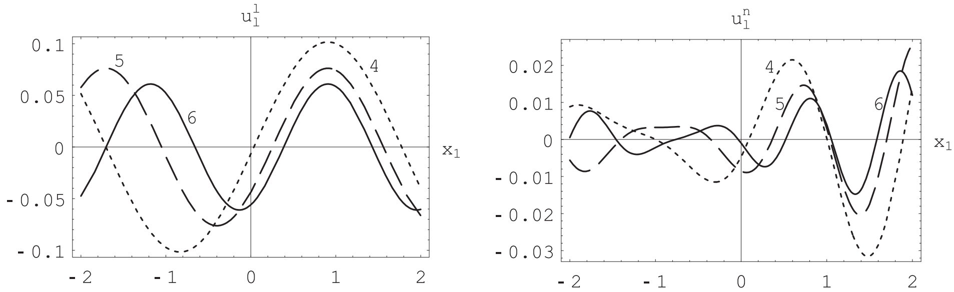

Figure 2. Displacements u_l distributions for $x_3 = 1/2$

been analyzed). These correlations are compared with the correlations between the longitudinal and cross horizontal components in the linear waves.

The longitudinal and cross horizontal components of the normal waves considered are calculated by using the formulas

$$u_l = u_1 \cos\varphi + u_2 \sin\varphi; \quad u_t = -u_1 \sin\varphi + u_2 \cos\varphi, \tag{5.2}$$

where u_1, u_2 are the displacements in linear waves or the second harmonics of linear waves; φ is the angle between the wave propagation direction in the middle waveguide plane and Ox_1 is a coordinate direction.

In Figure 2 the wave functions u_l^l, u_l^n for the waveguide section $\{|x_1| \leq 4h,\ x_2 = 0,\ x_3 = h\}$ and $h = 1/2$ and at time $t = 1$ are depicted. Computations have been made for those waves which belong to the linear spectrum second mode; the curves j correspond to the waves j in Figure 1. The analogous distributions for the waveguide section $\{|x_1| \leq 4h,\ x_2 = 0,\ x_3 = 0\}$ are presented in Figure 3. The values u_l^l, u_l^n are obtained as

$$u_l^l = Re[u_l^{(l)}/\Omega_*^2]; \quad u_l^n = 10^5 Re[u_l^{(n)}/\Omega_*^2]; \quad \Omega_*^2 = \rho\,\Omega^2/\rho_*. \tag{5.3}$$

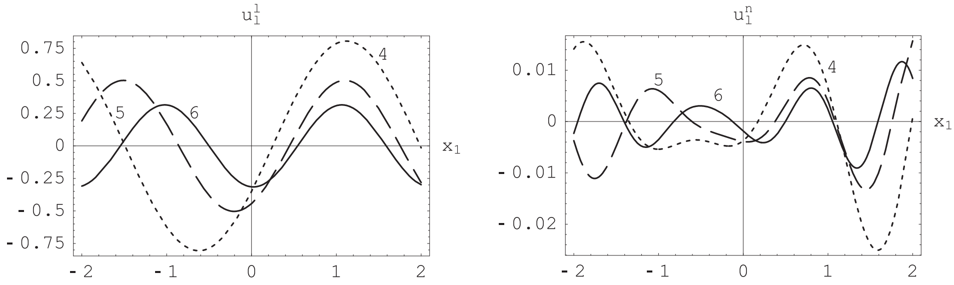

Figure 3. Displacements u_l distributions for $x_3 = 0$

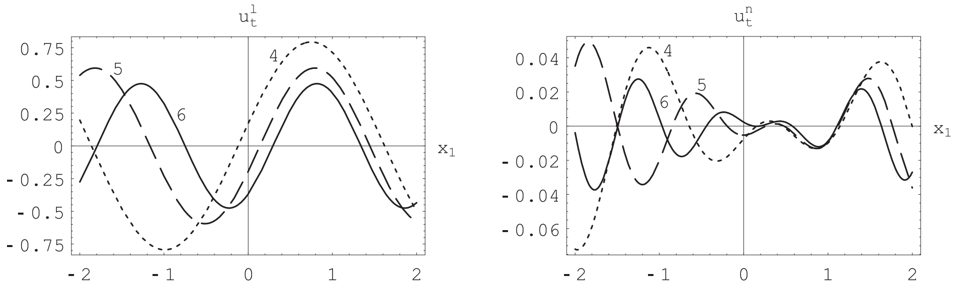

Figure 4. Displacements u_t distributions for $x_3 = 1/2$

In Figures 4 and 5 the wave functions u_t^l, u_t^n are shown for the different waveguide sections $x_3 = 1/2$ and $x_3 = 0$. Here

$$u_t^l = Re[u_l^{(l)}/\Omega_*^2]; \quad u_t^n = 10^5 Re[u_l^{(n)}/\Omega_*^2]; \quad \Omega_*^2 = \rho\,\Omega^2/\rho_*. \tag{5.4}$$

Both for linear waves and for their second harmonics the increasing of frequency leads to an increasing of the displacement maximum. For linear waves and for a non-harmonic distortion the increase in frequency and the changeability of the coordinate x_3 have little influence on u_l and u_t. In case of u_l the more intensive displacements appear in the waveguide area $x_3 = 0$ for linear waves, but the second harmonics are more vividly expressed on the layer surface while $x_3 = 1/2$. For u_t the displacements in linear waves have higher levels on the layer surface $x_3 = 1/2$, but the characteristics for the second harmonics are almost equal.

The graphs in Figure 6 show the distributions of the ratio u_l^n/u_t^n for the waves which correspond to points 1 and 4 in Figure 1, that is for waves with similar frequencies, but belonging to different linear spectrum modes. Computations have been made for the waveguide area $\{|x_1| \leq 2h,\ |x_2| \leq 2h,\ x_3 = 0\}$. It was found that in linear waves the first mode is the pseudotransverse mode, and the second is pseudolongitudinal. From the correlations obtained it is clear that in both cases the second harmonics are the pseudolongitudinal waves, that is the component u_l^n is dominant; for the case of

Ω_1 frequency the dependence is monotonic, and for Ω_4 frequency case the dependence is not continuous.

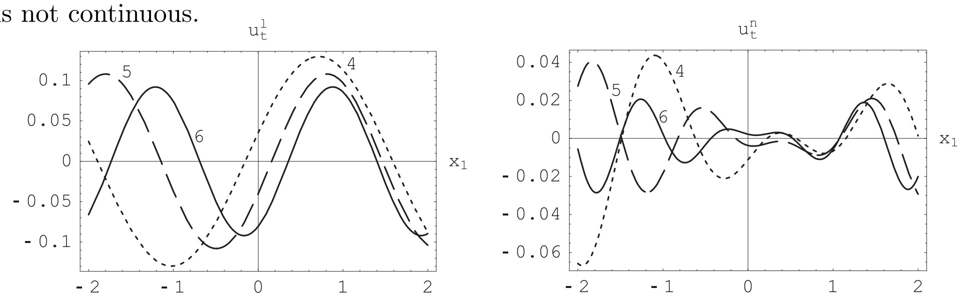

Figure 5. Displacements u_t distributions for $x_3 = 0$

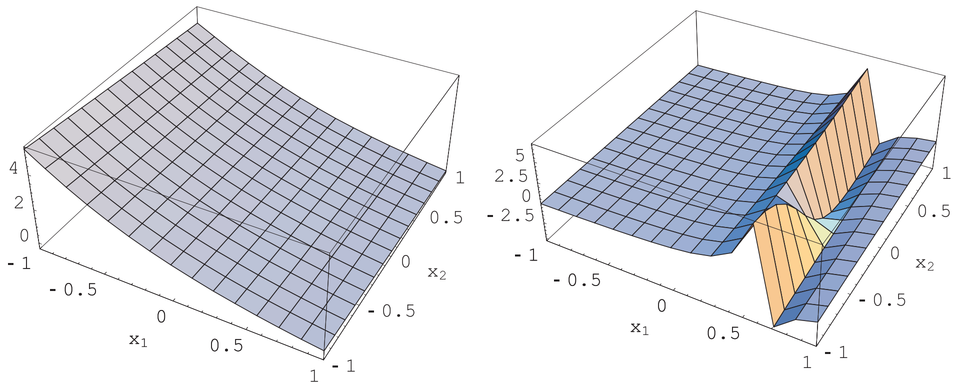

Figure 6. Distributions of $u_l^{(n)}/u_t^{(n)}$ for $x_3 = 0$

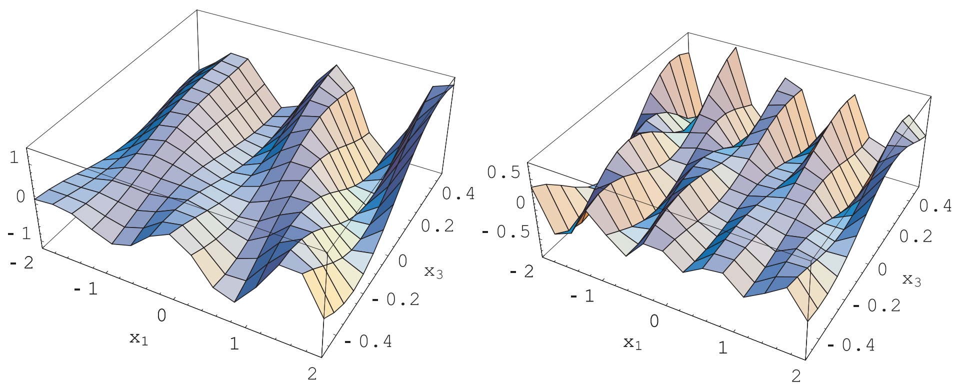

Figure 7. Frequency dependencies of $u_l^{(n)}$ for $x_1 = 0$

In Figure 7 the dependencies u_t^n on frequency for the waveguide section $\{|x_1| \leq 4h,\ x_2 = 0,\ |x_3| \leq h\}$ are shown. The first figure corresponds to frequency Ω_1, the second to frequency Ω_2. From the given data it follows that an increase in the first mode leads to a decrease in the maximum of u_t^n. The displacements themselves are almost constant.

6. Conclusions

The method presented in the paper allows us to analyze the nonlinear normal wave propagation in an arbitrary direction in the plane of anisotropic elastic layer waveguides. We have obtained and analyzed how the frequencies depend on the displacement characteristics, what the distributions for the amplitude characteristics of the linear normal waves are and what second harmonics they have. The data, obtained by this method, could be helpful while using a new class of nonlinear devices for signal information study.

The paper was presented at the 9th International Conference on Numerical Methods in Continuum Mechanics, Zilina, Slovakia, 9-12 September 2003 and its shortened version was published in the Conference CD Proceedings.

References

1. Zarembo L. K., Krasilnicov V. A.: *Nonlinear phenomena in the propagation of elastic waves in solids*. Successes in Phys. Sciens., **102**(4), (1970), 549-584. (in Russian)
2. Truell R., Elbaum C., Chic B.: *Ultrasound Methods in the Physics of Solid Bodies*. Mir, Moscow, 1972. (in Russian)
3. Taker J., Rempton V.: *Hypersound in the Physics of Solid Bodies*. Mir, Moscow, 1975. (in Russian)
4. Goldberg Z. A., Grebneva P. V.: *Nonlinear interaction of longitudinal and two cross waves in isotropic solid*. Acoust. J., **18**(3), (1972), 386-390. (in Russian)
5. Yermilin K. K., Lyamov V. A., Pyatakov P. A.: *Canted interaction of bulk waves in crystals*. Solids Phys., **15**(11), (1973), 3226-3230. (in Russian)
6. Krasilnicov V. A., Lyamov V. E.: *Nonlinear interaction of elastic waves in solids and signal information study*. Acoust. J., **19**(5), (1973), 801-804. (in Russian)
7. Maugin G.: *Nonlinear waves in elastic crystals*. Oxford, University Press, London, 1999.
8. Parker D. F., Mayer A. P., Maradudin A. A.: *The projection method for nonlinear surface acoustic waves*. Wave Motion, **16**, (1992), 151-162.
9. Harvey A. P., Tupholme G. E.: *Propagation of anisotropic elastic and piezo-electric nonlinear surface acoustic waves*. Wave Motion, **16**, (1992), 125-135.
10. Lopen P.O.: *Second-harmonic generation in an elastic surface wave in α-quarts*. J. Appl. Phys., **39**(12), (1968), 5400-5404.
11. Sugimoto M., Majima Y.: *Nonlinear third harmonic resonance of flexural waves on a waveguide of thin elastic plate*, J. Acoust. Sos. Am., **69**(2), (1981), 410-415.

Journal of Computational and Applied Mechanics, Vol. 6., No. 1., (2005), pp. 83–94

BAR ELEMENT WITH VARIATION OF CROSS-SECTION FOR GEOMETRIC NON-LINEAR ANALYSIS

Vladimír Kutiš and Justín Murín
Department of Mechanics, Slovak University of Technology
812 19 Bratislava, Slovak Republic
kutis@elf.stuba.sk

[Received: December 20, 2003]

Abstract. This paper deals with a new bar element with varying cross-sectional area which can be used for geometric non-linear analysis. Shape functions of the bar element include transfer functions and transfer constants, which respect variation of cross-sectional area. Main FE equations are assembled using non-incremental non-linearized method. The von Mises two bar structure with varying cross-sectional area was analyzed. The results obtained with our new element were compared with ANSYS bar element results.

Mathematical Subject Classification: 74S05, 74B20
Keywords: bar element, variation of cross-sectional area, geometric non-linear analysis, finite element method

1. **Introduction**

Even though the solution of geometric non-linear problems is possible, a great deal of time and effort is spent on improving effectiveness and accuracy of non-linear analyses. Commonly used FEM programs use incremental methods, where the Green-Lagrange strain tensor is linearized in total as well as in updated formulation [1]. Furthermore constitutive law is often linearized - relationship between increment of stress tensor and increment of strain tensor.

A new non-incremental Lagrange formulation without linearization has recently been published in [2]. Non-incremental equations are simpler and contain full non-linear stiffness matrices.

In our paper, we use these non-incremental equations to derive a full non-linear stiffness matrix and a full non-linear tangent matrix for a bar element with variation of the cross-sectional area. Variation of the cross-sectional area is defined as polynomial. New shape functions are used - shape functions which reflect variation of cross-sectional area exactly [3].

2. The basic equations set up in a local co-ordinate system

The Green-Lagrange strain tensor of finite deformation in Lagrange formulation can be written as

$$E_{ij} = \frac{1}{2}(u_{i,j} + u_{j,i} + u_{k,i}u_{k,j}) = e_{ij} + \eta_{ij} , \tag{1}$$

where e_{ij} is the linear part of the Green-Lagrange strain tensor and η_{ij} is its non-linear part. u_i represents the i-th component of displacement and $u_{i,j}$ is the gradient of displacement u_i.

The constitutive law can be written as

$$S_{ij} = C_{ijkl}E_{kl} , \tag{2}$$

where C_{ijkl} is the tensor of elastic constants and S_{ij} is II. Piola-Kirchhoff stress tensor.

The principle of virtual work can be written as

$$\delta W^{\text{int}} = \delta W^{\text{ext}} , \tag{3}$$

where δW^{int} and δW^{ext} are the internal and external virtual works. The internal virtual work assumes the form

$$\delta W^{\text{int}} = \int_{V^0} S_{ij}\, \delta E_{ij}\, \mathrm{d}V . \tag{4}$$

For the external virtual work we can write

$$\delta W^{\text{ext}} = \int_{A^0} F_i\, \delta u_i\, \mathrm{d}A + \hat{F}_k\, \delta q_k \tag{5}$$

where F_i is the i-th surface load and δu_i is the appropriate virtual displacement, $\hat{F}_k$ is discrete load at a node and δq_k is the virtual displacement at the same node. The integration is done through the initial volume V^0 and the initial area A^0.

Applying equations (4) and (5) to (3) and considering the displacement as

$$u_i = \phi_{ik}\, q_k , \tag{6}$$

where ϕ_{ik} are shape functions and q_k is nodal displacement, we obtain the classical FEM equation

$$\mathbf{K}(\mathbf{q})\, \mathbf{q} = \mathbf{F} . \tag{7}$$

Matrix $\mathbf{K}(\mathbf{q})$ is a full non-linear stiffness matrix, $\mathbf{q}$ is the vector of local displacements and $\mathbf{F}$ is the vector of external local loads.

The full non-linear stiffness matrix has a linear and a non-linear part

$$\mathbf{K}(\mathbf{q}) = \mathbf{K}^L + \mathbf{K}^{NL}(\mathbf{q}) = \mathbf{K}^L + \mathbf{K}^{NL1}(\mathbf{q}) + \mathbf{K}^{NL2}(\mathbf{q}) + \mathbf{K}^{NL3}(\mathbf{q}) . \tag{8}$$

The nm-th members of the single matrices can be written in the forms

$$K^{L}_{nm} = \frac{1}{4}\int_{V^0} C_{ijkl}(\phi_{km,l} + \phi_{lm,k})(\phi_{in,j} + \phi_{jn,i})\,\mathrm{d}V\ , \tag{9a}$$

$$K^{NL1}_{nm} = \frac{1}{4}\int_{V^0} C_{ijkl}\phi_{pm,k}\phi_{pr,l}(\phi_{in,j} + \phi_{jn,i})q_r\,\mathrm{d}V\ , \tag{9b}$$

$$K^{NL2}_{nm} = \frac{1}{2}\int_{V^0} C_{ijkl}\phi_{pr,i}\phi_{pn,j}(\phi_{km,l} + \phi_{lm,k})q_r\,\mathrm{d}V\ , \tag{9c}$$

$$K^{NL3}_{nm} = \frac{1}{2}\int_{V^0} C_{ijkl}\phi_{pm,k}\phi_{pv,l}\phi_{rq,i}\phi_{rn,j}q_v q_q\,\mathrm{d}V\ , \tag{9d}$$

where $\phi_{pm,k}$ is the first derivative of shape function ϕ_{pm} with respect to the k-th coordinate. Other derivatives in the previous equations have a similar meaning.

3. Stiffness matrices of bar element with variation of cross-section

3.1. **Introductory remarks.** The matrices, which were derived above, are valid for all types of elements whose displacements are described by equation (6). That means that we can use these equations also for a bar element with variation of cross-sectional area.

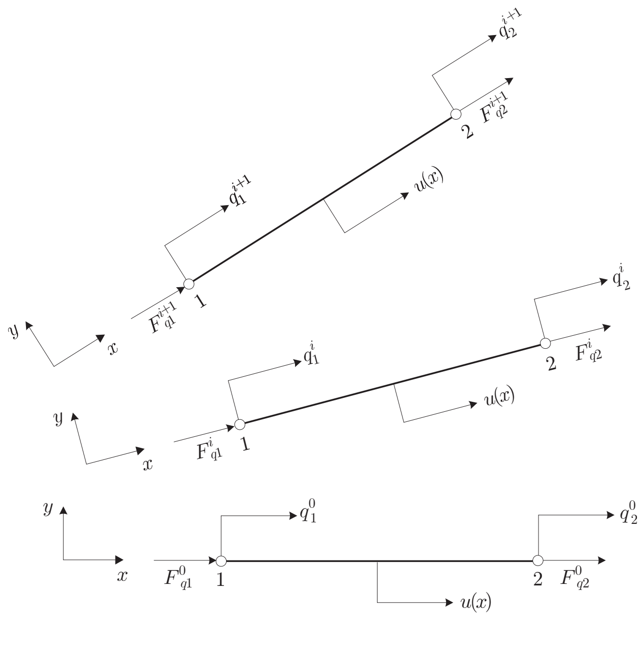

Figure 1. Local nodal displacements and forces in single iterations

In the classical FE codes (e.g. ANSYS), linear interpolation is used for shape functions. But such functions do not respect variation of the element's cross-sectional area and in a very coarse mesh they are responsible for an increase in inaccuracy.

This behavior of bar elements with variation of cross-section with classical linear shape function is also included in linear theory [4].

Figure 1 shows a bar element in a local co-ordinate system with local forces and local displacements in single iterations. The vectors of local displacements and forces have the forms

$$\mathbf{q} = \begin{bmatrix} q_1 & q_2 \end{bmatrix}^T \tag{10}$$

$$\mathbf{F} = \begin{bmatrix} F_{q1} & F_{q2} \end{bmatrix}^T \tag{11}$$

The variation of cross-sectional area $A^0(x)$ is defined as

$$A^0(x) = A_1^0 \eta_A(x) = A_1^0 \Big(1 + \sum_{k=1}^{p} \eta_{Ak} x^k\Big) \tag{12}$$

where A_1^0 is cross sectional area at node 1 and polynomial $\eta_A(x)$ describes variation of the cross-sectional area (η_{Ak} are the coefficients of the polynomial $\eta_A(x)$).

3.2. **Shape functions for bar element with variation of cross-sectional area.** New shape functions for a bar element with variation of cross-sectional area are derived from the direct stiffness method and the whole procedure is published in [3]. The new shape functions contain the transfer functions and transfer constants, which characterize the solution of the linear differential equation with non-constant parameters [5] and depend on polynomial $\eta_A(x)$. For displacement in location x in the local co-ordinate system, we can write

$$u(x) = u_1 - \frac{d'_{N2}(x)}{d'_{N2}} u_1 + \frac{d'_{N2}(x)}{d'_{N2}} u_2 \;, \tag{13}$$

where u_1 and u_2 are displacements in node 1 and 2, respectively, $d'_{N2}(x)$ is transfer function and d'_{N2} is transfer constant (transfer constant is transfer function for $x = L$ and L is length of element).

From equation (13) we can write for shape functions

$$\phi_{11} = 1 - \frac{d'_{N2}(x)}{d'_{N2}} \qquad \phi_{12} = \frac{d'_{N2}(x)}{d'_{N2}} \tag{14}$$

and their derivatives

$$\phi_{11,1} = -\frac{d''_{N2}(x)}{d'_{N2}} \qquad \phi_{12,1} = \frac{d''_{N2}(x)}{d'_{N2}} \tag{15}$$

3.3. **Full non-linear stiffness matrix.** Members of single matrices of a full non-linear stiffness matrix for a bar element with variation of cross-sectional area also have the forms (9a), (9b), (9c) and (9d). Shape functions and their derivations are defined by (14) and (15). For bar elements with linear elastic deformation the tensor of elastic constants C_{ijkl} is characterized by the Young modulus of elasticity E and $\mathrm{d}V$ can be written as $A^0\mathrm{d}x$, where A^0 is undeformed cross-sectional area, which is defined by equation (12). Considering all these equations, we can write for members of $\mathbf{K}^L$

$$K^L_{mn} = A^0_1 E \int_{L^0} \eta_A(x)\phi_{1m,1}\phi_{1n,1}\mathrm{d}x \ . \tag{16}$$

After the integration [3] for the whole matrix $\mathbf{K}^L$ we can write

$$\mathbf{K}^L = \frac{A^0_1 E}{d'_{N2}} \begin{bmatrix} 1 & -1 \\ -1 & 1 \end{bmatrix} . \tag{17}$$

For member of $\mathbf{K}^{NL1}$ we obtained

$$K^{NL1}_{nm} = \frac{1}{4} A^0_1 E \int_{L^0} \eta_A(x)\phi_{1m,1} \left(\phi_{11,1}q_1 + \phi_{12,1}q_2\right) 2\phi_{1n,1}\mathrm{d}x \tag{18}$$

and for the whole matrix $\mathbf{K}^{NL1}$

$$\mathbf{K}^{NL1}(\mathbf{q}) = \frac{1}{2}\frac{A^0_1 E}{(d'_{N2})^3} \begin{bmatrix} 1 & -1 \\ -1 & 1 \end{bmatrix} (q_2 - q_1)\, \bar{d}'_{N2} \ . \tag{19}$$

Similarly we can derive $\mathbf{K}^{NL2}$ and $\mathbf{K}^{NL3}$

$$\mathbf{K}^{NL2}(\mathbf{q}) = \frac{A^0_1 E}{(d'_{N2})^3} \begin{bmatrix} 1 & -1 \\ -1 & 1 \end{bmatrix} (q_2 - q_1)\, \bar{d}'_{N2} \tag{20}$$

$$\mathbf{K}^{NL3}(\mathbf{q}) = \frac{1}{2}\frac{A^0_1 E}{(d'_{N2})^4} \begin{bmatrix} 1 & -1 \\ -1 & 1 \end{bmatrix} (q_2 - q_1)^2\, \bar{\bar{d}}'_{N2} \tag{21}$$

The final full non-linear stiffness matrix (8) can be written using (17), (19), (20) and (21) as

$$\mathbf{K}(\mathbf{q}) = (k^L + k^{NL}) \begin{bmatrix} 1 & -1 \\ -1 & 1 \end{bmatrix} , \tag{22}$$

where

$$k^L = \frac{A^0_1 E}{d'_{N2}} , \tag{23}$$

$$k^{NL} = k^L \left[\frac{3}{2}(q_2 - q_1)\frac{\bar{d}'_{N2}}{(d'_{N2})^2} + \frac{1}{2}(q_2 - q_1)^2 \frac{\bar{\bar{d}}'_{N2}}{(d'_{N2})^3} \right] . \tag{24}$$

As can be seen from the previous equations, the full non-linear stiffness matrix of a bar element with variation of the cross-sectional area contains transfer constant d'_{N2} and two new modified transfer constants $\bar{d}'_{N2}$ and $\bar{\bar{d}}'_{N2}$. Numerical computation of transfer constant d'_{N2} is described in the Appendix, the modified transfer constants $\bar{d}'_{N2}$ and $\bar{\bar{d}}'_{N2}$ are the same transfer constants as d'_{N2}, but the polynomial $\eta_A(x)$ is changed to $(\eta_A(x))^2$ and $(\eta_A(x))^3$, respectively.

3.4. **Full non-linear tangent matrix.** The system of equations (7) with stiffness matrix in form (22) is non-linear, which is usually solved using the Newton-Raphson method. This iteration method makes use of derivatives of single functions of a system whose solution is being found, and that is why the full tangent stiffness matrix is required to be built.

In the formal way, the tangent stiffness matrix can be derived as

$$\begin{aligned}\mathbf{K}_T(\mathbf{q}) &= \frac{\partial \mathbf{F}}{\partial \mathbf{q}} = \frac{\partial \mathbf{K}(\mathbf{q})}{\partial \mathbf{q}}\mathbf{q} + \mathbf{K}(\mathbf{q}) = \frac{\partial \mathbf{K}^{NL}(\mathbf{q})}{\partial \mathbf{q}}\mathbf{q} + \mathbf{K}^{NL}(\mathbf{q}) + \mathbf{K}^L \\ &= \mathbf{K}^L + \mathbf{K}^{NLT}(\mathbf{q})\end{aligned} \tag{25}$$

Using equations (22), (23), (24) and (25) we can write the full non-linear stiffness matrix for a bar element with variation of cross-sectional area as

$$\mathbf{K}_T(\mathbf{q}) = (k^L + k^{NLT}) \begin{bmatrix} 1 & -1 \\ -1 & 1 \end{bmatrix}, \tag{26}$$

where k^L is defined by equation (23) and

$$k^{NLT} = k^L \left[3(q_2 - q_1)\frac{\bar{d}'_{N2}}{(d'_{N2})^2} + \frac{3}{2}(q_2 - q_1)^2 \frac{\bar{\bar{d}}'_{N2}}{(d'_{N2})^3} \right] \tag{27}$$

For the evaluation of the efficiency of the iteration procedure, we use the Euclidean norm of residual forces, which is compared with the norm of external nodal forces multiplied by a very small coefficient ϵ.

4. **Implementation**

The whole process of a bar element with variation of cross-sectional area for geometric non-linear problems was prepared in Fortran language. Solution for the transfer functions were taken from our program RAM3D [7], which was designed for linear problems and handled the beam element with variation of cross-sectional characteristics.

For the evaluation of the efficiency of the iteration procedure, we use the Euclidean norm of residual forces, which is compared with the norm of external nodal forces multiplied by the coefficient ϵ. More details about internal forces, residual forces, norms of residual forces and iteration process are published in [3].

5. **Numerical experiments**

The convenience of our new bar element with variation of cross-sectional area for geometric non-linear problems is illustrated in the next example. Figure 2 shows a simple arch structure assembled of two bar elements with variation of cross-sectional area - a well-known snap-through problem.

The material properties of the bars are defined by the Young modulus of elasticity $E = 2.1 \times 10^{11}$ Pa. The geometry is given by the parameters $L^0 = 1$ m and $\alpha = 15^\circ$.

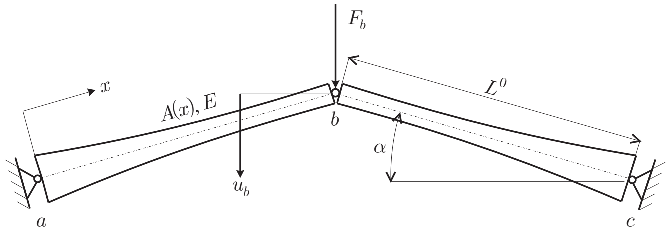

Figure 2. Snap-through problem

We considered four types of cross-sectional area $A(x)$ - from linear polynomial to fourth order polynomial. These have the following forms

type A

$$A(x) = 0.005 - 0.0047x \ ,$$

type B

$$A(x) = 0.005 - 0.0094x + 0.0047x^2 \ ,$$

type C

$$A(x) = 0.005 - 0,0141x + 0.0141x^2 - 0.0047x^3 \ ,$$

type D

$$A(x) = 0.005 - 0.0188x + 0.0282x^2 - 0.0188x^3 + 0.0047x^4 \ .$$

All cross-sectional areas are shown in Figure 3.

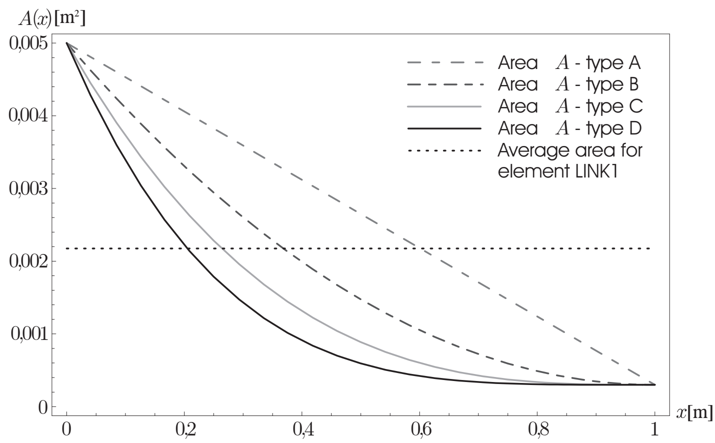

Figure 3. All types of cross-sectioal areas $A(x)$ considered

The goal is to find dependence between displacement u_b and load F_b.

The solution was obtained by our program NelinPrut, in which the new bar element is implemented, and comparative results were obtained from program ANSYS.

In our NelinPrut program, each bar was represented by one element only, but the variation of cross-sectional area was described exactly. In program ANSYS, there are two suitable elements - the classical bar element LINK1 or the beam element with variation of cross-sectional characteristics BEAM54. But the bar element LINK1 is developed for constant cross-sectional area and that is why we should compute some average area according to [6] (see Figure 3). In LINK1 we use also one element only. Element BEAM54 is more suitable, because it is developed for varying cross-sections and because we could refine mesh. But this element does not describe variation of the cross-section exactly, either.

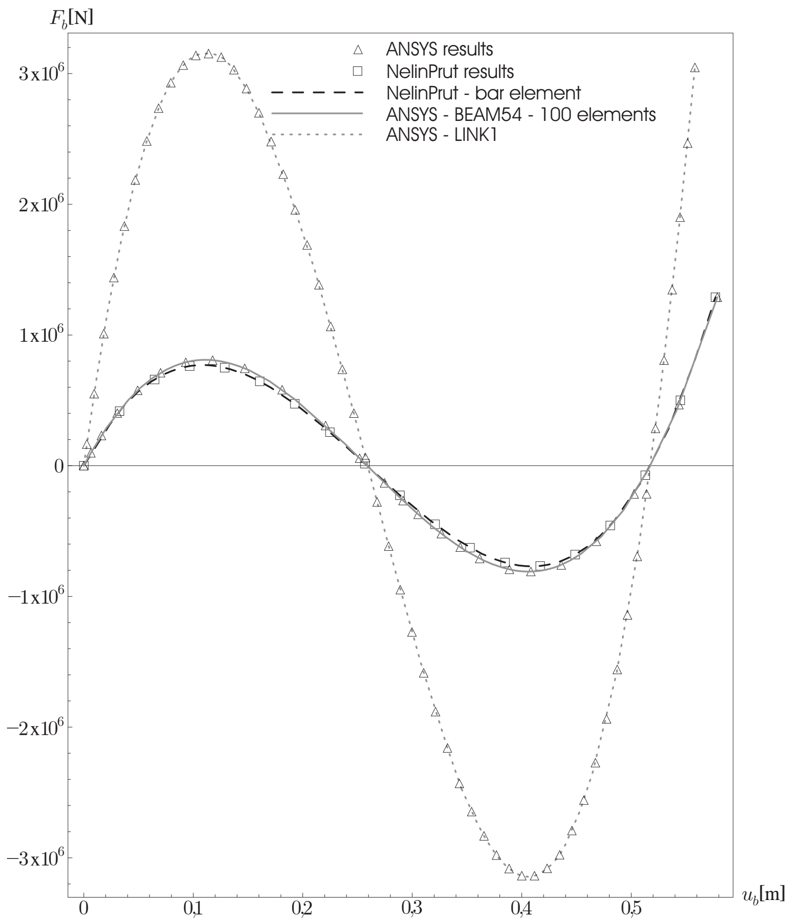

Figure 4. Snap-through problem: dependence between u_b and F_b for type D

Figure 4 shows results for cross-sectional area type D. In this Figure, there are 3 equilibrium paths. The equilibrium paths of the new bar element and BEAM54 with 100 elements are very similar but the equilibrium path of LINK1 is different. Differences between our results and BEAM54 and LINK1 results are caused by linearization of the Green-Lagrange strain tensor and also by variation of cross-sectional area. While our new bar element has shape functions which respect variation of cross-sectional area, BEAM54 and LINK1 use classical shape functions, which do not respect variation of cross-section. BEAM54 results are more accurate than LINK1 results because BEAM54 allows refinement: there are 100 elements and then variation of cross-sectional area is described more suitable than in LINK1.

Variation	NelinPrut		ANSYS-BEAM54 100 elements	
Type	u_b [mm]	IT	u_b [mm]	IT
A	6.6510	7	6.6171	8
B	12.872	8	12.750	10
C	17.958	9	17.744	11
D	21.872	10	21.574	12

Table 1. Snap-through problem: displacement u_b and number of iterations IT for load $F_b = 0,3 \times 10^6$ N for single types of cross-sectional areas A

Variation	NelinPrut		ANSYS-BEAM54 100 elements	
Type	u_b [mm]	IT	u_b [mm]	IT
A	13.927	9	13.777	10
B	28.490	12	27.854	13
C	42.165	15	40.811	17
D	54.635	19	52.290	21

Table 2. Snap-through problem: displacement u_b and number of iterations IT for load $F_b = 0,6 \times 10^6$ N for single types of cross-sectional areas A

Tables 1 and 2 show displacement u_b as function of F_b for all four types of cross-section variation for the new bar element and BEAM54. Table 1 shows results for load $F_b = 0,3 \times 10^6$ N and Table 2 for load $F_b = 0,6 \times 10^6$ N. As can be seen from the Tables, the difference between our and ANSYS results grows with increasing load, where the linearization of the Green-Lagrange strain tensor has more influence on result accuracy. The numbers of iterations IT are nearly equal.

Influence of mesh refinement is shown in Figure 5. We can see that for cross-sectional area type D – this is the most complicated variation –, ANSYS results for BEAM54 are not exactly the same as our new bar element results, neither for refinement. The difference is caused by linearization of the strain tensor mentioned above.

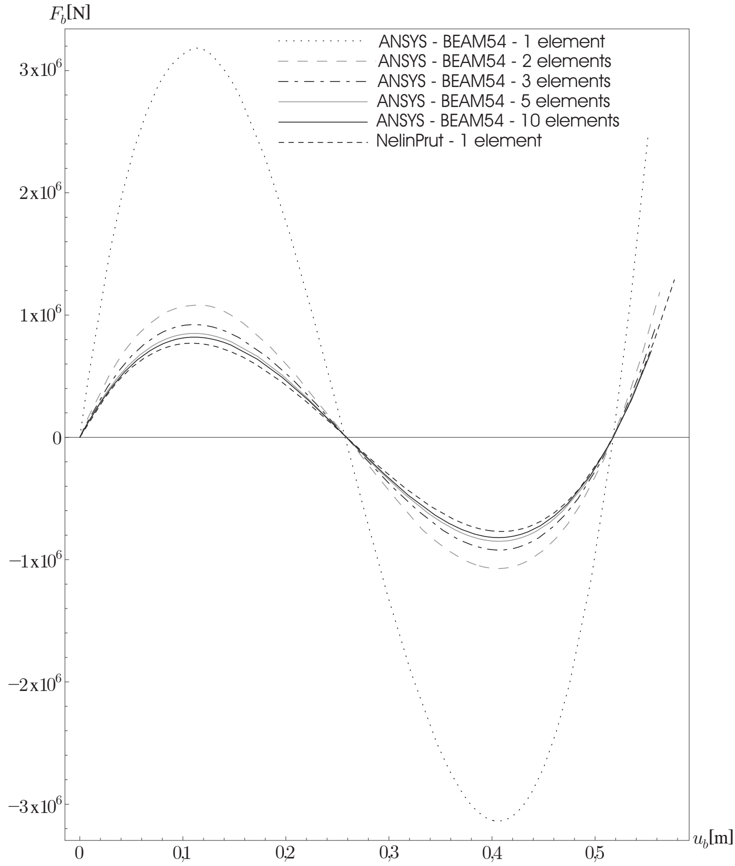

Figure 5. Snap through problem: influence of mesh refinement of BEAM54 element, cross-sectional area type - D

ANSYS - BEAM54		
N_{elem}	u_b [mm]	IT
1	5.0394	5
2	15.648	7
4	19.808	9
6	20.754	9
8	21.106	10
10	21.273	10
20	21.500	10
50	21.565	11
100	21.574	12

NelinPrut		
N_{elem}	u_b [mm]	IT
1	21.872	10

Table 3. Snap-through problem: displacement u_b and the number of iterations IT for load $0F_b = 0.3 \times 10^6$ N for type D as mesh density function

ANSYS - BEAM54		
N_{elem}	u_b [mm]	IT
1	10.383	6
2	35.157	11
4	46.778	15
6	49.677	16
8	50.786	17
10	51.320	18
20	52.051	18
50	52.260	21
100	52.290	21

NelinPrut		
N_{elem}	u_b [mm]	IT
1	54.635	19

Table 4. Snap-through problem: displacement u_b and number of iterations IT for load $F_b = 0,6 \times 10^6$ N for type D as mesh density function

Furthermore Tables 3 and 4 show a difference between our results and ANSYS results in the increasing number of BEAM54 elements in ANSYS.

6. Conclusion

The bar element with variation of cross-sectional area presented was derived without any linearization of the Green-Lagrange strain tensor or constitutive law. The method of solution is non-incremental.

As can be seen from the results, the linearization of the terms mentioned has influence on result accuracy also in refinement of mesh, because the main equations, which are used as equilibrium equations, are still linearized: the difference between our results for one bar element and 100 BEAM54 elements of ANSYS. Shape functions also have an influence on results: difference between our results for one bar element with the new shape functions and one bar LINK1 element of ANSYS, but this influence can be eliminated by refinement.

Numerical experiments confirm the applicability of the new bar element with variation of cross-sectional area with new shape functions for non-linear problems and it could be an alternative to the classical bar element with linear shape functions.

We remark that the paper was presented at the 9th International Conference on Numerical Methods in Continuum Mechanics, Zilina, Slovakia, 9-12 September 2003 and its shorter version was published in the Conference CD Proceedings.

References

1. Washizu, K.: *Variational Methods in Elasticity and Plasticity.* Pergamon Press, Oxford, 1975.
2. Murín, J.: Implicit non-incremental FEM equations for non-linear continuum. *Strojnícky časopis,* **52**, (2001), 147-158.

3. KUTIŠ V.: Beam element with variation of cross-section which satisfies all local and global equilibrium conditions. *PhD Thesis*, FEI STU, Bratislava, 2001.

4. MURÍN, J., and KUTIŠ, V.: 3D - beam element with continues variation of the cross-sectional area. *Computers and Structures,* **80**, (2002), 329-338.

5. RUBIN, H.: Analytische Lösung linearer Differentialgleichungen mit veränderlichen Koeffizienten und baustatische Anwendung. *Bautechnik,* **76**, 1999.

6. ANSYS 5.6 - *Theory Manual.* SAS IP, 1999.

7. KUTIŠ, V., and MURÍN, J.: RAM3D - program for statical analysis of frame structures. *Program code*, FEI STU, Bratislava, 2003.

APPENDIX

Determination of the transfer functions and transfer constants occurring in the stiffness matrix and shape functions is based on the following expression

$$d''_{Nj+2}(x) = \frac{a_j(x)}{\eta_A(x)} \ ,$$

where the function $a_j(x) = \frac{x^j}{j!}$ for $j \geq 0$, and for $j \leq 0$, $a_0 = 1$, $a_j = 0$. Closed solutions for the 1st and 2nd integrals of the function $d''_{Nj+2}(x)$ are known only for lower degree polynomials $\eta_A(x)$. For their numerical solution, which is more general, a recurrance rule was derived

$$d^{(n)}_{Nj}(x) = a_{j-n}(x) - \sum_{k=1}^{m} \eta_{Ak} \, \frac{(j-2+k)!}{(j-2)!} \, d^{(n)}_{Nj+k}(x) \qquad \text{for} \quad j \geq 2 \ , \ n = 0 \text{ a } 1 \ .$$

After some manipulation we get

$$d^{(n)}_{Nj}(x) = a_{j-n}(x) \, \sum_{t=0}^{\infty} \beta_{t,0}(x) \ ,$$

where $\beta_{t,0}(x)$ is expressed by

$$\beta_{t,0}(x) = - \sum_{k=1}^{m} \left[\eta_{Ak} \beta_{t,k}(x) \prod_{r=-k}^{-1} (s-1+r) \right]$$

with parameters

$$s = 1 + t \qquad e = \frac{x}{s-n} \qquad \beta_{t,k} = e\beta_{t-1,k-1} \qquad \text{for} \quad k = 1, ...m$$

and initial values

$$\beta_{0,0} = 1 \qquad \beta_{0,k} = 0 \qquad \text{for} \quad k = 1, ...m \ .$$

Journal of Computational and Applied Mechanics, Vol. 6., No. 1., (2005), pp. 95–105

NUMERICAL PREDICTION OF AIRFOIL STALL

Zoran Milas
Faculty of Electrical Engineering, Mechanical Engineering and Naval Architecture
University of Split, 21 000 Split, Croatia
zmilas@fesb.hr

[Received: April 5, 2004]

Abstract. Prediction of the airfoil characteristics, particularly for large incidence angles when stall occurs, depends on the prediction of separation. Turbulent flow around NACA 0012 airfoil in the range of incidence angles from 0^o up to stall angle at $Re = 2.8\,10^6$ is calculated by applying the finite volume method with modified $k-\varepsilon$ turbulence model. A grid independent solution is achieved on the C-type grid around airfoil with 1664*320 control volumes for the finest grid in multigrid procedure. Inclusion of the laminar part by prescribing transition is required in order to bring the calculated data closer to the experimental ones. Very good agreement is obtained between the calculated and the experimental values of the lift-drag coefficients and the pressure coefficient distribution at moderate incidence angles. The peak values of the lift coefficient in the stall area are underpredicted. Trailing edge separation bubble appears at 18^0.

Mathematical Subject Classification: 76F99
Keywords: turbulent flow, finite volume method

1. **Introduction**

Operation of turbomachines at off-design conditions (even close to the best efficiency point) is frequently accompanied by stall. This is due to design aspirations for high specific outputs and consequently high lift coefficients. An increase of the inflow angle α at off-design conditions causes the stalling of the lift curve $c_L(\alpha)$ and its decline further on (deep stall).

Aerodynamic characteristics of axial turbomachines, particularly of those with low rotor 'solidity', are largely determined by their airfoil characteristics. Airfoil stall controls most of the blade stall smeared by 3D effects at the root and tip areas.

Accurate prediction of airfoil stall depends on accurate prediction of the separation point, i.e. the size of the separation area. Separation deteriorates pressure distribution on the airfoil suction side and diminishes lift. The difference between experiments and computation, characterized by delay in predicting separation, indicates that separation is quite sensitive to the correct modelling of flow in the area upstream to the separation point [1]. This area is characterized by a strong adverse streamwise pressure gradient and vanishing shear stress, i.e., skin friction. Transition from laminar to turbulent flow also frequently precedes trailing edge separation. Modifications contributing to a better prediction of skin friction are expected to improve stall predicting capabilities.

Symmetrical NACA 0012 airfoil is chosen for testing numerical predictability of airfoil flow because of rather comprehensive data on its integral and local aerodynamic characteristics measured by various researchers in different wind tunnels. Most of the available data on local characteristics: pressure distribution, location of separation and transition points, comes from the measurements of Gregory [2] . Lift characteristic of Gregory at moderate incidence angles is almost identical with measurements of Abbot [3] and the results compiled by Lazauskas [4]. The latter is mostly based on the SANDIA Report 80-2114, Sheldahl (1981). Experiments with NACA 00 series at $\mathrm{Re}\approx 1.5\cdot 10^6$ [5] indicate that separation starts at the trailing edge and moves towards the airfoil leading edge. Separation appears at larger incidence angles for thinner airfoils. However, its streamwise expansion with increasing incidence angle is more sudden for thinner airfoils. Gregory [2] reports on a thin and small leading edge separation bubble that vanishes close to the stall and appears again in post stall. Accordingly, the stall is provoked by the trailing edge separation expansion.

The Reynolds number at which airfoil flow is calculated equals that of the experiments $\mathrm{Re}=2.88\ 10^6$ [2] allowing for straightforward comparison.

2. **Numerical modelling**

The academic research computer program CAFFA [6,7], which is based on the finite volume method, is used in the flow analysis. Transport equations are developed in the Cartesian coordinate directions with Cartesian velocity components $\bar{v}_j$:

$$\frac{\partial}{\partial x_j}(\rho \bar{v}_j \bar{\Phi} - \Gamma_\Phi \frac{\partial \bar{\Phi}}{\partial x_j}) = S_\Phi \ , \tag{2.1}$$

where

$$\bar{\Phi} = [1,\, \bar{u},\, \bar{v},\, \bar{k},\, \bar{\varepsilon}] \ , \tag{2.2a}$$

$$\Gamma_\Phi = [0,\, \mu_\ell + \mu_t,\, \mu_\ell + \mu_t,\, \mu_\ell + \mu_t/\sigma_k,\, \mu_\ell + \mu_t/\sigma_\varepsilon] \tag{2.2b}$$

are the transport variables, the diffusion coefficients and

$$S_\Phi = [S_1,\, S_u,\, S_v,\, S_k,\, S_\varepsilon] \ , \tag{2.2c}$$

$$S_1 = 0, \quad S_u = -\frac{\partial \bar{p}}{\partial x} + \frac{\partial}{\partial x}(\mu_E \frac{\partial \bar{u}}{\partial x}) + \frac{\partial}{\partial y}(\mu_E \frac{\partial \bar{v}}{\partial x}) \, ,$$

$$S_v = -\frac{\partial \bar{p}}{\partial y} + \frac{\partial}{\partial y}(\mu_E \frac{\partial \bar{v}}{\partial y}) + \frac{\partial}{\partial x}(\mu_E \frac{\partial \bar{u}}{\partial y}), \quad S_k = \rho \bar{P}_k - \rho \bar{\varepsilon} \, ,$$

$$S_\varepsilon = \frac{\rho \bar{\varepsilon}}{\bar{k}}(C_{\varepsilon 1} \bar{P}_k - C_{\varepsilon 2} \bar{\varepsilon})$$

are the source-sink terms, respectively. The transport equations are integrated over the body-fitted curvilinear non-staggered grid. Convective terms in the transport equations are linearized according to Picard and discretized by upwind differencing scheme blended with deferred central differencing scheme. Variables are stored in the central nodes [8]. Standard $k-\varepsilon$ turbulence model with wall functions is used. Calculation of the average value of turbulence kinetic energy production $\bar{P}_k$ and dissipation $\bar{\varepsilon}$ in the wall volumes is modified. Modification is based on the boundary layer DNS data [9] and asymptotic analysis and it accounts for non-equilibrium between production $\bar{P}_k$ and dissipation $\bar{\varepsilon}$ in viscous and buffer sublayer. Values of the constants C_μ, $C_{\varepsilon 1}$, $C_{\varepsilon 2}$, σ_k, σ_ε in the turbulence model are 0.09, 1.44, 1.92, 1.0, 1.3. The coupling procedure in solving momentum and continuity equation is of the SIMPLE type.

Standard $k-\varepsilon$ model of turbulence is surpassed by models that are more complex. However, simplicity-robustness still makes this model a part of many CFD packages for engineering applications. Computation of separating flows using $k-\varepsilon$ model overpredicts skin friction upstream of separation [10] and consequently may fail to predict location of zero skin friction, i.e. point of separation. Modifications to standard $k-\varepsilon$ model to be described here were tested on channel flow [11]. Slightly lower values of channel skin friction, which agree better with experiments, were obtained with the modified $k-\varepsilon$ model. It is expected that these modifications will contribute to a better prediction of separated airfoil flow. Deficiency of $k-\varepsilon$ model lies among others

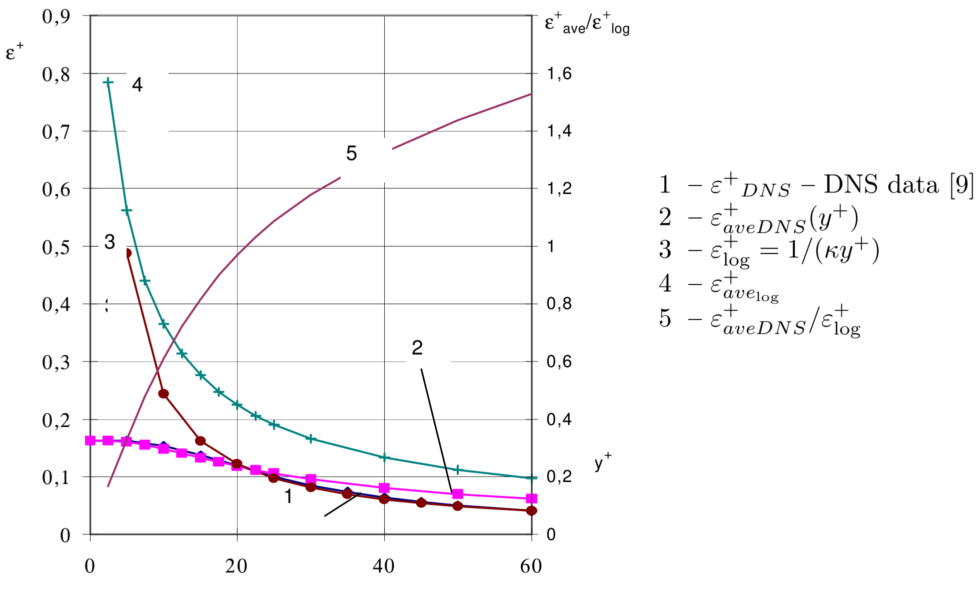

Figure 1. Dissipation of turbulence kinetic energy ε^+ near the wall
ε^+_{ave} – average value in the wall volume (volume height 2y$^+$)

in inadequate modelling of terms of the k and ε equation in the near wall region. The problem is bridged over by means of the wall functions. The local equilibrium of turbulence kinetic energy production $\bar{P}_k$ and dissipation $\bar{\varepsilon}$ is the basic assumption of the wall functions, which is valid only in the log layer $\bar{u}^+ = \frac{1}{\kappa}\ln(Ey^+)$.

Scarce measurements and DNS (direct Navier Stokes solver) data [9],[12],[13],[14] indicate that $\bar{P}_k$ and $\bar{\varepsilon}$ behavior in the near wall region is far from equilibrium and far from log formulation $\bar{\varepsilon}^+_{\log} = \bar{P}^+_{k\,\log}(y^+) = 1/(\kappa y^+)$ as well, Figure 1.

Effect of modifying near wall production and dissipation in k equation are closely related to their contribution to the discretized form of k equation in the finite volume method:

$$a^{(t1)}_{P_k}\bar{k}_P = \sum_{nb} a_{nb_k}\bar{k}_{nb} + S^{(t1)}_k \ , \tag{2.3}$$

where $\bar{k}_P, \bar{k}_{nb}$ represent values of turbulence kinetic energy in the central node of the wall volume and the neighboring nodes. Source term $S^{(t1)}_k$ absorbs right-hand terms of equation (2.1), i.e. their integral contribution over the control (wall) volume:

$$\int\limits_{\Delta V} \rho\bar{P}_k\,\mathrm{d}V - \int\limits_{\Delta V} \rho\bar{\varepsilon}\,\mathrm{d}V = \rho\bar{P}_{k_{ave}}\Delta V - \rho\bar{\varepsilon}_{ave}\Delta V \tag{2.4}$$

Average values of production/dissipation $\bar{P}_{k_{ave}}/\bar{\varepsilon}_{ave}$ [6] are calculated explicitly based on the values from the previous iteration step. Assumption of local equilibrium ($\bar{P}_k = \bar{\varepsilon}$) and representation of average values with central node values [6],[7] make $S^{(t1)}_k$ insensitive to the modelling of dissipation and production. However, dissipation term is rearranged $\bar{\varepsilon}_{ave}\Delta V \approx (\bar{\varepsilon}_{ave}/\bar{k}^{(o)}_P)\bar{k}_P\ \Delta V$ and central node coefficient $a^{(t1)}_{P_k}$ is corrected to $a_{P_k} = a^{(t1)}_{P_k} + \rho\bar{\varepsilon}_{ave}/\bar{k}^{(o)}_P\Delta V$. This computational redistribution aimed to provide positive values of turbulence kinetic energy leaves production $\bar{P}_k$ as a single contributor to the source term of k equation. Accurate representation of $\bar{P}_k$ and $\bar{\varepsilon}$ averages therefore becomes important also from the computational standpoint.

Average values of dissipation and production are calculated using DNS data $\bar{P}^+_k(y^+)$, $\bar{\varepsilon}^+(y^+)$ [9] and assuming that distribution of dissipation/production in dimensionless coordinates $\bar{P}^+_k = \bar{P}_k/(u^4_{\tau w}/\nu_l)$, $\bar{\varepsilon}^+ = \bar{\varepsilon}/(u^4_{\tau w}/\nu_l)$ is independent of Re number. As far as production is concerned this is supported by experiments for boundary layer flows with zero pressure gradient [15].

Outside the near wall region, DNS data exhibit an equilibrium between production and dissipation, which follows log formulation. Asymptotic analysis supports the finite value of dissipation as predicted by DNS on the wall balanced with viscous diffusion of the turbulence kinetic energy. Near the wall dissipation changes slowly, almost linearly.

In order to make it easier to implement modifications into existing $k-\varepsilon$ models, where $\bar{\varepsilon}_{ave} = \bar{\varepsilon}_{\log}$, a correction function f_ε is introduced:

$$\bar{\varepsilon}_{ave} = \bar{\varepsilon}_{\log} f_\varepsilon \quad f_\varepsilon = \frac{1}{2}\left[1 + \ln\frac{y^+_P}{y^+_{o_\varepsilon}} + \ln 2\right] \ , \tag{2.5}$$

$y^+_{o_\varepsilon}$ limits the near wall region in which the constant value of dissipation up to the wall is assumed. $y^+_{o_\varepsilon} \approx 17$ provides best fit to DNS data in Figure 2.

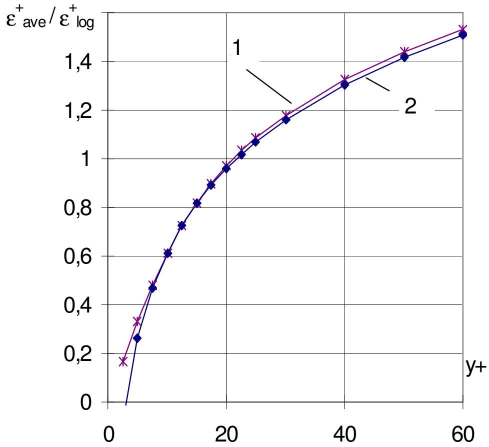

1 – $\bar{\varepsilon}^+_{aveDNS}/\bar{\varepsilon}^+_{P\,\log}$
2 – approximation of 1) with f_ε [11]

Figure 2. Ratio of the average value of dissipation in the wall volume $\varepsilon^+_{aveDNS}(y^+_P)$ and local (log) value in the volume central node P) $\bar{\varepsilon}^+_{P\,\log} = P^+_{kP\,\log} = 1/(\kappa y^+_P)$

The modification of production is analogous to the modification of dissipation. Constant $y^+_{o_k}$ in the correction function $\bar{P}^+_{k_{ave}}/\bar{P}^+_{k_{\log}} = f_{P_k} \approx \frac{1}{2}\left[c_{P_k} + \ln(y^+/y^+_{ok}) + \ln 2\right]$ corresponds to the maximum of production in the near wall region according to DNS data. c_{P_k}equals 0.5 assuming linear steep rise of production from the wall to $y^+_{o_k}$and log formulation further on. Approximation of DNS data gives $c_{P_k} \approx 0.8$.

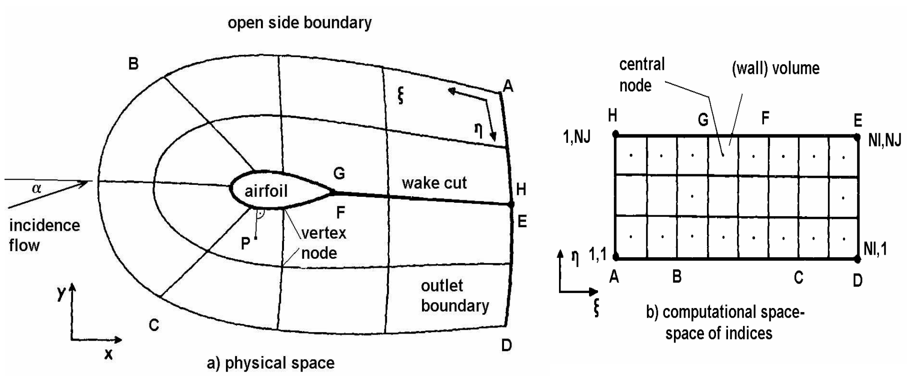

Figure 3. a) C-grid around airfoil, b) computational space- space of indices

The grid generated around airfoil is C-type with the cut along the airfoil wake, Figure 3. Open side boundaries (A-B, C-D) and exit boundary (A-D) are generated as simple straight lines located 4-5 c and 7c (c-chord length) respectively, far from the airfoil. The grid is kept fixed and the incidence angle is varied by skewing the incidence flow. It is assumed that location of side boundaries 4-5 c from the airfoil allows for prescribing inlet boundary conditions along A-B-C-D for all incidence angles between 0-20^0. Interior grid points are generated by applying two - boundaries technique.

Arrangement of the grid points along the airfoil leading edge is of great concern due to high curvature and expected high pressure/shear stress gradients. Preliminary 'panelization' of the airfoil is based on the conformal mapping of a circle into foil. Chordwise location x/c of mapped points is initially the same as for an infinitely thin airfoil, Eppler [16] .

Mapping is presented in Figure 4.a where θ indicates location of the points on the original circle. Equidistant distribution of original points along (semi)circle (N_{pan}=50) provides satisfactory panelization of the airfoil leading edge. Stretching of the airfoil panels $\Delta s(i)/\Delta s(i-1)$ shown in Figure 4b, however, indicates excessive shrinking around the airfoil tail. Slightly better results are obtained by increasing the number

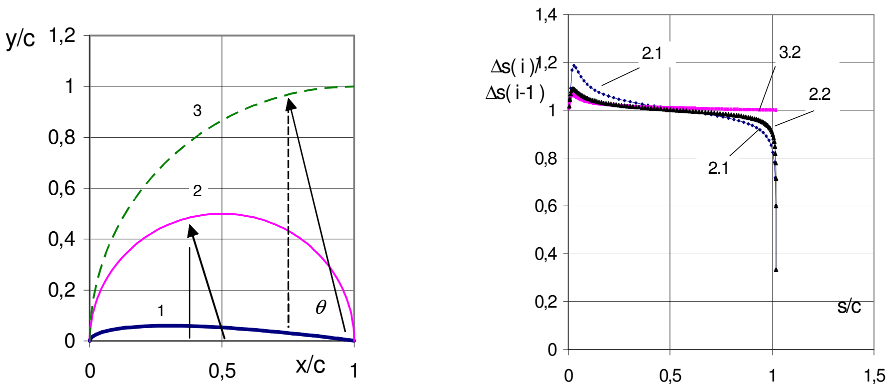

1 – airfoil contour — 2.1 – N_{pan}=50,
2 – $x/c = 0.5(1-\cos\theta)$ — 2.2 – N_{pan}=100
3 – $x/c = 1-\cos\theta$ — 3.2 – N_{pan}=100

Figure 4. a) Generation of grid points x/c along airfoil by mapping semi (quarter) circle, b) stretching of the grid panels Δs(i)/Δs(i-1) along NACA 0012 airfoil, x/c – location of grid points along airfoil chord, Δs(i) – panel length, N_{pan}-number of 'panels', i.e. wall volumes along airfoil

of original points on a circle (N_{pan}=100), however without improving distribution near tail, line 2.2 in Figure 4b . Algebraic mapping of the quarter circle remedies accumulation of grid points near trailing edge, lines 3 and 3.2 in Figure 4ab. Finer grid in multigrid procedure is generated by 'halving' the previous, coarse, grid. This results in N_{pan}=1024 panels along the airfoil for the finest grid (finesse index kg=6) and Nc=Nw=320 panels along the wake cut (G-H) and wake outlet section (A-H) respectively. The total number of control volumes on the finest grid without local refinement amounts to 0.5 10^6.

The effects of grid local refinement on flow prediction are tested on coarser grid (kg=5) where only near wall control volumes are refined. Calculation of the laminar flow converged to the values obtained on the finest grid (kg=6) with considerable computational time saving. Testing of the locally refined grid for the calculation of turbulent flow, unfortunately, showed instability. Results in Section 3 are obtained on the finest grid (kg=6) with 1664*320 control volumes.

Various boundary conditions along open side boundaries (A-B, C-D, in Figure 3): inlet, outlet and symmetrical, are tested by calculating flow at incidence angle $\alpha = 0^0$. Outlet boundary conditions correspond best to reality; values of the flow variables are not prescribed on the outlet boundary, but extrapolated from the neighboring interior points located upstream to the boundary. Inlet boundary conditions $\bar{u} = \mathrm{v}_0$, $\bar{v} = 0$, $\bar{k} = \bar{k}_0$, $\bar{\varepsilon} = \bar{\varepsilon}_0$ 'overdetermine' flow development, particularly with reference to the neglected velocity components normal to the boundary. Testing of various boundary conditions proves that they have negligible effect on calculated pressure and shear stress distribution along airfoil and lift/drag coefficients as well. Calculation of the flow at incidence angle $\alpha = 3^0$ with inlet boundary conditions along B-C-D ($\bar{u} = v_0 \cos\alpha$, $\bar{v} = v_0 \sin\alpha$, $\bar{k} = \bar{k}_0$, $\bar{\varepsilon} = \bar{\varepsilon}_0$) and outlet boundary conditions along A-B diverged. All calculations further on are performed with the prescribed inlet boundary conditions along A-B and C-D boundaries.

3. **Prediction of airfoil flow**

Potentials of the original program in predicting separation are tested by calculating airfoil flow around NACA 0012 at $Re = 10^4$ and $\alpha = 0^0$, when the airfoil boundary layer is entirely laminar. Calculated distribution [11] of the pressure coefficient (not presented in the paper) $c_p = 2(p-p_0)/\rho v_0^2$ near the leading edge $x/c \leqslant 0.3$ agrees well with the results of calculation by Rhie-Mehta [8] (no experimental data are available). Position of the separation point $x_s/c \approx 0.85$ is the same as in [8]; however, downstream recovery of the velocity-pressure in the trailing region is faster.

Pressure distribution at $\alpha = 0^0$ and Re=2.88 10^6, shown in Figure 5a, is calculated by assuming fully turbulent flow (ignoring laminar flow in the development of the airfoil boundary layer) and agrees well with the experimental data of Gregory [2]. Better prediction with comparison with the Rhie calculation [8] can be partly explained by the finer grid. The deficiency of the model, which ignores the laminar character of the flow in the boundary layer (occupying 40% of the airfoil chord length) has little impact on the correct flow prediction. Capturing of viscous effects negligibly affects calculation of the pressure distribution at a small incidence angle. Grid finesse contributes to better prediction only near the leading edge, i.e. of the peak pressure.

Correct prediction of pressure distribution reflects upon airfoil lift characteristic, lines 5 and 6 in Figure 6, which coincide with the experimental results at small

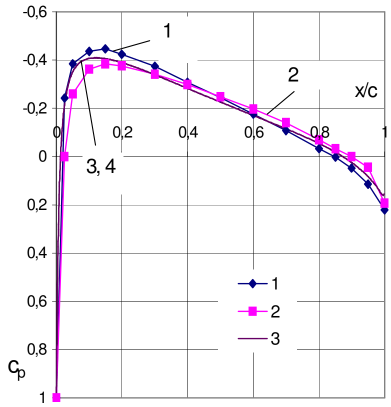

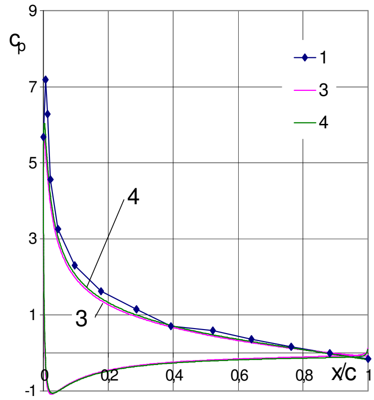

1 – exp. Gregory [2]   3 – calc. k-ε model+wall functions, 1664*320 control volumes, fully turbulent flow [11]

2 – calc. Rhie [8]   4 – same as 3) except prescribed transition from laminar to turbulent [11]

Figure 5. Pressure distribution along NACA 0012: a) α=0^0, b) α=12^0, Re=2.8 10^6

incidence angles. This is expected because lift coefficient c_L, being calculated by means of normal c_y and tangential c_x force coefficients:

$$c_L = c_y \cos\alpha - c_x \sin\alpha \tag{3.1}$$

is dominated by $c_y = c_{py} + c_{\tau y}$, i.e. the integral contribution of pressure along the airfoil contour:

$$c_{py} = \oint_{s_a} c_p \, \mathrm{d}(x/c) \; .$$

Excessive values of drag coefficient c_D at small incidence angles, lines 5 and 6 in Figure 7, in comparison with the experimental ones, indicate inadequate modelling of the flow as fully turbulent. Large values of c_D:

$$c_D = c_y \sin\alpha + c_x \cos\alpha \tag{3.2}$$

for small incidence angles α can be attributed to the large values of wall shear stress τ_w, i.e. skin friction coefficient $c_f(= 2\tau_w/\rho v_0^2)$, and its integral contribution

$$c_{\tau_x} = \oint_{s_a} c_{fx} \, \mathrm{d}(s/c)$$

to the tangential force coefficient $c_x = c_{px} + c_{\tau x}$.

The computer program is modified by suppressing turbulence, i.e. turbulent stress in the laminar region. Location of transition on the upper-lower part of airfoil x_{tr}/c is prescribed on the basis of experimental data [2]. Zero value of turbulent viscosity $\mu_t = 0$ and very small value of turbulence kinetic energy $\bar{k}$ are imposed on all nodes in the laminar region in every step of the global iteration procedure.

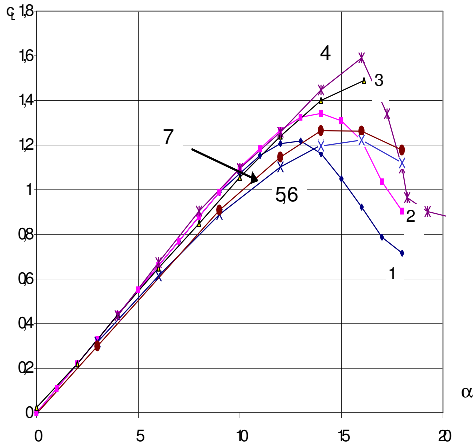

Experiments:
1,2 – $Re = 2.0 - 5.0 \cdot 10^6$ [4]
3 – $Re = 2.88 \cdot 10^6$ Gregory [2]
4 – Abbot [3] calculated at $Re = 2.88 \cdot 10^6$
5 – standard k-ε model with wall functions, grid finesse kg=5, 832x160 control volumes
6 – k-ε, grid finesse kg=6, 1664*320 c.v.
7 – same as 6) except prescribed laminar-turbulent transition [11]

Figure 6. Lift coefficients of NACA 0012 airfoil

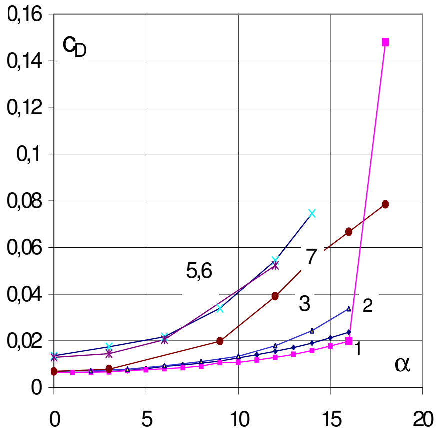

Figure 7. Drag coefficient of NACA 0012 airfoil (for legend see Figure 6.)

Small value of $\bar{k}$ is prescribed in order to avoid divergence of the numerical procedure that is noticed for initially prescribed zero values of $\bar{k}$.

Favorable effect of prescribing laminar-turbulent transition is evident in Figures 6 and 7, line 7.

Underprediction of the lift coefficient is reduced. Maximum of the lift is more distinguished and analysis of the flow pattern indicates presence of separation near the trailing edge at $\alpha \leqslant 18^0$, Figure 8. Drag coefficient perfectly matches experimental values for smaller incidence angles. Significant reduction of drag is due to smaller skin friction in the laminar part of the boundary layer that extends along almost the entire lower part of the airfoil.

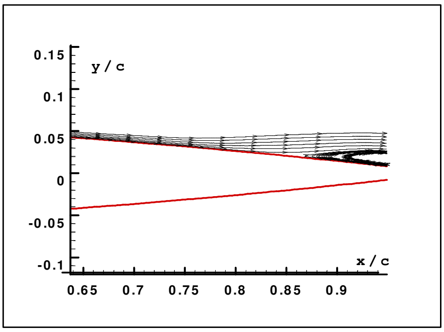

Figure 8. Flow pattern near NACA 0012 trailing edge at Re=2.88 10^6, α=18^0 [11]

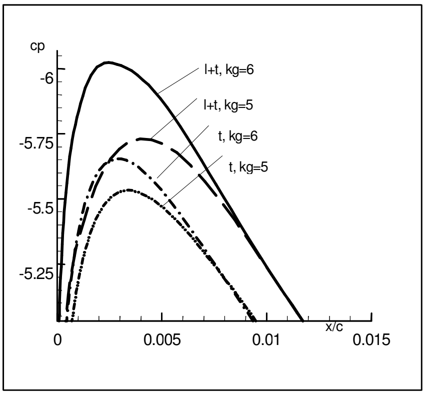

Figure 9. Pressure coefficient c_p along NACA 0012 airfoil leading edge (suction side) at Re=2.88 10^6, α=12^0 [11]: t- calc. assuming fully turbulent flow, l+t- calc. with prescribed transition laminar-turbulent, kg-grid finesse index

Increase of the lift occurs mainly due to higher (under) pressure along the airfoil suction side. Figure 9 shows that increase in the peak pressure is quite discernible ($\Delta c_p \approx 0.5$ for $\alpha = 12^0$) and calculated values no longer fall short of the experimental ones as much as before.

4. **Conclusions**

Numerical prediction of the airfoil aerodynamic characteristics is improved by introducing prescribed transition from laminar to turbulent. Stall is predicted and accompanied by a trailing edge separation bubble at the incidence angle slightly higher than the experimental one. Underprediction of pressure near the leading edge is responsible for disagreement between the calculated and experimental values of the lift/drag coefficients at higher incidence angles.

References

1. Mehta, U., Chang, K. C. and Cebeci, T.: *A Comparison of Interactive Boundary Layer and Thin Layer Navier Stokes Procedures.* Numerical and Physical Aspects of Aerodynamic Flows III. Springer-Verlag, New York, 1985, 198-215.
2. Gregory, N. and O'Riley, C.L.: Low speed aerodynamic characteristics of NACA aerofoil section including the effect of upper surface roughness, NPL AERO Report 1308, 1970.
3. Abbot, I. H. and Doenhoff, A. E.: *Theory of Wing Sections.* Dover Publications, 1958.
4. Lazauskas, L.: "www.maths.adelaide.edu.au/llazauskas", 1997.
5. Angel, R. K., Musgrove, P. J., Galbraith, R. A. and Green, R. B.: *Summary of the Collected Data for Tests on the NACA 00 Aerofoils.* University of Glasgow, ETSU WN 5072-P2, 1990.
6. Ferziger, J. F. and Perić, M.: *Computational Methods for Fluid Dynamics.* Springer-Verlag, 1997.
7. Perić, M.: *A Finite-Volume for the Prediction of Three-Dimensional Fluid Flow in Complex Ducts*. PhD Thesis, University of London, Imperial College, London, 1985.
8. Rhie, C. M. and Chow, W. L.: A numerical study of the turbulent flow past an isolated airfoil with trailing edge separation. AIAA-82-0998, AIAA/ASME 3^{rd} *Joint Thermophysics, Fluids, Plasma and Heat Transfer Conference*, St. Louis, Missouri, 1982.
9. Spalart, P. R.: Direct simulation of a turbulent boundary layer up to Re_θ=1410. *Journal of Fluid Mechanics*, **187**, (1988), 61-98.
10. Rodi, W. and Scheurer, G.: Scrutinizing the k-ε Turbulence Model Under Adverse Pressure Gradient Conditions. *Journal of Fluid Engineering*, **108**, (1986), 174-179.
11. Milas, Z.: *Analysis of Turbulent Flow Around Airfoil.* Faculty of Mechanical Engineering and Naval Architecture, PhD Thesis, University of Zagreb, Zagreb, 2001, p. 209.
12. Mansour, N. N., Kim, J. and Moin, P.: Near-wall k-ε turbulence modeling. *AIAA Journal*, 27(8), (1989), 1068-1073.
13. So, R .M. C., Lai, Y. G., Zhang, H. S. and Hwang, B. C.: Second order near wall turbulence closures: A review. *AIAA Journal*, **29**(11), (1991) 1819-1835.
14. Derksen, R. W. and Azad, R. S.: Behaviour of the turbulent energy equation at a fixed boundary. *AIAA Journal*, **19**(2), (1981), 238-239.
15. Fernholz, H. H. and Finley, P. J.: The incompressible zero-pressure gradient turbulent boundary layer: An assessment of the data. *Progress in Aerospace Engineering*, **32**(4), (1996), 245-312.
16. Eppler, R.: *Airfoil Design and Data.* Springer-Verlag, Berlin, 1990.

Journal of Computational and Applied Mechanics, Vol. 6., No. 1., (2005), pp. 107–113

APPLICATION OF THE GENERALIZED FDM FOR NUMERICAL SOLUTION OF NON-LINEAR THERMAL DIFFUSION PROBLEMS

Bohdan Mochnacki and Edyta Pawlak
Institute of Mathematics and Computer Science
Technological University of Częstochowa
42-200 Częstochowa, Dąbrowskiego 68, Poland
moch@imi.pcz.pl

[Received: January 15, 2004]

Abstract. A generalized variant of the finite difference method [2, 3, 4] is used for numerical modelling of non-steady and non-linear thermal diffusion problems. In order to simplify the considerations the 1D problem (infinite plate) is discussed, but the way of 2D algorithm construction is very similar. In the first part of the paper the governing equations are presented, in the second one, some details connected with the numerical algorithm and an example of computations can be found.

Mathematical Subject Classification: 80M20
Keywords: generalized finite difference method, non-linear thermal diffusion

1. **Introduction**

The $1D$ heat diffusion that takes place in the domain of a plate is described by the equation

$$0 < x < L \qquad c(T)\frac{\partial T(x,t)}{\partial t} = \frac{\partial}{\partial x}\left[\lambda(T)\frac{\partial T}{\partial x}\right] + q_v(x,t) \ , \tag{1.1}$$

where $c(T)$ is volumetric specific heat, λ is thermal conductivity, $q_v(x,t)$ is the capacity of internal heat sources, L is thickness of the plate, T, x, t denote temperature, spatial co-ordinate and time.

For $x = 0$ and $x = L$ the boundary conditions are given in the form

$$\begin{aligned} x = 0: \qquad & \Phi_1\left[T(x,t), \frac{\partial T(x,t)}{\partial n}\right] = 0 \ , \\ x = L: \qquad & \Phi_2\left[T(x,t), \frac{\partial T(x,t)}{\partial n}\right] = 0 \ , \end{aligned} \tag{1.2}$$

where $\frac{\partial T(x,t)}{\partial n}$ is the derivative with respect to the outward normal.

The initial condition

$$T(x,\ 0) = T_0 \tag{1.3}$$

is also known. For our further considerations equation (1.1) is written in the following form

$$0 < x < L \quad c(T)\frac{\partial T(x,\ t)}{\partial t} = \frac{\mathrm{d}\,\lambda(T)}{\mathrm{d}\,T}\left[\frac{\partial T(x,\ t)}{\partial x}\right]^2 + \lambda(T)\frac{\partial^2 T}{\partial x^2} + q_v(x,\ t)\ . \tag{1.4}$$

2. A numerical model

The domain $[0, L]$ is covered by a 1D geometrical mesh. The step h_j can be optional and variable. The points forming the geometrical mesh Δ_k can be arbitrary. Now we define the sets of the nodes, which form the successive stars. The star is created by the central node and a certain number of nodes from its neighborhood. In this place two approaches can be taken into account. The star is generated using the criterion concerning the number of points e.g. 5-point star - as in Figure 1, or on the basis of the condition that determines the distance between the central node x_i and adjacent

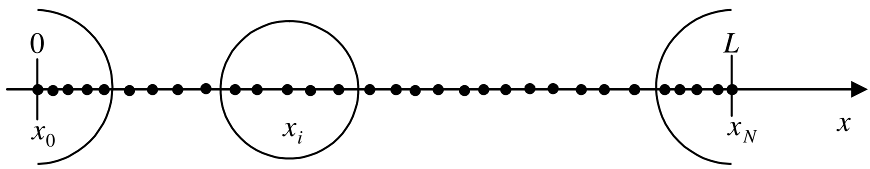

Figure 1. Nodes and stars

nodes x_j. The position of the central node determines the type of the star. If the point x_i belongs to the interior of the domain Ω, then an internal star is considered and the FDM equation resulting from (1.4) is constructed. If the point x_i is a boundary one (for 1D problems x_i corresponds to x_1 or x_N), then we consider the boundary star for which the FDM equation results from the boundary condition given at point x_i. For the sake of further mathematical manipulations, we introduce the local numeration of nodes forming the arms of the star: $j = 1, 2, \ldots, n$. For non-steady problems the time grid Δ_t must also be introduced:

$$0 = t^0 < t^1 < t^2 < \ \ldots\ < t^f < t^{f+1} < \ \ldots\ < t^F < \infty\ ,\ \Delta t = t^{f+1} - t^f \tag{2.1}$$

The Cartesian product $\Delta_h \otimes \Delta_t$ creates a spatial-time grid. In order to find an approximation for the first and second derivatives of the function T at the point x_i (they are involved in equation (1.4) and conditions (1.2)), we expand the function $T\left(x,\ t^f\right)$ (explicit scheme [1]) into Taylor's series with an accuracy to the terms containing derivatives of the second order

$$T\ \left(x,\ t^f\right) \cong T\ \left(x_i,\ t^f\right) + \left(\frac{\partial T}{\partial x}\right)_i^f (x - x_i) + \left(\frac{\partial^2 T}{\partial x^2}\right)_i^f \frac{(x - x_i)^2}{2\,!}\ . \tag{2.2}$$

In particular, for $x = x_i$ we have

$$T_j^f \cong T_i^f + (T_x)_i^f \, h_j + 0.5 \, (T_{xx})_i^f \, h_j^2 \,, \tag{2.3}$$

where $h_j = x_j - x_i$, while the partial derivatives of the function T at the central point x_i for the point of time t^f are denoted by $(T_x)_i^f$ and $(T_{xx})_i^f$. The following quality criterion can be set up [2, 3, 4]:

$$J = \sum_{j=1}^{n} \left\{ \left[T_i^f - T_j^f + (T_x)_i^f \, h_j + 0.5 \, (T_{xx})_i^f \, h_j^2 \right] \frac{1}{\rho_j^m} \right\}^2 = \min \,, \tag{2.4}$$

where $\rho_j = |x_j - x_i| = |h_j|$, m is a natural number, n is the number of nodes creating the star considered, $1/\rho_j^m$ are the tapering functions introduced in order to take into account the influence of the node x_j distance to the star center x_i, and its 'participation' in the approximation of derivatives.

The minimum condition for the functional J is to make the derivatives $\frac{\partial J}{\partial (T_x)_i^f}$ and $\frac{\partial J}{\partial (T_{xx})_i^f}$ equal to zero. Consequently,

$$\left\{ \begin{array}{l} \dfrac{\partial J}{\partial (T_x)_i^f} = 0 \,, \\ \dfrac{\partial J}{\partial (T_{xx})_i^f} = 0 \,. \end{array} \right. \tag{2.5}$$

These conditions lead to the system of equations

$$\left\{ \begin{array}{l} \sum\limits_{j=1}^{n} \left[T_i^f - T_j^f + (T_x)_i^f \, h_j + 0.5 \, (T_{xx})_i^f \, h_j^2 \right] \frac{h_j}{\rho_j^{2m}} = 0 \,, \\ \sum\limits_{j=1}^{n} \left[T_i^f - T_j^f + (T_x)_i^f \, h_j + 0.5 \, (T_{xx})_i^f \, h_j^2 \right] \frac{h_j^2}{2\rho_j^{2m}} = 0 \,. \end{array} \right. \tag{2.6}$$

Equations (2.6) can be rewritten in a matrix form

$$\begin{bmatrix} \sum\limits_{j=1}^{n} \frac{h_j^2}{\rho_j^{2m}} & \sum\limits_{j=1}^{n} \frac{h_j^3}{2\rho_j^{2m}} \\ \sum\limits_{j=1}^{n} \frac{h_j^3}{2\rho_j^{2m}} & \sum\limits_{j=1}^{n} \frac{h_j^4}{4\rho_j^{2m}} \end{bmatrix} \begin{bmatrix} (T_x)_i^f \\ (T_{xx})_i^f \end{bmatrix} = \begin{bmatrix} \sum\limits_{j=1}^{n} \frac{h_j}{\rho_j^{2m}} \left(T_j^f - T_i^f \right) \\ \sum\limits_{j=1}^{n} \frac{h_j^2}{2\rho_j^{2m}} \left(T_j^f - T_i^f \right) \end{bmatrix} , \tag{2.7}$$

from where

$$\begin{bmatrix} (T_x)_i^f \\ (T_{xx})_i^f \end{bmatrix} = \begin{bmatrix} \sum\limits_{j=1}^{n} \frac{h_j^2}{\rho_j^{2m}} & \sum\limits_{j=1}^{n} \frac{h_j^3}{2\rho_j^{2m}} \\ \sum\limits_{j=1}^{n} \frac{h_j^3}{2\rho_j^{2m}} & \sum\limits_{j=1}^{n} \frac{h_j^4}{4\rho_j^{2m}} \end{bmatrix}^{-1} \begin{bmatrix} \sum\limits_{j=1}^{n} \frac{h_j}{\rho_j^{2m}} \left(T_j^f - T_i^f \right) \\ \sum\limits_{j=1}^{n} \frac{h_j^2}{2\rho_j^{2m}} \left(T_j^f - T_i^f \right) \end{bmatrix} . \tag{2.8}$$

If the elements of the inverse matrix in equation (2.8) are denoted by g_{ij} we have

$$\begin{bmatrix} (T_x)_i^f \\ (T_{xx})_i^f \end{bmatrix} = \begin{bmatrix} g_{11} & g_{12} \\ g_{21} & g_{22} \end{bmatrix} \begin{bmatrix} \sum\limits_{j=1}^{n} \frac{h_j}{\rho_j^{2m}} \left(T_j^f - T_i^f \right) \\ \sum\limits_{j=1}^{n} \frac{h_j^2}{2\rho_j^{2m}} \left(T_j^f - T_i^f \right) \end{bmatrix} . \tag{2.9}$$

The system of equations (2.9) allows us to find the optimal local approximations for the first and second derivatives at the point x_i and for the time t^f. Therefore

$$(T_x)_i^f = \sum_{j=1}^{n} \hat{z}_j T_j^f - T_i^f \sum_{j=1}^{n} \hat{z}_j \ , \tag{2.10}$$

where

$$\hat{z}_j = \frac{1}{\rho_j^{2m}} \left[g_{11} h_j + \frac{1}{2} g_{12} h_j^2 \right] \tag{2.11}$$

and

$$(T_{xx})_i^f = \sum_{j=1}^{n} z_j T_j^f - T_i^f \sum_{j=1}^{n} z_j \ , \tag{2.12}$$

in which

$$z_j = \frac{1}{\rho_j^{2m}} \left[g_{21} h_j + \frac{1}{2} g_{22} h_j^2 \right] \ . \tag{2.13}$$

To determine the time derivative for $t \in [t^f, t^{f+1}]$ we shall use the simple differential quotient

$$\frac{\partial T(x_i,t)}{\partial t} \cong \frac{T\left(x_i, t^{f+1}\right) - T\left(x_i, t^f\right)}{\Delta t} = \frac{T_i^{f+1} - T_i^f}{\Delta t} \ . \tag{2.14}$$

The local approximation of equation (1.4) for internal node x_i is the following

$$c\left(T_i^f\right) \frac{T_i^{f+1} - T_i^f}{\Delta t} = \left(\frac{\mathrm{d}\lambda}{\mathrm{d}T}\right)_i^f \left[(T_x)_i^f\right]^2 + \lambda\left(T_i^f\right) (T_{xx})_i^f + (q_v)_i^f \tag{2.15}$$

from which the temperature T_i^{f+1} can be found.

Substituting equations (2.10) and (2.12) into equation (2.15) we have

$$c\left(T_i^f\right) \frac{T_i^{f+1} - T_i^f}{\Delta t} = \left(\frac{\mathrm{d}\lambda}{\mathrm{d}T}\right)_i^f \left[\sum_{j=1}^{n} \hat{z}_j T_j^f - T_i^f \sum_{j=1}^{n} \hat{z}_j\right]^2 + \\ + \lambda\left(T_i^f\right) \left[\sum_{j=1}^{n} z_j T_j^f - T_i^f \sum_{j=1}^{n} z_j\right] + (q_v)_i^f \tag{2.16}$$

and

$$T_i^{f+1} = T_i^f + \frac{\Delta t}{c\left(T_i^f\right)} \left(\frac{\mathrm{d}\,\lambda}{\mathrm{d}\,T}\right)_i^f \left[\sum_{j=1}^{n} \hat{z}_j T_j^f - T_i^f \sum_{j=1}^{n} \hat{z}_j\right]^2 + \\ + \frac{\lambda\left(T_i^f\right)\Delta t}{c\left(T_i^f\right)} \left[\sum_{j=1}^{n} z_j T_j^f - T_i^f \sum_{j=1}^{n} z_j\right] + \frac{\Delta t}{c\left(T_i^f\right)} (q_v)_i^f \ . \tag{2.17}$$

This formula can be written in the form

$$T_i^{f+1} = \frac{\lambda\left(T_i^f\right)\Delta t}{c\left(T_i^f\right)}\sum_{j=1}^{n} z_j T_j^f + T_i^f\left(1 - \frac{\lambda\left(T_i^f\right)\Delta t}{c\left(T_i^f\right)}\sum_{j=1}^{n} z_j\right) + \frac{\Delta t\, Q_i^f}{c\left(T_i^f\right)}\,, \tag{2.18}$$

where

$$Q_i^f = \left(\frac{\mathrm{d}\lambda}{\mathrm{d}T}\right)_i^f \left[\sum_{j=1}^{n} \hat{z}_j T_j^f - T_i^f \sum_{j=1}^{n} \hat{z}_j\right]^2 + (q_v)_i^f\ . \tag{2.19}$$

The stability condition of the scheme discussed is the following

$$1 - \frac{\lambda\left(T_i^f\right)\Delta t}{c\left(T_i^f\right)}\sum_{j=1}^{n} z_j \geqslant 0\ . \tag{2.20}$$

The equations for $x = 0$ and $x = L$ result directly from the approximation of the boundary conditions.

3. Example of computations

We consider a plate (5 cm) for which the thermal conductivity is assumed to be a linear function: $\lambda = aT + b$, where $a = -0.04023$, $b = 60.916$, while the specific heat is approximated by the function: $c = AT^2 + BT + C$, where $A = 1.6187$, $B = 290.9286$. $C = 3692954.4$. For $x = 0$ the no-flux condition is assumed, for $x = L$ the Robin condition is taken into account.

The plate is cooled in the conditions of natural convection and radiation. The heat transfer coefficient is the sum of convective component $\alpha_k = 10\mathrm{W/m^2K}$ and the radiant one given by the formula

$$\alpha_r = 10^{-4}\varepsilon\, C_C \left[\left(\frac{T}{100}\right)^2 + \left(\frac{T_a}{100}\right)^2\right](T + T_a) \tag{3.1}$$

where $\varepsilon = 0.8$ is thermal emissivity, $C_C = 5.67\mathrm{W/m^2K^4}$, T_a is the ambient temperature. The initial temperature equals 900 ^{0}C, $T_a = 30^0$C (303 K).

The problem was solved in several variants. In Figures 2 to 3 the temperature profiles in the domain considered are shown.

The first solution has been obtained for the regular mesh, 3-point stars and an exponent $m = 0$. The domain is covered by the set of 51 nodes in which x_0 and x_{50} are the boundary nodes. The results are shown in Figure 2.

In the same Figure the numerical solution is compared with the results obtained using the control volume method (symbols marked in Figure 2) and the differences between these solutions are less than 3K.

In Figure 3 the temporary temperature field for the points of time 2, 4, 6, 8 and 10 minutes (the same times as in Figure 2) are presented. This simulation is carried

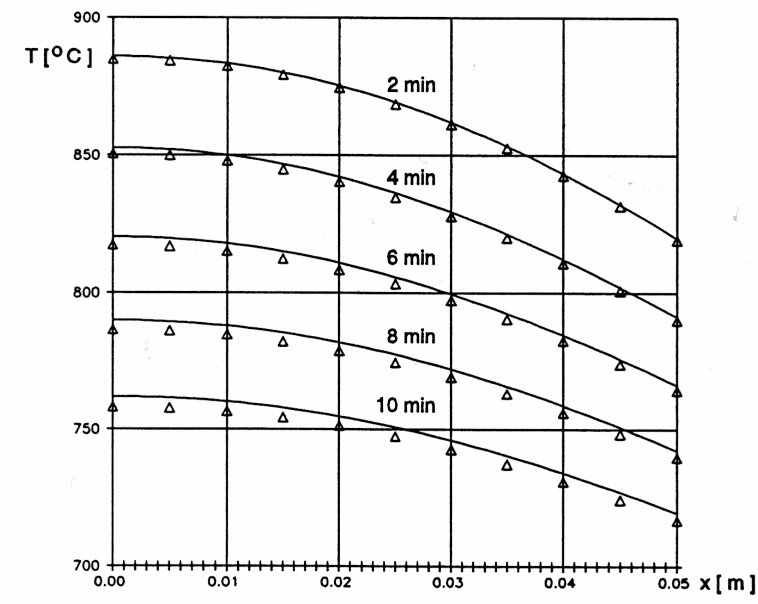

Figure 2. Solution for regular mesh

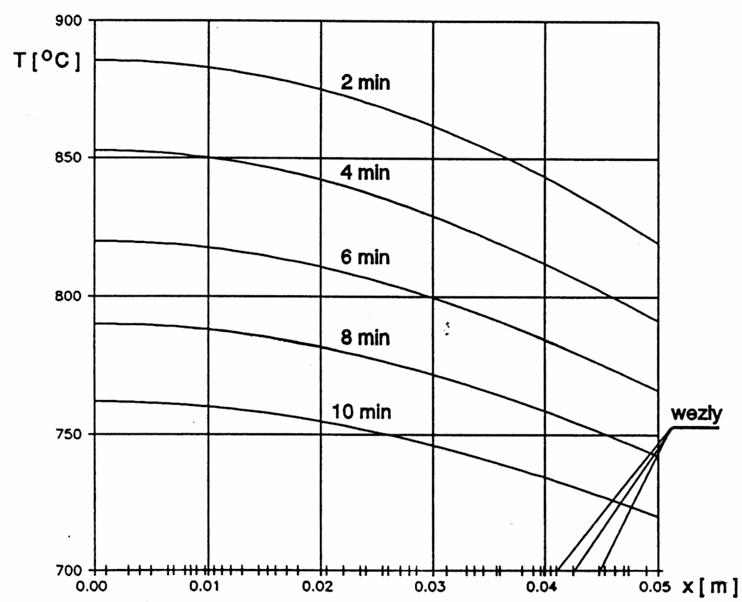

Figure 3. Solution for 'chaotic' mesh

out for the 'chaotic' mesh (see points along x axis), 5-point stars and exponent $m = 1$. The results shown in the Figures discussed are practically the same.

The generalized FDM can be also efficiently used in the case of 2D problems and the details of the algorithm can be found among others in [4, 5, 6, 7]. The GFDM was tested for different thermal diffusion problems and we did not find limitations to the method applications.

4. **Final remarks**

The generalized variant of the finite difference method constitutes a very effective tool for numerical solution of the large class of thermal diffusion problems. The very essential disadvantage of the FDM consists in the limitations resulting from the necessity of regular meshes construction. It causes, as a rule, that the real shape of the domain is approximated inexactly. In the case of GFDM this inconvenience does not appear. The theoretical and numerical aspects of FDM for the steady state problems are sufficiently described in literature. In this paper we discuss the problems connected with the method application in the case of transient heat diffusion, at the same time both the governing equation and the boundary conditions are non-linear. The GFDM algorithm is more complex than the FDM one, but is not an essential obstruction for its practical applications.

Note. The paper was presented at the 9th International Conference on Numerical methods in Continuum Mechanics, Zilina, Slovakia, 9-12 September 2003 and its shorter version was published in the Conference CD Proceedings.

References

1. Godunow, S. K. and Riabenkij, W. S.: *Differential schemes. An Introduction to the Theory*, Nauka, Moskwa, 1997. (in Russian)
2. Orkisz, J.: *Computational Mechanics, New Trends and Applications.* Idelshon S., Onate E., Dvorkin E. (eds.), Buenos Aires, 1998.
3. Krok, J. and Orkisz, J.: A unfield to the FE generalized variational FD method in nonlinear mechanics, *Proceedings of the Discretization methods in structural mechanics, IUTAM/IACM Symp.*, Vienna, 1989, pp. 353-362.
4. Pawlak, E.: *Application of the Generalized Finite Difference Method for Numerical Modelling of Linear and Non-linear Thermal Diffusion Problems.* Ph. D. Thesis., Techn. Univ. of Częstochowa, Częstochowa, 1999. (in Polish)
5. Mochnacki, B. and Pawlak, E.: Numerical modelling of non-steady thermal diffusion on the basis of generalized FDM. *Heat Transfer'98*, Computational Mechanics Publications, (1998), 33-42.
6. Mochnacki, B., Pawlak, E. and Lara, S.: Numerical solution of 2D Stefan problem. *Solidification of Metals and Alloys*, **2**(44), (2000), 235-238.
7. Mochnacki, B., Pawlak, E. and Lara, S.: Application of generalized finite difference method in numerical modelling of bioheat transfer processes. *Acta of Bioengineering and Biomechanics*, **4**(1), (2002), 478-479.

Journal of Computational and Applied Mechanics, Vol. 6., No. 1., (2005), pp. 115–128

ON TRANSVERSE VIBRATIONS OF BELTS

Gyula Patkó, Tibor Kollányi
Department of Machine Tools, University of Miskolc
3515 Miskolc - Egyetemváros, Hungary
kollanyi@szgtirix.szgt.uni-miskolc.hu

[Received: September 2, 2004]

Abstract. The paper examines the transverse vibrations of belts and the impact of the vibration modes on unstable speed ranges. Supposing large deformations, it produces a more general non-linear motion of equation for the vibrations, which may be suitable for the examination of further linear and non-linear vibrations. It is shown that in the course of the belt motion, parametrically excited non-linear vibrations develop. The parametrical excitation is caused by the change in length of the belts resulting from the eccentricity of one of the belt pulleys. Next the paper examines the impact of vibration modes developing during the transverse vibrations of the belts on the main instability range. A first approximation of a closed form is developed for the main instability ranges of transverse vibrations. It is shown that the instability ranges belonging to the higher vibration modes become wider and tend to move towards higher numbers of revolutions.

Mathematical Subject Classification: 73A05
Keywords: belt drive, transverse vibration, non-linear dynamics, stability analysis

1. **Introduction**

Belt drives are extensively used in mechanical engineering practice for the transmission of moments and power between axles located far away from each other. Its widespread application – in the automobile industry, a number of branches of the light industry, general engineering and machine tool industry, etc. – can be explained by its inexpensive realisation, quiet operation, easy mounting, favourable vibration damping, and last but not least by its good efficiency. The theory of belt drive design has been known and applied in engineering practice for a long time. Today renowned belt manufacturers support graphical dimensioning of belts based on diagrams. The basis of these selection and dimensioning procedures is provided by strength calculations.

In applications requiring higher accuracy – for example the main and feed drives of machine tools – it is not sufficient to dimension the particular machine elements, in particular belts, exclusively in terms of strength. In such cases it is also essential to apply a knowledge of vibrations that will facilitate the solution or elimination of dynamic problems in the design phase. When designing belt drives, basically two kinds of dynamic tasks are to be solved. One of them is an examination of the problems arising from the longitudinal vibrations of the belts. The other is an examination of the transverse vibrations of the belts. It is known both from the literature and from practical experience that at a certain running speed the belts lose their stability and develop transverse vibrations. These vibrations exert a detrimental influence on the life of the belt and in some cases on that of the machine, and – in the case of machine tools – may exert a non-desirable effect on the machining process and the manufacturing accuracy. Therefore it is expedient and important to determine in the design phase the instability ranges where the non-desirable vibrations mentioned above may develop. The following is a stability analysis of transverse vibrations.

2. The system of equations of motion of a single belt

2.1. **The mechanical model.** On the basis of the understanding of the literature it is expedient in the analysis of certain types of vibrations arising in the application of belt drives to consider the non-linear material properties of the belt (cf. e.g. [3]). One possible way to do so is to approximate the characteristic curve of the belt with a third degree polynomial. Accordingly, the material law applying to the belt is supposed to have the following form

$$\sigma_x = E\varepsilon_x + \beta\varepsilon_x^3, \tag{2.1}$$

where σ_x is the tensile stress arising in the belt, ε_x is the strain in direction x, E and β are material constants, which have to be determined by means of measurements. In the derivation of the equations of motion the following are supposed to hold:

- the belt moves only in plane xz according to Figure 1,
- only the force stretching the belt acts on the belt,
- the cross-sectional area of the belt is constant, its material properties do not change along the axis x,
- in the beginning the internal damping of the belt is neglected,
- the effects of the belt separating from and being stretched on the discs are neglected in accordance with [4].

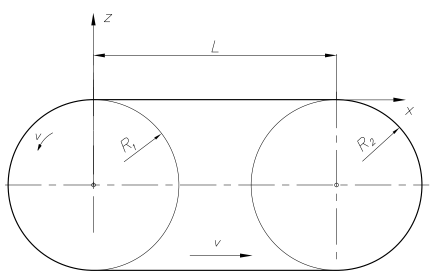

Figure 1. Mechanical model of the drive

As usual, the line connecting the centres of gravity of the cross-sectional areas is called the centre line of the belt. The displacement of the point with abscissa x of the belt centre line in direction x is denoted by $u\,(x,t)$, and that in direction z is denoted by $w\,(x,t)$. In accordance with our supposition, the displacement in direction y is zero, therefore the strain of the center line according to [1, 3] is approximated by

$$\varepsilon_{x0} = \frac{\partial u}{\partial x} + \frac{1}{2}\left[\left(\frac{\partial u}{\partial x}\right)^2 + \left(\frac{\partial w}{\partial x}\right)^2\right]. \tag{2.2}$$

On the basis of experience $\left(\frac{\partial u}{\partial x}\right)^2$ in (2.2) may be negligible as related to the very small $\frac{\partial u}{\partial x}$, but $\frac{\partial w}{\partial x}$ may be large as compared with $\frac{\partial u}{\partial x}$. Therefore on the basis of [1] the approximation

$$\varepsilon_{x0} = \frac{\partial u}{\partial x} + \frac{1}{2}\left(\frac{\partial w}{\partial x}\right)^2 \tag{2.3}$$

is used. If the curvature of the center line is approximated by $\frac{\partial^2 w}{\partial x^2}$, then the axial strain of an arbitrary fibre in the belt can be written in the form

$$\varepsilon_{x} = \frac{\partial u}{\partial x} + \frac{1}{2}\left(\frac{\partial w}{\partial x}\right)^2 - z\frac{\partial^2 w}{\partial x^2}\,. \tag{2.4}$$

2.2. **Equations of motion.** The equations of motion are derived by means of the Hamilton principle. Therefore the following can be written

$$\delta \int_{t=t_1}^{t_2} (W - T)\,\mathrm{d}t = 0\,.$$

After the calculations detailed in Appendix A the following equations of motion are obtained:

$$\begin{aligned}
&\varrho A\tfrac{\partial^2 u}{\partial t^2} - \tfrac{\partial}{\partial x}\Bigg\{AE\left[\tfrac{\partial u}{\partial x} + \tfrac12\left(\tfrac{\partial w}{\partial x}\right)^2\right] + \beta\Bigg\{A\left[\tfrac{\partial u}{\partial x} + \tfrac12\left(\tfrac{\partial w}{\partial x}\right)^2\right]^3 + \\
&+3I_y\left[\tfrac{\partial u}{\partial x} + \tfrac12\left(\tfrac{\partial w}{\partial x}\right)^2\right]\cdot\left(\tfrac{\partial^2 w}{\partial x^2}\right)^2 - 2I_{3y}\left[\tfrac{\partial u}{\partial x} + \tfrac12\left(\tfrac{\partial w}{\partial x}\right)^2\right]\cdot\left(\tfrac{\partial^2 w}{\partial x^2}\right)^3\Bigg\}\Bigg\} = 0
\end{aligned} \tag{2.5}$$

$$\begin{aligned}
&\varrho A\tfrac{\partial^2 w}{\partial t^2} - \tfrac{\partial}{\partial x}\Bigg\{\tfrac{\partial w}{\partial x}\Bigg\{AE\left[\tfrac{\partial u}{\partial x} + \tfrac12\left(\tfrac{\partial w}{\partial x}\right)^2\right] + \beta\Bigg\{A\left[\tfrac{\partial u}{\partial x} + \tfrac12\left(\tfrac{\partial w}{\partial x}\right)^2\right]^3 + \\
&+3I_y\left[\tfrac{\partial u}{\partial x} + \tfrac12\left(\tfrac{\partial w}{\partial x}\right)^2\right]\cdot\left(\tfrac{\partial^2 w}{\partial x}\right)^2 - 2I_{3y}\left[\tfrac{\partial u}{\partial x} + \tfrac12\left(\tfrac{\partial w}{\partial x}\right)^2\right]\cdot\left(\tfrac{\partial^2 w}{\partial x^2}\right)^3\Bigg\}\Bigg\}\Bigg\} + \\
&\quad+\tfrac{\partial}{\partial x^2}\Bigg\{\tfrac{\partial^2 w}{\partial x^2}\Bigg\{I_y E + \beta\Bigg\{3I_y\left[\tfrac{\partial u}{\partial x} + \tfrac12\left(\tfrac{\partial w}{\partial x}\right)^2\right]^2\cdot\left(\tfrac{\partial^2 w}{\partial x^2}\right) - \\
&\quad-3I_{3y}\left[\tfrac{\partial u}{\partial x} + \tfrac12\left(\tfrac{\partial w}{\partial x}\right)^2\right]^2\cdot\left(\tfrac{\partial^2 w}{\partial x^2}\right)^2 + I_{4y}\left(\tfrac{\partial w}{\partial x}\right)^3\Bigg\}\Bigg\}\Bigg\} = 0\,,
\end{aligned} \tag{2.6}$$

(cf. [5]) where ϱ is the density, A is the cross-sectional area, I_y is the moment of inertia of the cross-section calculated for the axis y, $I_{ny}, n = 3, 4$ are the higher order moments of the cross-sectional area, L is the length of the belt between the belt pulleys, E is the linear part of the modulus of elasticity, β is the non-linear part of the modulus of elasticity. Equations of motions (2.5) and (2.6) describe the general motion of a single belt. When supplemented with the right fitting and boundary conditions, they are suitable for performing general dynamic analyses. Later on the above equations of motion (2.5) and (2.6) are regarded as our starting point for further research.

3. Analysis of transverse vibrations

When analyzing transverse vibrations, the non-linear partial differential equation system (2.5) and (2.6) is used as the starting point. Their accurate solution, suitable for engineering work, is not known yet. The method to be presented, based on Kirchhoff [2] and Kauderer [1], was used by Faragó [3] and Patkó [5] for belts as follows. In order to produce simpler equations of motion, the suppositions in [2] were used in (2.5), (2.6) according to which in the expression of the kinetic energy the coordinate $\left(\frac{\partial u}{\partial t}\right)$ in direction x of the velocity vector of the belt element performing the transverse vibration may be neglected beside the component $\left(\frac{\partial w}{\partial t}\right)$ in direction z. Thus, instead of (2.5) and (2.6) a simpler partial differential equation system is obtained. Relying on the train of thoughts by Kauderer and on the basis of the measurement results by Faragó, it is acceptable, as a first approximation in an analysis of transverse vibrations, to approximate the function $\sigma_x = \sigma_x(\varepsilon)$ by its linear part. Using the approximations mentioned, the system of the equations of motion (2.5) and (2.6) of the belt can be written in the form

$$\frac{\partial}{\partial x}\left\{AE\left[\frac{\partial u}{\partial x}+\frac{1}{2}\left(\frac{\partial w}{\partial x}\right)^2\right]\right\}=0 \tag{3.1}$$

$$\varrho A\frac{\partial^2 w}{\partial t^2}+\frac{\partial^2}{\partial x^2}\left(\frac{\partial^2 w}{\partial x^2}I_yE\right)-\frac{\partial}{\partial x}\left\{\frac{\partial w}{\partial x}\left\{AE\left[\frac{\partial u}{\partial x}+\frac{1}{2}\left(\frac{\partial w}{\partial x}\right)^2\right]\right\}\right\}=0. \tag{3.2}$$

Comparing equations (3.1) and (3.2) with (2.3) shows that the elongation of the center line of the belt does not depend on place x, therefore it can only depend on time t. Integrating (3.1) according to variable x gives the form

$$AE\left[\frac{\partial u}{\partial x}+\frac{1}{2}\left(\frac{\partial w}{\partial x}\right)^2\right]=F(t). \tag{3.3}$$

Equation (3.3) is again integrated along length L of the belt from $x=0$ to $x=L$, which gives

$$\frac{AE}{L}\left[u(L,t)-u(0,t)+\frac{1}{2}\int_{x=0}^{L}\left(\frac{\partial w}{\partial x}\right)^2\mathrm{d}x\right]=F(t). \tag{3.4}$$

Thus supposing a constant belt cross-sectional area from (3.2) and (3.4) for the function $w=w(x,t)$ describing the transverse vibrations gives the following integro-differential equation

$$\varrho A\frac{\partial^2 w}{\partial t^2}+I_yE\frac{\partial^4 w}{\partial x^4}-\frac{\partial^2 w}{\partial x^2}\left\{\frac{AE}{L}\left[u(L,t)-u(0,t)+\frac{1}{2}\int_{x=0}^{L}\left(\frac{\partial w}{\partial x}\right)^2\mathrm{d}x\right]\right\}=0. \tag{3.5}$$

There are time-dependent boundary conditions belonging to (3.5). If the coordinate system xyz is taken so that axis x passes through the current points of contact between the belt and the belt plates, then these boundary conditions can be formulated in the following forms

$$w\,(vt,t) = 0$$

and

$$w\,(vt + L, t) = 0,$$

where $v = constant$, the velocity of the belt in the coordinate system xyz. Let us

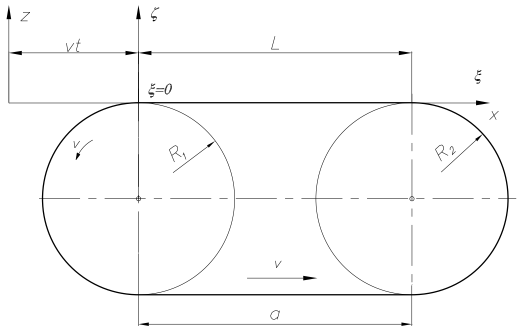

Figure 2. Mechanical model of the drive after transformation of coordinates

attach a coordinate system $\xi\eta\varsigma$ according to Figure 2 to the belt side in motion so that there should only be a translation in direction x between the coordinate systems xyz and $\xi\eta\varsigma$. Let us transform differential equation (3.5) into the coordinate system $\xi\eta\varsigma$ that the time dependence of the boundary conditions will be eliminated. Let us introduce the transformation

$$x = \xi + v \cdot t \tag{3.6}$$

according to Figure 2, thus the equation of motion is transformed into the form

$$\begin{aligned} &\varrho A \tfrac{\partial^2 w}{\partial t^2} - 2\varrho v A \tfrac{\partial^2 w}{\partial \xi \partial t} + \varrho A v^2 \tfrac{\partial^2 w}{\partial \xi^2} + I_y E \tfrac{\partial^4 w}{\partial \xi^4} - \\ -&\tfrac{\partial^2 w}{\partial \xi^2} \left\{ \tfrac{AE}{L} \left[u\,(L,t) - u\,(0,t) + \tfrac{1}{2} \int_0^L \left(\tfrac{\partial w}{\partial \xi} \right)^2 \mathrm{d}\xi \right] \right\} = 0 \end{aligned} \tag{3.7}$$

and the boundary conditions are transformed into the time-independent forms

$$w\,(0,t) = 0 \tag{3.8}$$

and

$$w\,(L,t) = 0. \tag{3.9}$$

Equation (3.7) is a non-linear partial integro-differential equation. In the analysis of certain types of non-linear vibrations the Galerkin method is widely used [6]. On the basis of observations and experience the solution of the above integro-differential equation (3.7) is looked for in the following trigonometric series

$$w(\xi,t)=\sum_{n=1}^{\infty} q_n(t)\sin\left(\frac{n\pi}{L}\xi\right), \tag{3.10}$$

the members of which are orthogonal in the interval $[0, L]$ and satisfy the boundary conditions (3.8) and (3.9). Then

$$\ddot{q}_k+\left(\tfrac{k\pi}{L}\right)^2\left\{\left(\tfrac{k\pi}{L}\right)^2\tfrac{I_y}{A}\tfrac{E}{\varrho}-v^2+\tfrac{E}{\varrho L}\left[u(L,t)-u(0,t)+\tfrac{\pi^2}{4L}\sum_{m=1}^{p}\left(m^2q_m^2\right)\right]\right\}q_k=0$$
$$(k=1,2,3,\dots,p) \tag{3.11}$$

is obtained. A detailed presentation of the calculations can be found in Appendix B. Let us introduce the notations

$$Q_k(\xi)=\sin\left(\frac{k\pi}{L}\xi\right)\qquad(k=1,2,3,\dots,p)$$

where the functions $Q_k(\xi)$ are from now on called vibration modes. On the basis of experience (cf. [7]) it can be supposed that the arising vibrations in the first approximation have the property that there is a dominant vibration mode $Q_k(\xi)$ and a dominant frequency belonging to them, beside which the amplitudes $q_m(t)$ belonging to the other $Q_m(\xi)$ $(m\neq k)$ are mostly negligibly small. Based on the above, in (3.11) only one such function $q_k(t)$ considered to be dominant is kept. Thus instead of (3.11) it is sufficient to analyse the differential equation

$$\ddot{q}_k+\left(\tfrac{k\pi}{L}\right)^2\left\{\left(\tfrac{k\pi}{L}\right)^2\tfrac{I_y}{A}\tfrac{E}{\varrho}-v^2+\tfrac{E}{\varrho L}\left[u(L,t)-u(0,t)+\left(\tfrac{k\pi}{2}\right)^2\tfrac{1}{L}q_k^2\right]\right\}q_k=0$$
$$(k=1,2,3,\dots,p)\ . \tag{3.12}$$

4. Stability analysis

4.1. **The exciting effect.** In order to investigate the stability of belt, let us linearise (3.12) at $q_{k0}=0$, which gives

$$\ddot{q}_k+\left(\frac{k\pi}{L}\right)^2\left\{\left(\frac{k\pi}{L}\right)^2\frac{I_y}{A}\frac{E}{\varrho}-v^2+\frac{E}{\varrho L}\left[u(L,t)-u(0,t)\right]\right\}q_k=0\ . \tag{4.1}$$

It can be seen from the equation of motion that one possible cause of the transverse vibrations of belts is the longitudinal elongation of the belt, which changes in time. Let us examine the case when the longitudinal displacement of the ends of the belts is caused by the eccentricity of one of the belt pulleys. Let us suppose that in the coordinate system $\xi\eta\zeta$ one end of the belt does not get displaced, that is

$$u(0,t)=0, \tag{4.2}$$

and its other end gets displaced by the value u_0 resulting from the pre-tensioning and the transferred moment, then performs an oscillatory motion described by the function $u_L=e_2\cos(\nu t)$ in direction ξ due to the eccentricity of one of the belt pulleys

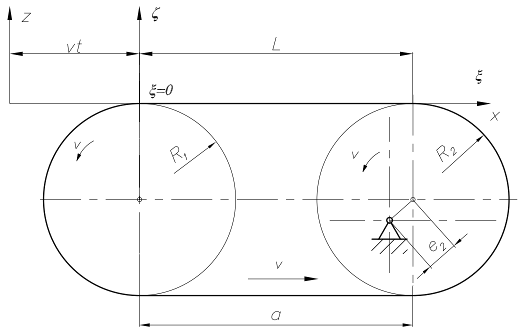

Figure 3. The model of a drive with eccentricity

(in this case the driven one), where e_2 is the eccentricity of the driven belt pulley, ν is its angular velocity, and using them gives

$$u(L,t) = u_0 + e_2 \cos(\nu t) \, . \tag{4.3}$$

The velocity of the belt can be expressed in terms of the angular velocity of the driving plate denoted by 1 and gives

$$v = R_1 \nu, \tag{4.4}$$

where ν is the angular velocity of the driving plate and R_1 is the radius of the driving plate – see Figure 3. Substituting equations (4.2)-(4.4) into (4.1), let us introduce the dimension-free time coordinate

$$\tau = \frac{1}{2}\nu t \, , \tag{4.5}$$

and we get

$$q_k^{''} + 4\left(\frac{k\pi}{L}\right)^2 \left\{ \left(\frac{k\pi}{L}\right)^2 \kappa(h) \frac{E}{\varrho \nu^2} - R_1^2 + \frac{E}{\varrho \nu^2 L}\left[u(L,\tau) - u(0,\tau)\right] \right\} q_k = 0$$

$$(k = 1,2,3,\ldots,p) \, , \quad (4.6)$$

where the comma denotes differentiation according to τ and $\kappa(h) = \sqrt{\frac{I_y}{A}}$ is the inertia-radius. Let us furthermore introduce the notations

$$\lambda_k = 4\left(\tfrac{k\pi}{L}\right)^2 \left\{ \tfrac{E}{\varrho \nu^2}\left[\left(\tfrac{k\pi}{L}\right)^2 \kappa(h) + \tfrac{u_0}{L}\right] - R_1^2 \right\} \, , \tag{4.7}$$

$$\mu_k = -2\left(\tfrac{k\pi}{L}\right)^2 \tfrac{E}{L\varrho \nu^2} e_2 \, . \tag{4.8}$$

Thus (4.6) will take the form

$$q_k^{''} + (\lambda_k - 2\mu_k \cos(2\tau))\, q_k = 0 \qquad (k = 1,2,3,\ldots,p) \, . \tag{4.9}$$

The stability ranges of the above Mathieu-type differential equations are known from the literature [1, 8]. The case $\lambda_k < 0$ is of no importance for practical belt drives. Among the instability ranges what is called the main instability range is the most dangerous, for here even for small μ_k values may arise stability loss in a wide interval

λ_k. The other instability ranges are of smaller significance due to the dampings not taken into account here. Therefore this paper is limited to an analysis of the main instability range. It should be noted here that due to the damping present in the system, but not taken into account now, the sizes of the instability ranges decrease.

4.2. **First approximation of the main instability ranges.** Practical calculations show that the values μ_k in belt drives are small, therefore in the first approximation

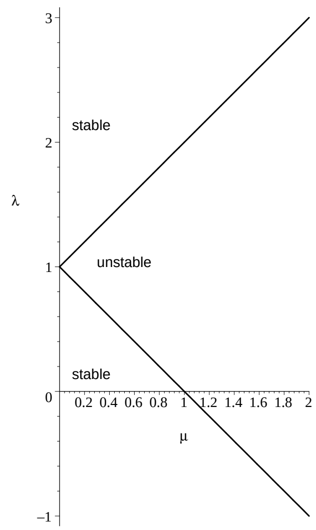

Figure 4. First approximation of the main instability range of the Mathieu equation

it is sufficient to approximate the main instability range by its tangents. Accordingly, the main instability range of (4.9) is approximated – see Figure 4. – in the form

$$\lambda_k = 1 \pm \mu_k \ . \tag{4.10}$$

Substituting the variables (4.7)-(4.8) into (4.10) and solving the expression obtained for angular velocity ν of the belt plates, the relationship

$$\nu = 2k\pi\sqrt{\frac{E\left[k^2\pi^2 I_y + LA\left(u_0 \pm \frac{e_2}{2}\right)\right]}{\varrho AL^2\left(4k^2\pi^2 R_1^2 + L^2\right)}} \tag{4.11}$$

is obtained. It means that the unstable angular velocities are in the region

$$2k\pi\sqrt{\frac{E\left[k^2\pi^2 I_y + LA\left(u_0 - \frac{e_2}{2}\right)\right]}{\varrho AL^2\left(4k^2\pi^2 R_1^2 + L^2\right)}} < \nu < 2k\pi\sqrt{\frac{E\left[k^2\pi^2 I_y + LA\left(u_0 + \frac{e_2}{2}\right)\right]}{\varrho AL^2\left(4k^2\pi^2 R_1^2 + L^2\right)}} \ . \tag{4.12}$$

It describes the first approximation of the main instability range as depending on the further belt parameters. The following is an analysis of how the positions of the main instability ranges change for different vibration patterns.

4.3. **Analysis of the impact of vibration patterns.** It can be seen from equation (4.11) as well as from the Figures that when number k of the vibration pattern being analysed is increased, the instability range moves towards the higher revolution numbers. It can be observed and can also be seen from relationship (4.11) that for higher values of k and for the usual belt parameters the ranges become slightly wider.

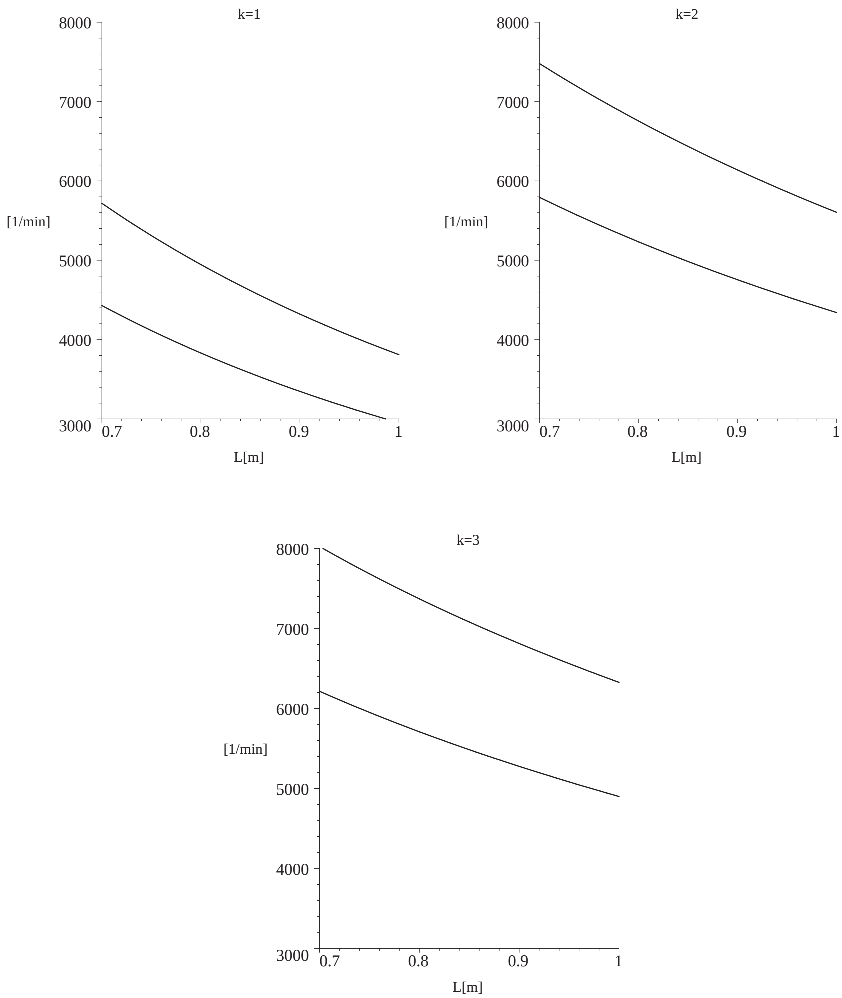

Figure 5. First approximations of the main instability domains for $k = 1, 2, 3$, $e_2 = 3 \cdot 10^{-3}[m]$, $I_y = 3.2 \cdot 10^{-11}[m^4]$, $\varrho = 2 \cdot 10^3[kg/m^3]$, $E = 1.5 \cdot 10^9[N/m^2]$, $A = 2.1 \cdot 10^{-7}[m^2]$, $R_1 = 0.1[m]$, $u_0 = 6 \cdot 10^{-3}[m]$

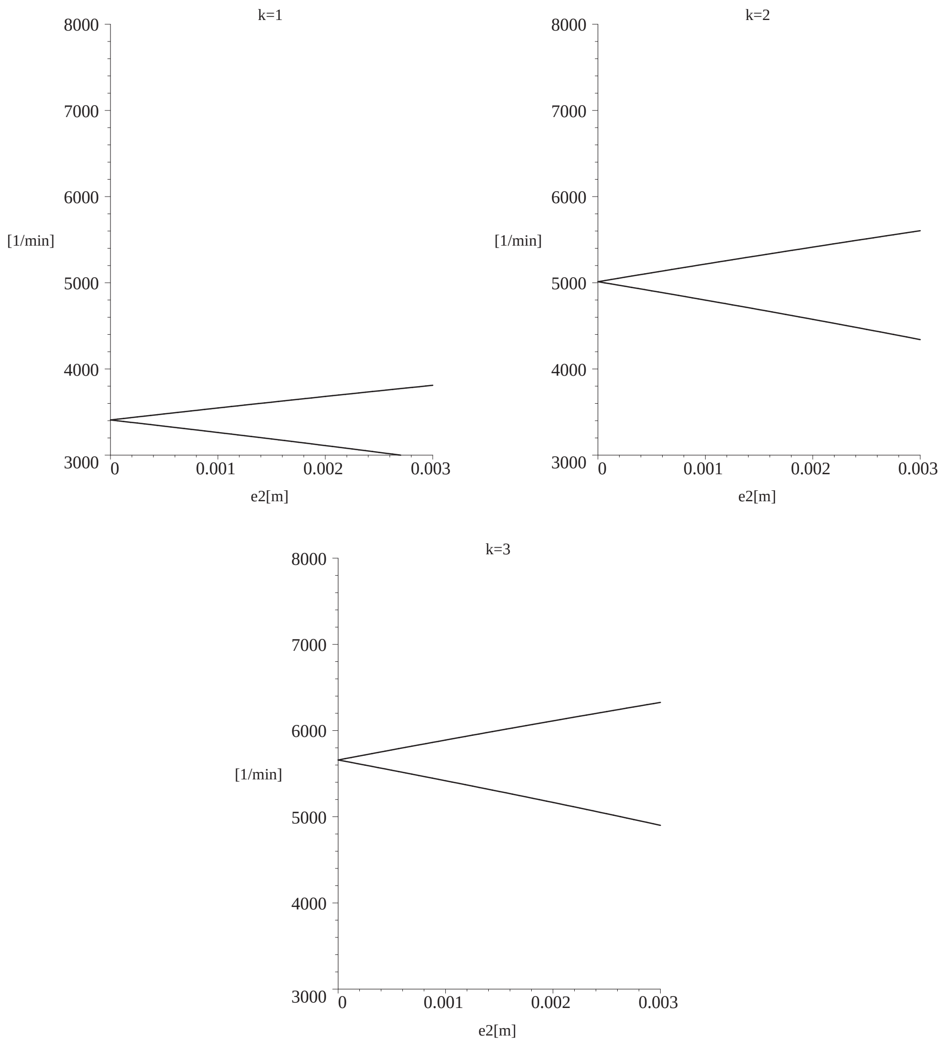

Figure 6. First approximations of the main instability domains for $k = 1, 2, 3,\ L = 1[m], I_y = 3.2 \cdot 10^{-11}[m^4], \varrho = 2 \cdot 10^3[kg/m^3], E = 1.5 \cdot 10^9[N/m^2], A = 2.1 \cdot 10^{-7}[m^2], R_1 = 0.1[m], u_0 = 6 \cdot 10^{-3}[m]$

Figure 5 shows the boundaries of the instability ranges calculated from (4.11) with the values $k = 1, 2, 3$. In the diagrams of Figure 5 the instable angular velocity range is drawn versus length L of the belt. In the diagrams of Figure 6 the unstable angular velocity range is drawn versus eccentricity e_2 of the pulley. It can be seen from the Figures that certain revolution number ranges may become dangerous even for different vibrations. Relationship (4.12) lends itself to further noteworthy conclusions. The formula shows what impact the belt parameters exert on the positions and dimensions of unstable ranges.

5. Concluding remarks

The paper has shown more general equations of motion of transverse vibrations of belts than those known from the literature. These are the equations of motion (2.5), (2.6), (3.5) and (3.11), which take into account the non-linear behaviour of the belts and also provide a basis for further research. Based on the above, it can be stated that one possible cause of the transverse vibrations of belts is the eccentricity of the belt pulleys. In that case the transverse vibrations are described by a differential equation system with a non-linear variable coefficient. The stability analysis of the belt has also been presented. The first approximation of the main instability range has been performed versus the angular velocity of the belt pulley. It has been investigated how the main instability domains of the transverse vibrations of a belt change with the different vibration patterns. It was found that the main instability ranges belonging to the higher vibration patterns move towards the higher numbers of revolution and become slightly wider.

Acknowledgement. The authors express their thanks to research project OTKA No T042 657, which has significantly contributed to concluding the research.

References

1. Kauderer, H.: *Nichtlineare Mechanik*, Springer Verlag, Berlin-Göttingen-Heidelberg, 1958.
2. Kirchhoff, G.: *Mathematische Physik*, Teubner Verlag, Leipzig, 1967.
3. Faragó, K.: *Non-linear vibrations of the main drives of machine tools combined with belt drives*, University of Miskolc, Ph. D. Dissertation, 1986. (in Hungarian)
4. Yue, M. G.: *Transverse Vibration in Belt Drives*, Chalmers University of Technology, Göteborg, Sweden, Dissertation, 1994.
5. Patkó, G.: *Dynamical Results and Applications in Machine Design.* Miskolci Egyetem, 1998. (in Hungarian)
6. Forbat, N.: *Analytische Mechanik der Schwingungen*, VEB Deutscher Verlag der Wissenschaften, Berlin, 1966.
7. Fischer, U. and Stephan, W. *Mechanische Schwingungen*, VEB Fachbuchverlag, Leipzig, 1981.
8. Bolotin, W.W.: *Kinetische Stabilität elastischer Systeme*, VEB Deutscher Verlag der Wissenschaften, Berlin, 1961.

Appendix A. Derivation of the equations of motion

The Hamilton integral is

$$H = \int_{t=t_1}^{t_2} (W - T)\,\mathrm{d}t, \tag{A.1}$$

where W represents the strain work of the belt, and T is its kinetic energy. Let us first determine the strain work resulting from the flexible displacements in the transverse and longitudinal directions of the belt cross-sections. Let U be the strain work of the belt for unit volume. Then, using (2.1)

$$\bar{U} = \int_{\varepsilon_x=0}^{\varepsilon_x} \left(E\varepsilon_x + \beta\varepsilon_x^3\right) \mathrm{d}\varepsilon_x = \frac{1}{2}E\varepsilon_x^2 + \frac{1}{4}\beta\varepsilon_x^4 \tag{A.2}$$

can be written. The strain work of the belt for unit length can be calculated by using (2.4) and (A.2) according to

$$U = \iint_A \bar{U}\mathrm{d}y\mathrm{d}z, \tag{A.3}$$

where A is the cross-section of the belt. Giving details of expression (A.3)

$$\begin{aligned} U = {} & \tfrac{1}{2}E \textstyle\iint_A \left[\frac{\partial u}{\partial x} + \frac{1}{2}\left(\frac{\partial w}{\partial x}\right)^2 - z\frac{\partial^2 w}{\partial x^2}\right]^2 \mathrm{d}y\mathrm{d}z + \\ & + \tfrac{1}{4}\beta E \textstyle\iint_A \left[\frac{\partial u}{\partial x} + \frac{1}{2}\left(\frac{\partial w}{\partial x}\right)^2 - z\frac{\partial^2 w}{\partial x^2}\right]^4 \mathrm{d}y\mathrm{d}z \end{aligned} \tag{A.4}$$

is obtained. When U is known, the strain work accumulated in the belt can be calculated as

$$W = \int_{x=0}^{L} U\mathrm{d}x,$$

which is detailed to give the following integral

$$\begin{aligned} W = {} & \tfrac{1}{2}\textstyle\int_{x=0}^{L} \left\{ E\left\{ A\left[\frac{\partial u}{\partial x} + \frac{1}{2}\left(\frac{\partial w}{\partial x}\right)^2\right]^2 + I_y\left(\frac{\partial^2 w}{\partial x^2}\right)^2 \right\} + \right. \\ & + \tfrac{1}{2}\beta\left\{ A\left[\frac{\partial u}{\partial x} + \frac{1}{2}\left(\frac{\partial w}{\partial x}\right)^2\right]^4 + 6I_y\left[\frac{\partial u}{\partial x} + \frac{1}{2}\left(\frac{\partial w}{\partial x}\right)^2\right]^2\left(\frac{\partial^2 w}{\partial x^2}\right)^2 - \right. \\ & \left.\left. - 4I_{3y}\left[\frac{\partial u}{\partial x} + \frac{1}{2}\left(\frac{\partial w}{\partial x}\right)^2\right]^2\left(\frac{\partial^2 w}{\partial x^2}\right)^3 + I_{4y}\left(\frac{\partial^2 w}{\partial x^2}\right)^4 \right\} \right\} \mathrm{d}x. \end{aligned} \tag{A.5}$$

In the integration of function $\bar{U}$ the facts that the first moment $S_y = \iint_A z\mathrm{d}y\mathrm{d}z$ of the belt cross-section calculated for its centroidal axis is zero and that the quantity $\iint_A z^i\mathrm{d}y\mathrm{d}z$ was designated I_{iy} $(i = 3, 4)$ were made use of.

Let us now turn to calculating the kinetic energy of the elementary belt. Let the mass of the belt per unit length be denoted by $m_0 = \varrho A$. The velocity of one point of the central line of the belt is calculated according to

$$v_0 = \sqrt{\left(\frac{\partial u}{\partial t}\right)^2 + \left(\frac{\partial w}{\partial t}\right)^2}. \tag{A.6}$$

If the moments of inertia of the individual belt elements are neglected - and thus the kinetic energy resulting from the angular velocities of the revolutions of the cross-sections is also neglected - then the kinetic energy can be written as

$$T = \frac{1}{2}m_0 \int_{x=0}^{L} \left[\left(\frac{\partial u}{\partial t}\right)^2 + \left(\frac{\partial w}{\partial t}\right)^2\right] \mathrm{d}x. \tag{A.7}$$

If now the relationships (A.5) and (A.7) are substituted into (A.1), this gives the integral of form

$$H = \int_{t=t_1}^{t_2} \int_{x=0}^{L} F\left(\frac{\partial u}{\partial t}; \frac{\partial u}{\partial x}; \frac{\partial w}{\partial t}; \frac{\partial w}{\partial x}; \frac{\partial^2 w}{\partial x^2}\right) \mathrm{d}x\mathrm{d}t \tag{A.8}$$

from which the Euler-Lagrange equations

$$\frac{\partial}{\partial x} \frac{\partial F}{\partial\left(\frac{\partial u}{\partial x}\right)} + \frac{\partial}{\partial t} \frac{\partial F}{\partial\left(\frac{\partial u}{\partial t}\right)} = 0 \tag{A.9}$$

$$\frac{\partial w}{\partial x} \frac{\partial F}{\partial\left(\frac{\partial w}{\partial x}\right)} - \frac{\partial^2}{\partial x^2} \frac{\partial F}{\partial\left(\frac{\partial^2 w}{\partial x^2}\right)} + \frac{\partial}{\partial t} \frac{\partial F}{\partial\left(\frac{\partial w}{\partial t}\right)} = 0 \tag{A.10}$$

can be derived [1] on the basis of the Hamilton variation principle ($\delta H = 0$). Completing the differentiations designated gives the differential equations (2.5) and (2.6) describing the motion of the belt.

Appendix B. Details of the calculations using the Galerkin method

According to (3.7) the equation of motion can be written in the form

$$\begin{aligned} &\varrho A \frac{\partial^2 w}{\partial t^2} - 2\varrho v A \frac{\partial^2 w}{\partial \xi \partial t} + \varrho A v^2 \frac{\partial^2 w}{\partial \xi^2} + I_y E \frac{\partial^4 w}{\partial \xi^4} - \\ &\qquad - \frac{\partial^2 w}{\partial \xi^2} \left\{ \frac{AE}{L} \left[u(L,t) - u(0,t) + \frac{1}{2} \int_0^L \left(\frac{\partial w}{\partial \xi}\right)^2 \mathrm{d}\xi \right] \right\} = 0 \end{aligned} \tag{B.1}$$

and the boundary conditions are transformed into the time-independent forms

$$w(0,t) = 0 \tag{B.2}$$

and

$$w(L,t) = 0. \tag{B.3}$$

The solution of equation (B.1) is sought following Galerkin's method in the form

$$w(\xi,t) = \sum_{n=1}^{\infty} q_n(t) \sin\left(\frac{n\pi}{L}\xi\right) \tag{B.4}$$

which satisfies the boundary conditions (B.2) and (B.3). Substituting (B.4) in the equation of motion (B.1) results in equation

$$\begin{aligned} &\sum_{n=1}^{\infty} \left\{ \left\{ \varrho A \ddot{q}_n - \varrho A v^2 \frac{n^2\pi^2}{L^2} q_n + I_y E \frac{n^4\pi^4}{L^4} q_n + \left(\frac{n^2\pi^2}{L^2} q_n\right) \left\{ \frac{AE}{L} \left[u_L(t) + \right.\right.\right.\right. \\ &\qquad \left.\left.\left.\left. + \frac{L}{4} \sum_{k=1}^{\infty} \left(\frac{k^2\pi^2}{L^2} q_k^2\right) \right] \right\} \right\} \sin\left(\frac{n\pi}{L}\xi\right) \right\} = 0\,. \end{aligned} \tag{B.5}$$

Let us multiply equation (B.5) by the expression $\sin\left(\frac{i\pi}{L}\xi\right)$, then integrate it on the interval $[0, L]$. In accordance with Galerkin's method, the equation

$$\sum_{n=1}^{\infty}\left\{\left\{\varrho A\ddot{q}_n - \varrho A v^2 \frac{n^2\pi^2}{L^2} q_n + I_y E \frac{n^4\pi^4}{L^4} q_n + \left(\frac{n^2\pi^2}{L^2} q_n\right)\left\{\frac{AE}{L}\left[u_L(t) + \right.\right.\right.\right.$$
$$\left.\left.\left.\left. + \frac{L}{4}\sum_{k=1}^{\infty}\left(\frac{k^2\pi^2}{L^2} q_k^2\right)\right]\right\}\right\}\right\}\int_{\xi=0}^{L}\sin\left(\frac{n\pi}{L}\xi\right)\sin\left(\frac{i\pi}{L}\xi\right)\mathrm{d}\xi = 0 \quad \text{(B.6)}$$

can be written. Completing the integrations designated gives equation

$$\varrho A\ddot{q}_i + \frac{i^2\pi^2}{L^2}\left[I_y E \frac{i^2\pi^2}{L^2} - \varrho A v^2 + \frac{AE}{L}\left(u_L(t) + \frac{\pi^2}{4L}\sum_{k=1}^{\infty} k^2 q_k^2\right)\right] q_i = 0. \quad \text{(B.7)}$$

Journal of Computational and Applied Mechanics, Vol. 6., No. 1., (2005), pp. 129–143

NUMERICAL SUPPORT FOR RESIDUAL STRESS MEASUREMENT BY THE HOLE DRILLING METHOD

Michal Švantner
University of West Bohemia, New Technologies-Research Centre
Univerzitní 22, 306 14 Plzen, Czech Republic
msvantne@ntc.zcu.cz

[Received: November 26, 2003]

Abstract. The hole drilling technique is one of the most frequently used methods of residual stress determination. This technique is based on drilling a small hole in the material. Relieved strain around the hole is measured and the residual stress is then evaluated using calibration coefficients. Possibilities of calibration coefficient computation using finite element method (FEM) are presented in this paper. Analyses of computation parameters influence are performed: the solver used and its parameters, finite element types, model type, mesh density and sample shape. An efficient method using a script-based model for the calibration function determination is introduced.

Mathematical Subject Classification: 74S05
Keywords: residual stress, hole drilling method, calibration coefficients, FEM

1. Introduction

Residual stress is defined as stress in a material without the action of external forces. It occurs practically in all technical materials as a consequence of their manufacturing, treatment or usage. Residual stress influences detrimentally or beneficially the resulting properties: toughness or fatigue and corrosion characteristics for example. Residual stress represents one of the important material state characteristics together with microstructure and texture, hence a great care is given to its determination.

Experimental techniques play the main role in residual stress determination. Several *destructive* or *nondestructive* experimental methods based on different physical principles are developed [3]. Frequently used ones include diffraction (x-ray, neutron) techniques, ultrasonic techniques, bending methods or destructive techniques based on residual stress relieving measurement. The *hole-drilling* residual stress measurement method [2,3,6,7,11] is a destructive technique based on the original residual stress relieving by drilling a small hole into the material surface. The method is labelled as *semi-destructive*, as the material damage is very small and often removable. The response of the relaxed stress-relieved strain is measured during incremental hole drilling and the original residual stress is evaluated based on this measurement. Strain gauge or optical [8] methods are most often used for strain measurement. The standard ASTM E837 [12] has been adopted as the basic concept of the method, however, many modifications and improvements have been developed.

Generally, a blind hole and a non-uniform stress field is considered. The relaxed strains measured are related to the acting residual stress with so-called influence function or calibration coefficients (discrete form) in this case. The influence function depends on the material properties, hole and strain gauges geometry, hole depth and the position of the residual stress acting in the hole. In some cases (uniform stress field, homogeneous isotropic material, etc.) an experimentally evaluated influence function is sufficient. However, in most cases a numerical calibration of the method is necessary.

Numerical techniques are used both for residual stresses prediction or as an experimental method support. The residual stress calibration coefficient can also be determined using the numerical modeling [4,5,9]. This allows more accurate influence function determination and the hole drilling residual stress measurement problem analysis. In this way, calibration coefficients can be efficiently obtained for different materials, the influence of sample shapes (some analysis provided in [1]) and properties as well as other factors can be investigated. Therefore, the numerical simulation appears an efficient tool, which can help to enhance the experimental method compatibilities and the generalization of its application.

2. Hole drilling residual stress measurement method

The semi-destructive hole drilling residual stress measurement technique is based on drilling a small hole to the material surface measured. The principle of the method is schematically shown in Figure 1. A conical shaped mill is used for the drilling; the original residual stress relaxation response that is the relieved strain is measured usually by a strain gauge rosette with 3 gauge elements.

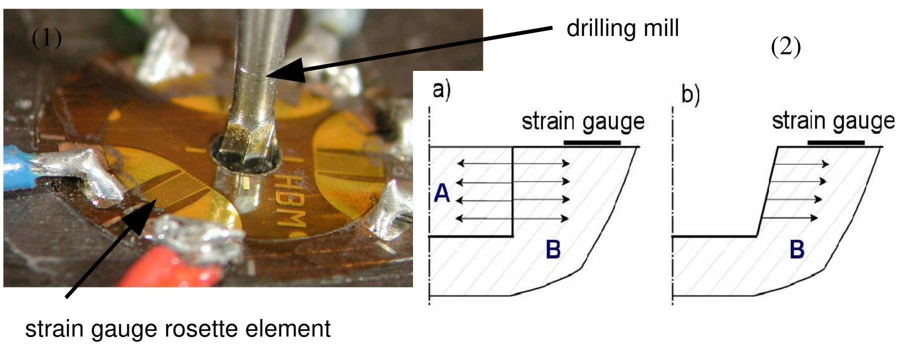

Figure 1. Schematic photograph of the drilling mill and strain gauge rosette (1), principle of the hole drilling residual stress measurement technique before drilling (2a); after drilling (2b).

The relationship between the residual stress relaxation and the surface relieved strain is based on equation

$$\varepsilon_r = A\,(\sigma_x + \sigma_y) + B\,(\sigma_x - \sigma_y)\cos(2\theta)\ , \tag{1}$$

where ε_r is the relieved radial strain at angle θ, σ_x and σ_y are the residual stress components in principal directions and A, B are calibration coefficients. Equation (1) is analytically derived by Kirsch (1898) for through-hole and the coefficient definitions are

$$A = -\frac{1+\nu}{2E}\frac{1}{R^2} \tag{2}$$

and

$$B = -\frac{1+\nu}{2E}\left(\frac{4}{1+\nu}\frac{1}{R^2} - \frac{3}{R^4}\right)\ . \tag{3}$$

where ν and E are Poisson ratio and Young elasticity modulus of the measured material and R is the measuring position for r relative to the hole-radius r_a:

$$R = \frac{r}{r_a}\ . \tag{4}$$

Equation (1) stands for a homogeneous isotropic material with linear elastic stress-strain relationship. Strain measurement in 3 independent directions (θ, $\theta + 45^o$, $\theta + 90^o$ for the ASTM E837 strain gauge rosette) allows determination of the two principal residual stress components and their directions. The analytical derivation is performed assuming an infinite plate with a small hole in 2-dimensional simplification for a constant stress-depth profile. If these conditions are not fulfilled, such simplification is not possible.

Let us suppose the frequently assumed case of a homogeneous, isotropic and linear elastic material, a blind hole and a non-uniform stress profile. Similar form of the stress-strain relationship as in the case of equation (1) is considered. However, the stresses $\sigma_x(H)$ and $\sigma_y(H)$ are additionally a function of position in the hole H; $\varepsilon_r(h)$ is a function of hole depth h; calibration coefficients $A(h,H)$, $B(h,H)$ are functions of the whole hole depth h and the position H. Then the dependence (1) for $\theta = 0$ and $\theta = 90^o$ can be written (integral form proposed by Schajer [8])

$$\varepsilon_{r(x,y)}(h) = \int\limits_0^h A(h,H)\,[\sigma_x(H) + \sigma_y(H)] \pm B(h,H)\,[\sigma_x(H) - \sigma_y(H)]\,dH \tag{5}$$

Severel residual stress evaluation schemes based on different simplifications have been developed (integral method, power series method, etc.). A discrete form of equation (5) is used for the numerical evaluation of the calibration functions (A, B). Such equation is the basis for the integral evaluation method [7] and can be written as

$$\vec{\varepsilon}_{r(x,y)} = [A]\vec{\sigma}_A \pm [B]\vec{\sigma}_B\ , \tag{6}$$

where $\vec{\varepsilon}_r$ is the vector of radial surface strain by discrete depths h_i in the directions $\theta = 0$ or $\theta = 90^o$, $\vec{\sigma}$ is the stress vector ($\sigma_A = \sigma_x + \sigma_y$, $\sigma_B = \sigma_x - \sigma_y$) while $[A], [B]$ are lower triangular coefficient matrices.

In this way the calibration coefficients are evaluated based on given ‘residual’ stress (boundary condition) and strain at the strain gauge rosette elements’ position (computation result). The common form of the coefficients is the dimensionless cumulative strain relieving function:

$$a_{ij} = \frac{2E}{1+\nu} \int\limits_0^{H_j} A(h_i, H) dH \;, \tag{7a}$$

$$b_{ij} = 2E \int\limits_0^{H_j} B(h_i, H) dH \;. \tag{7b}$$

These dimensionless coefficients are considered material independent (only small dependence up to 2% on Poisson ratio ν is observed [11]) and thus they are functions of the hole and strain gauge rosette geometry only (with respect to the above mentioned conditions).

3. Numerical model - solvers’ comparison

The blind-hole analysis is generally a 3 dimensional problem. In some cases a 2 dimensional approximation can be used. The numerical finite element method (FEM) system *Cosmos/M* [10] offers three possible models (linear static analysis):

- 3D model
- 2D axially symmetric model
- 2D axially symmetric model (geometry) with asymmetric loading (NAL-model)

Standard numerical solvers (SPARSE or SKYLINE) or the fast FFE solver developed by SRAC (Structural Research & Analysis Corp.) can be used for both 2D and 3D models (except the NAL-model).

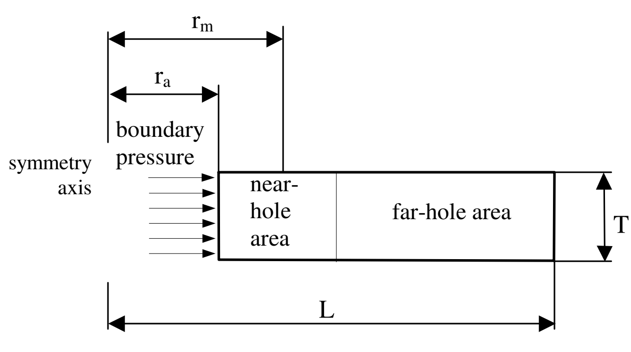

Figure 2. Through-hole linear static problem analysis scheme.

An axially symmetric through-hole problem is modeled according to the schema shown in Figure 2 for the solvers/models comparison. The model parameters are presented in Table 1. The hole radius and measuring point position are considered in accordance with the HBM (Hottinger Baldwin Messtechnik) drilling mill used and strain gauge rosette dimensions. The steel material is considered. Constant radial pressure $\sigma_{r,b}$ is set as the boundary condition to simulate the relieved tensile residual stress.

The most often used scale is the strain gauge rosette mean radius (r_m - rosette strain gauge element center radius), however, dimensions in this paper are presented relative to the hole radius, which is the main scale of the problem.

Table 1. Through-hole linear static analysis problem parameters (element size values are only approximate, the program can adapt the mesh during automatic mesh generation)

Parameter	**Value**	**Unit**
Hole radius (r_a) - reference size	0.90	mm
Strain gauge rosette mean radius ($R_m = r_m/r_a$)	2.83	-
Sample length (L/r_a)	20.00	-
Sample thickness (T/r_a)	5.00	-
Element size ratio (by 3D model)	1.20	-
Near hole area length (by 2D model, L_1/r_a)	5.67	-
Minimum size of elements (e_{min}/r_a)	0.10	-
Maximum size of elements (e_{max}/r_a)	0.50	-
Boundary pressure ($\sigma_{r,b}$)	100.00	MPa
Density (ρ)	7700.00	kg/m^3
Elasticity modulus (E)	210.00	GPa
Poisson ratio (ν)	0.28	-

Generated mesh types are shown in Figure 3. The object is divided into two parts by the 2D problem mesh (see Figure 2). The near-hole part of the length $L_1 = 5.67r_a = 2r_m$ is meshed by constant element size e_{min}, the far-hole part is meshed with increasing element size from e_{min} up to e_{max} at the object boundary. The triangular (TRIANG) 3-node element mesh with 2 translational degrees of freedom per node is used for the axially symmetric problem.

The principle of the symmetric model with asymmetric loading (NAL-solver) is based on the load $F(\theta)$ decomposition to the sum of several harmonic components of the Fourier series

$$F(\theta) = P_0 + P_1\cos(\theta) + ... + P_n\cos(n\theta) + Q_0 + Q_1\sin(\theta) + \\ ... + Q_n\sin(n\theta) \; . \tag{8}$$

Then a 2D problem can be solved for each component and the particular solutions are superposed (linear static analysis). The load is defined as a function of angle (definition curve) and the decomposition is done automatically in the *Cosmos/M* system. This NAL-solver does not support triangular mesh and thus PLANE2D 4-node quadrilateral element mesh is used (two nodes can be coincident). In the general case 3 translational degrees of freedom per node are considered.

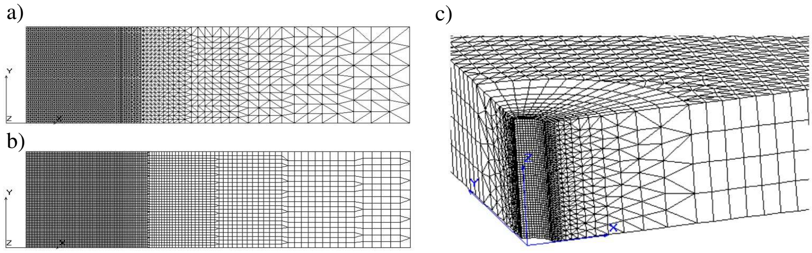

Figure 3. Through-hole linear static analysis mesh – (a) 3-node triangular 2D mesh, (b) 4-node 2D quadrilateral mesh , (c) 3D 8-node isoparametric solid mesh

8-node SOLID elements are generated for 3D analysis (special cases are prism and pyramid elements), where translational degrees of freedom per node are considered. The near-hole part is meshed with increasing element size from e_{min} up to e_{max} and the far-hole part element size e_{max} is constant with regard to mesh size requirements.

Both 2D and 3D solvers except the NAL-solver make it possible to use the first (linear) order or the second (parabolic) order elements. As an example, middle nodes on TRIANG 2nd order elements straight edges are considered in the analysis. This feature is not supported by the NAL-solver, where the mesh has to be refined manually.

The radial stress $\sigma_{r,m}$ at the mean strain gauge rosette radius is considered to be the value to be compared. The results are presented relatively to the boundary stress $\sigma_{r,b}$. Results of the SPARSE solver with 2nd order element option are considered to be a base for the percentage differences expression. Results for an axially symmetric through-hole problem are in Table 2.

The results show that there is only a small difference up to 0.4% between all 2D models. Similar solution times correspond to the number of equations solved and do not exceed one minute (data given by Cosmos/M output file). No considerable differences in accuracy or solution-time requirements are observed between SPARSE and FFE solvers.

The results of 3D models are significantly influenced by increasing elements size in the near-hole area. In this case the difference (error) can reach up to 20% by disabling the 2nd order element option. By enabling this option both the SPARSE and FFE results are comparable with 2D solution ($\Delta\sigma_{r,m}$ = 0.1 and 3.2%). The requirements (number of solved equations) of 3D solution are significantly higher than 2D simplification, thus the solution times are also longer. A huge solution time requirement increase can be seen in 3D STAR 2nd order element solution. This is caused by disc swapping due to the insufficient computer operating memory (512 MB RAM). Using the FFE solver can reduce the solution time significantly, however, the result accuracy is worse (difference about 3%).

Table 2. Result and parameter comparison for different computational models - axially symmetric through-hole problem. Comp. PC x86 533MHz, 512 MB RAM

Option	$\sigma_{r,m}/\sigma_{r,b}$ (-)	$\lvert\Delta\sigma_{r,m}\rvert$ (%)	Number of eqns.	Number of elements	Number of corner nodes	Solution time (s)	Element type
2D Sym., SPARSE, 2nd order el. (base)	-0.12231	0.0	26299	6505	3365	8	TRIANG
2D Sym., SPARSE	-0.12284	0.4	6645	6505	3365	2	TRIANG
2D Sym., FFE, 2nd order el.	-0.12233	0.0	26468	6505	3365	4	TRIANG
2D Symmetric, FFE	-0.12278	0.4	6730	6505	3365	2	TRIANG
3D, SPARS, 2nd order el.	-0.12249	0.1	154016	15266	9512	5438	SOLID
3D, SPARS	-0.14669	19.9	26654	15266	9512	78	SOLID
3D, FFE 2nd order el.	-0.11845	3.2	134193	15266	9512	110	SOLID
3D, FFE	-0.14597	19.3	28536	15266	9512	28	SOLID
2D Asymmetric (SPARSE), high el. dens.	-0.12238	0.1	24053	7920	8067	15	PLANE2D
2D Asymmetric (SPARSE)	-0.12239	0.1	10572	3453	3561	8	PLANE2D

The NAL-solver provides accurate enough results ($\Delta\sigma_{r,m} = 0.1$ %). The solution time is comparable with axially symmetric solvers, but it is influenced by other solver-settings (see later).

The 3D solution is much more space- and time-consuming for similar result accuracy in comparison with the 2D model, especially in case of disc swapping mode transition. The 2D axially symmetric model with asymmetric loading solver appears to be an efficient way to solve such problems.

4. **Model parameter influence**

The surface stress/strain sensitivity related to the relieved residual stress due to the hole drilling is relatively small (about 12% by through-hole, see Table 2), hence the highest possible coefficient accuracy, i.e. computational accuracy, is required. The results can be influenced not only by incorrect solver parameters, but also due to the real sample and model geometry differences. Thus an analysis of mesh density, asymmetric loading curve value density, sample length and thickness is performed.

Assuming the parameters according to Table 1 (through-hole) the results obtained making use of the numerical model are compared to the analytic solution by Kirsch in Table 3. It can be seen that the results do not agree (difference about 2%) for the sample length 20·r$_a$ used in previous analysis. This length is insufficient to the approximate an infinite sample dimension considered by analytical derivation. The approximation is significantly better (difference about 0.3%) for 100·r$_a$ sample length setting.

Table 3. Asymmetric loading through-hole analysis results

Sample length (L/r$_a$)	$\sigma_{r,m}/\sigma_{r,b}$**(-)**	$\Delta\sigma_{r,m}$ **(%)**
Analytic (infinite)	-0.12457	0.0
20	-0.12231	1.8
100	-0.12426	0.3

In numerical modeling the infinite sample approximation is not necessary, but the demonstration of the sample dimensions' influence and the results' analytical verification is important. Let us further consider the more general case of a blind hole and an asymmetric residual stress profile, i.e. asymmetric loading boundary conditions. The model parameters correspond to those in Table 1, additional or changed parameters are in Table 4. The 2D symmetric solver with asymmetric loading

Table 4. Blind-hole linear static analysis basic model parameters; asymmetric loading (a supplement to Table 1)

Parameter	**Value**	**Unit**
Hole depth (h/r$_a$)	1.00	-
Sample length (L/r$_a$)	50.00	-
Sample thickness (T/r$_a$)	50.00	-
FCOEF curve values	73.00	-
Boundary pressure ($\sigma_{x,b}$)	100.00	MPa
Boundary pressure ($\sigma_{y,b}$)	0.00	MPa

(NAL-solver) is used for simulations. Hole depth h is chosen to be the same as the hole radius r_a; sample length and thickness are both $50r_a$ for the basic case. The tensile residual stress profile in x direction (100 MPa) is considered, i.e. a boundary pressure $\sigma_{x,b} = 100MPa$ is set. The boundary pressure is divided into a radial and a tangential component

$$\sigma_r = \sigma_x \cos^2\theta \ , \tag{9a}$$

$$\tau_{\theta r} = -\sigma_x \sin\theta\cos\theta \ . \tag{9b}$$

Separate simulations are performed for each radial and tangential load case. The results are superposed (solver requirements). Equations (9a,b) define the angle dependent load, which is set in form of an angle-load dependence curve (FCOEF) from -180^o to 180^o. The number of FCOEF entered values, i.e. the $\Delta\theta$ angle step should correspond to the function tangential changes intensity. FCOEF=73 ($\Delta\theta = 5^o$) is chosen as the basic case.

The number of Fourier series components n used in equation (8), i.e. the number of a particular solution computed, is one of the parameters that control the solution time-requirements. The system Cosmos/M allows function decomposition up to 1000 Fourier series components, however, use of the first three is sufficient in this case regarding the dependencies given by equations (9a,b).

The mesh shown in Figure 4 is constructed similarly to the through-hole case: the near-hole area ($5.66r_a$ in radial direction, $4.25r_a$ in axial direction) is meshed by constant element size e_{min}, the far-hole area is meshed with increasing element size from e_{min} to e_{max} at the object boundary. The mesh density influence near the hole is shown in Figure 5. The results show that mesh density influences the stress/strain field in the hole close vicinity above all. Using an element size smaller than $0.2r_a$ produces a maximum error of about 0.2%, increasing of the element size can cause an inaccuracy up to a few percents. The results, however, are hole-depth dependent and the smallest possible elements are required especially by incremental hole-drilling simulation. Each increment is significantly smaller than the overall hole-depth, thus the element size should be comparable or smaller than the increment size. Moreover, the strain value needed for the calibration coefficient evaluation should correspond to an integral strain value over the whole strain gauge element area, contrary to one-point stress value used for this comparison. Thus, regarding the increasing error in the hole vicinity as shown in Figure 5b, the sparse-mesh caused errors can be higher than those presented in Figure 5a.

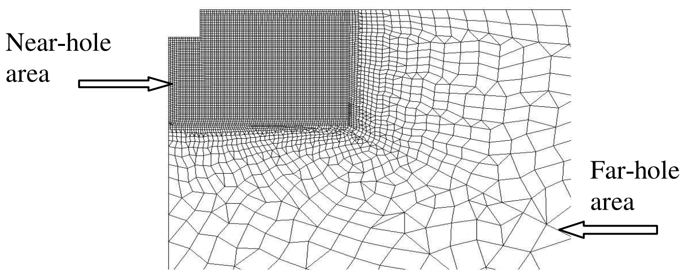

Figure 4. PLANE2D mesh generated for the blind-hole analyses (symmetric geometry, asymmetric loading)

One of the NAL-solver parameters is the load-angle dependence curve definition. This parameter acts as one of numerical parameters similar to element size because of the interpolation between the separate values. Simulations for FCOEF = 10, 19, 37 and 73 values ($\Delta\theta = 40^o$, 20^o, 10^o, 5^o) are performed. As shown in Figure 6, the relative

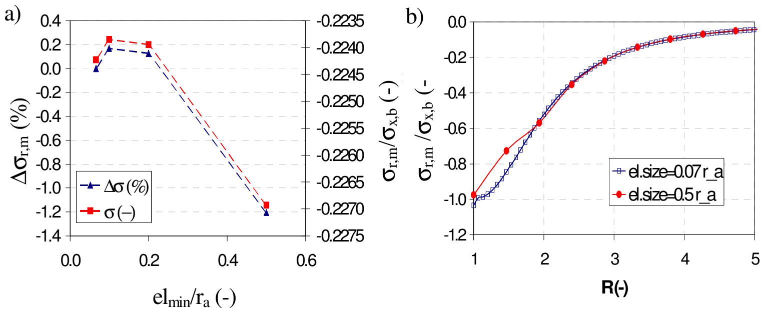

Figure 5. Near-hole mesh density influence. (a) Radial stresses in position $R = 2.83$, (b) radial stress along the axis x

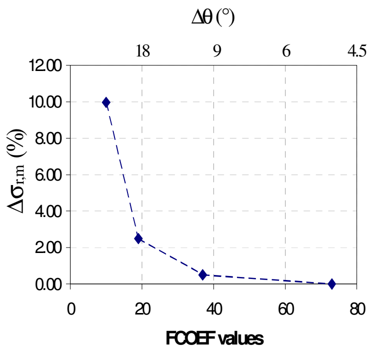

Figure 6. Number of FCOEF parameter ($\Delta\theta$) influence on stress in the strain gauge position $R = 2.83$

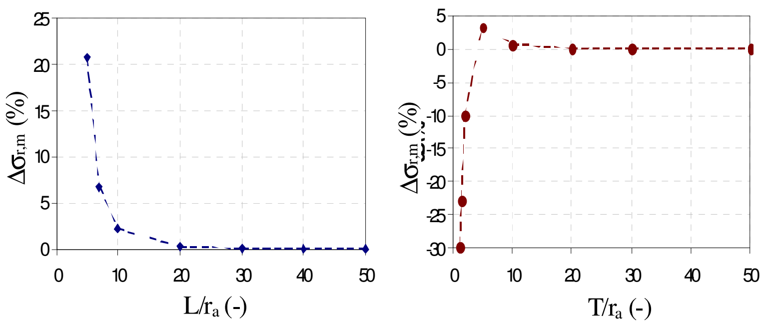

Figure 7. (a) Sample length influence on stress at strain gauge position $R = 2.83$; (b) sample thickness influence on stress in the strain gauge position $R = 2.83$

error up to 10% can occurs by insufficient FCOEF curve density and it decreases exponentially with angle step decreasing $\Delta\theta$ (increasing number of FCOEF values).

The sample shape and dimensions influence the stress/strain response as shown in [2,4] and also in Table 3 (numerical/analytical results comparison). Thus, the calibration functions are influenced as well. Simulation for different sample length (radius) and thickness is performed to investigate this dependence. The results are shown in Figure 7.

It can be seen that both the sample length and thickness play important role in dimensions comparable with the hole dimension. In the case of a small sample length (to $10r_a$) the strain relieved around the hole is influenced by a relieved strain at the sample boundaries as well. Than the error can reach values exceeding 20%. The difference decreases exponentially by increasing the sample length and at dimensions greater than $30r_a$ the error is negligible (less then 0.1%). Similar behavior can be observed for thickness variation. The error is not significant for the sample thickness greater than $30r_a$ (less then 0.1%). However, the error increases exponentially and can reach a few tens of percent (30% by $T = 1.2r_a$) by further sample thickness reduction.

The presented results demonstrate a model parameters influence on the relieved stress/strain response on the sample surface, thus on the computed calibration coefficients values as well. Similarly, any surface shape changes [1] or material inhomogeneities (by surface coating analysis for example) have an important role and should be considered by calibration coefficients determination and using. These features should be taken into account by the residual stress hole drilling method analysis and conditions of the calibration coefficients computation should correspond to a real analysed problem. Considering of standard ASTM coefficients should cause determined errors.

5. **Calibration coefficients evaluation**

A dependence of the strain $\varepsilon_r(h)$ on the (residual) stress $\sigma(H)$ is needed for the coefficients evaluation according to equation (5) and (6). The strain on the material surface is defined as

$$\varepsilon = \frac{u_r(r_2) - u_r(r_1)}{r_2 - r_1} \tag{10}$$

where r_i is radial position (distance from the hole) and $u_r(r)$ is displacement. Both the distance $(r_2 + r_1)/2$ and difference $r_2 - r_1$ should correspond to the strain gauge rosette main radius r_m and gauge element length l_{sg}. The displacement is a non-linear function of r, hence an incorrect setting of these parameters by strain evaluation influences the computed calibration coefficients.

An example of strain gauge rosette element length (l_{sg}) influence on the cumulative calibration coefficients according to equations (7a,b) are shown in Figure 8. The computation is performed for $h = H = 0.5r_m = 1.42r_a$ and the strain gauge main radius is $r_m/r_a = 2.83$, other model parameters agree with those in Table 1 and 4.

The gauge element length l_{sg}/r_a varies from 0.56-2.78 ($l_{sg}/r_a = 1.67$ for used HBM 1,5/120RY61S residual stress rosettes). The coordinates and displacements of nodes

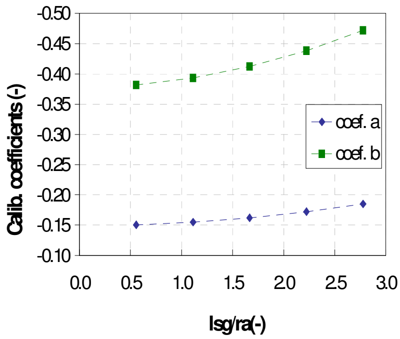

Figure 8. Calibration coefficients (cumulative) – strain gauge element length l_{sg} dependence

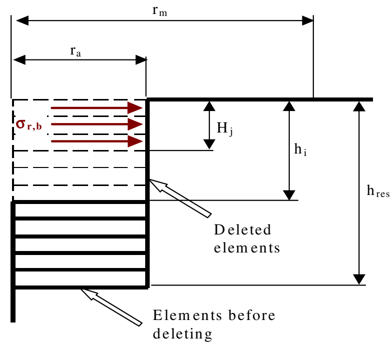

Figure 9. Calibration coefficients computation model scheme.

on principal axes at the interval of supposed grid lengths (from $r_m - l_{sg}/2$ to $r_m + l_{sg}/2$) are saved and approximated with a spline function, which is further used for strain computation according equation (10). The transverse gauge element grid size is omitted.

It can be seen from Figure 8 that the variations l_{sg} can cause differences up to a few tens percent. The true element length setting is also necessary for correct calibration coefficient computation and usage for given strain gauge rosette. Consideration of transverse gauge dimensions as shown in [3] can bring an further enhancement of result accuracy.

The coefficients A, B can be obtained by solving equation (6) for the boundary stress σ_x, ($\sigma_y = 0$) and computed strains $\varepsilon_x, \varepsilon_y$. It is better to compute the cumulative coefficients directly, according to Figure 9. The strain ε_i by given hole depth h_i is computed for acting stress σ_j, that is set to a whole depth region from 0 to H_j. The cumulative dimensionless coefficients are then computed according equations (7a,b).

$$a_{ij} = \frac{E}{1+\nu} \cdot \left(\sigma_{x,j}^{-1}\,\varepsilon_{x,i} + \sigma_{x,j}^{-1}\,\varepsilon_{y,i}\right) \tag{11a}$$

$$b_{ij} = E \cdot \left(\sigma_{x,j}^{-1}\,\varepsilon_{x,i} - \sigma_{x,j}^{-1}\,\varepsilon_{y,i}\right) \tag{11b}$$

Such computation is performed for all depths from $h_i = 0$ to $h_i = h_{res}$ and for all combination $H_j \leqslant h_i$ by each discrete depth h_i. Thus the required calibration coefficients matrices a_{ij} and b_{ij} respectively are obtained (lower triangular matrices - coefficients are not defined for $H > h$).

The computational procedures are time consuming because of repeated geometry generation, boundary conditions changes and results processing for each depth. Therefore an efficient computational procedure is investigated. Utilization of Cosmos/M FEM system appears to be a suitable solution due to its internal script language.

This language makes possible to solve of the whole problem, including parametric geometry generation, boundary condition setting, results saving, etc.

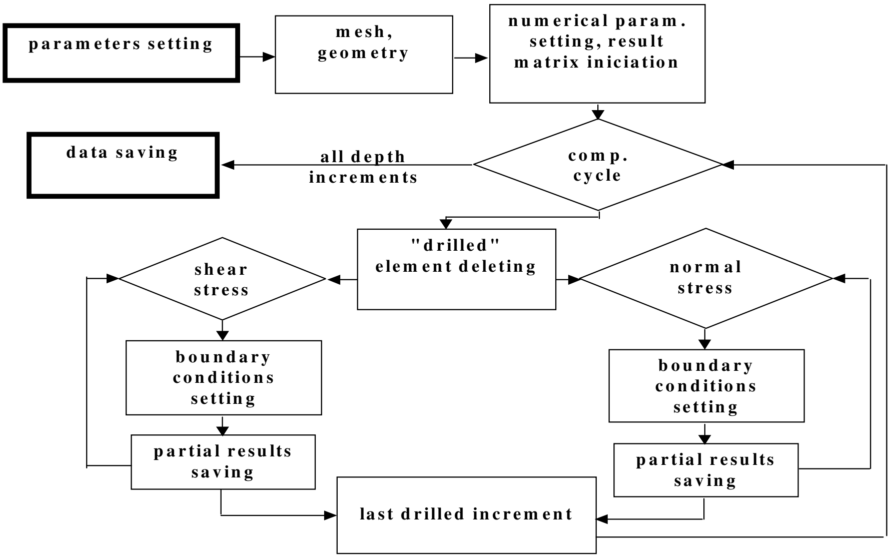

Figure 10. Calibration coefficients computational cycle scheme.

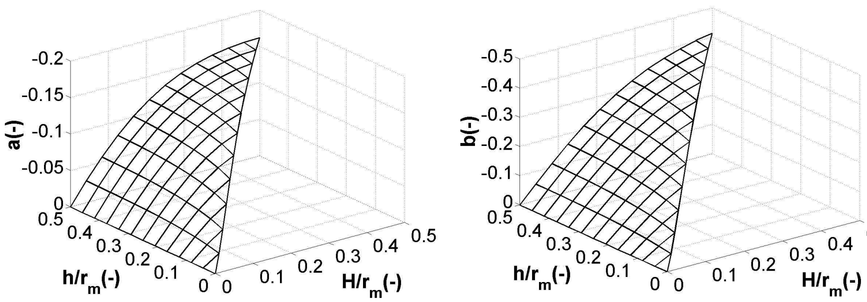

Figure 11. Dimensionless calibration coefficients a, b graphical representation as a function of hole depth h and stress acting depth H

The computational algorithm is shown in Figure 10. All parameters used in the program, the geometry and mesh generation and numerical parameters setting are defined in the program/script heading. The "hole-area" is divided in finite number of discrete increments (see Figure 9) that represent increments to be drilled out. In the main program cycle the elements in drilled area (from $h = 0$ to h_i) are deleted. The boundary conditions changes (boundary stress from 0 to H_j), computation and partial results savings for each increments H_j are provided by two nested loops for shear and normal stress component respectively according to equations (9a,b) (the

SGAL-solver does not support multiple load case definition). After the final depth h_{res} is achieved, the data matrix (monitored points/nodes coordinate, hole dept h_i, stress depth H_j and corresponding displacement values) are saved to disc and can be used for calibration coefficients evaluation. All the computational process is fully automatic. A user set only the problem parameters definition (hole radius, strain gauge rosette mean radius, elements density, etc.) in the script heading.

Calibration coefficients matrices graphical representation as a function $f(h, H)$ is shown in fig.11 as an example. Both h and H depths are related to r_m , what is more traditional. The computation is performed for $r_a = 0.353 r_m$, $l_{sg} = 0.588 r_m$ and $r_m = 2.55\ mm$ (HBM 1,5/120RY61S strain gauge rosette).

6. **Concluding remarks**

The model of the residual stress relieving due to the drilling a hole is made. A number of experimental computations are performed to test different model parameters. The solvers offered by the FEM system Cosmos/M are compared on the through-hole problem. The results show the error can reach up to 20% by insufficient mesh density for 3D model. On the contrary, geometrically symmetric model with asymmetric loading gives good results (difference about 0.1%) by significantly less computational requirements. Numerical results are verified by comparison with the analytical solution. The difference does not exceed several tenths of percent.

The influence of mesh density, sample length and thickness, asymmetric loading definition curve density and strain gauge element grid finite area is investigated. The error due to the insufficient mesh density can be several percent at strain gauge rosette mean radius position, but substantial dependence on distance from the hole is observed. Low density of the asymmetric loading definition curve can cause an error even 10% and so it appears as one of numerical important parameters like the mesh. An incorrect sample dimensions setting can cause an error up to 20%. Sample (surface) shape changes are supposed to be of the same influence, thus the model geometry should correspond to the real measured sample. The strain gauge element length, i.e. its finite dimensions, can also significantly influence the evaluated calibration coefficients in terms of non-linear displacement spatial dependence. This fact should not be omitted and the real strain gauge element length of a rosette used by measurement should be considered.

An efficient way in calibration coefficient computations appears to be using Cosmos/M script language. The procedure presented provides an automatic computation of the incremental drilling problem based on parameters defined in the script heading. Further research goal will be to adapt the coefficients computation technique to the hole drilling residual stress measurement method generalization. It can bring the method usage enhancement to inhomogeneous and an-isotropic materials for example or to include possible non-linear material behaviour during relaxation processes.

Acknowledgement. This paper is based upon work sponsored by the Ministry of Education of the Czech Republic under research and development project LN00B084.

References

1. Cherouat, A., Montay, G. and Lu. J.: Study of residual stresses in complex parts by experimental and numerical methods. *Material Science Forum*, **404-407**, (2002), 251-256.
2. Niku-Lari, A., Lu, J. and Flavenot, J. F.: Measurement of residual-stress distribution by the incremental hole-drilling method. *Journal of Mechanical Working Technology*, **11**, (1985), 167-188.
3. Lu, J. ed.): *Handbook of Measurement of Residual Stress.* The Fairmont Press, Inc., Lilburn, 1996.
4. Jong-Ning Aoh and Chung-Sheng Wei.: On the improvement of calibration coefficients for hole-drilling integral method: Part I-Analysis of calibration coefficients obtained by a 3-d FEM model. *Journal of Engineering Materials and Technology*, **124**, (2002), 250-258.
5. Schajer, G.S.: Application of Finite Element Calculations to residual stress Measurements. *Journal of Egineering Materials and Technology*, **103**, (1981), 157-163.
6. Schajer, G.S.: Measurement of non-uniform residual stress using the hole-drilling method. Part I - Stress calculation procedures. *Journal of Egineering Materials and Technology,* **110**, (1988), 338-343.
7. Schajer, G.S.: Measurement of non-uniform residual stress using the hole-drilling method. Part II - Practical application of integral method. *Journal of Egineering Materials and Technology,* **110**, (1988), 344-349,
8. Zhu Wu, Jian Lu and Bongtae Han: Study of residual stress distribution by a combined method of moire interferometry and incremental hole drilling. *Journal of Applied Mechanics*, **65**, (1998), 837-850.
9. Švantner M.: Computation of Calibration Coefficients for the Residual Stress Hole Drilling Measurement Technique. *Proceedings of 19-th user conference of Cosmos*, TechSoft Engineering, spol.s.r.o., Praha, (2002), 77-88. (in Czech)
10. Anon. *Cosmos/M 2.8 Online Manuals.* Structural Research and Analysis Corporation (SRAC), 2001.
11. Anon. *Measurement of Residual Stress by the Hole Drilling Strain Gauge Method.* Vishay-Measurements Group, Inc. Raleigh, 1993.
12. ASTM E 837. *Determining Residual Stresses by the Hole-Drilling Strain-gage Method*, American Society for Testing and Materials, Philadelphia, 1985.

Journal of Computational and Applied Mechanics, Vol. 6., No. 1., (2005), pp. 145–146

Book Review

Farkas, J. and Jármai, K. Economic design of metal structures. Rotterdam, Millpress, 2003.

This book is a continuation of the authors' previous book Analysis and Optimum Design of Metal Structures (Rotterdam, Balkema, 1997), since they have extended their research work to other interesting structural models and industrial problems and collected them from their studies in conference papers and journal articles published in recent years. The authors have developed a structural optimization system, the main components of which are the design constraints, fabrication aspects and economy. Economy is achieved by minimization of a cost function taking into account constraints on design and fabrication.

Chapter 1 describes the mathematical methods of optimization such as the genetic algorithm, the particle swarm method and the leap-frog algorithm. Chapter 2 covers cost calculation. The cost function is formulated according to the fabrication sequence and includes the costs of material, cutting and grinding of strut ends, assembly, welding, additional welding works and painting.

The structural models investigated and their specialties are as follows (Chapters 3-8):

- welded I- and box beams, including hollow flange I-beams as well as the economy of post-welding treatments to improve the fatigue strength of welded joints;
- tubular trusses, including a detailed minimum cost design of a triangular tubular truss to find the optimum truss height;
- sandwich structures, including the optimum design of a five-layer sandwich beam, which contains a central rubber layer for better vibration damping glued between two aluminium square box rods and two fiber-reinforced plastic laminates for decreasing the displacements;
- frames, including the cost comparison of welded and bolted beam-to-column connections;
- welded stiffened plates, including the optimization of the position of horizontal stiffeners in plates loaded by hydrostatic pressure; and
- welded stiffened shells, including the derivation of the radial deformation of a cylindrical shell due to the shrinkage of circumferential welds as well as the minimum cost design of a ring-stiffened cylindrical shell subject to external pressure.

The following industrial problems are treated (Chapters 9-12):

- Welded steel bridge decks;
- welded aluminium truck floors;
- welded steel punch presses for the light industry;
- square bunkers welded from stiffened steel plates.

The basic problem of the optimum design is the selection of suitable parameters (variables) to be optimized, for by changing of these variables better solutions can be achieved. In order to facilitate the selection, the characteristics of each structural type are given.

Since the problems are complicated, they can be treated only numerically. Therefore the validity of conclusions is somewhat restricted, but, in spite of this, many important lessons can be learned from the calculations elaborated. It can be concluded that each problem should be worked out considering the given special aspects and numerical data.

The book gives an insight into the latest research results in the field of structural optimization worthy of the attention of civil and mechanical engineers, designers, researchers, manufacturers, and undergraduate and postgraduate students.

It can be concluded that the structural optimization system developed by the authors is very flexible and gives designers a good basis for the consideration of all the important engineering aspects in developing modern structural versions.

Ferenc Orbán

Journal of Computational and Applied Mechanics, Vol. 6., No. 1., (2005), pp. 147–148

Calendar of Events

2005

August 7-12, 2005: Eindhoven, The Netherlands
Fifth Nonlinear Oscillations Nonlinear Dynamics Conference
Web: `http://yp.wtb.tue.nl/showemp.php/822`
Professor Dick H. van Campen, Department of Mechanical Engineering
Eindhoven University of Technology, 5600 MB Eindhoven, The Netherlands
E-mail: `D.H.v.Campen@tue.nl`
Phone: +31 40 247 2710, Fax: +31 40 243 7175

August 23-26, 2005: Žilina, Slovak Republic
Numerical Methods in Continuum Mechanics & 4th Workshop on Trefftz Methods
Professor V. Kompiš, University of Žilina, Slovak Republic
E-mail: `kompis@mppserv.utc.sk`
Web: `http://mppserv.utc.sk/NMCM2005`
Phone: +421 41 525 3352; Fax: +421 41 5652940

September 4-7, 2005: Paris, France
6th European Conference on Structural Dynamics, EURODYN 2005
Web: `http://www.eurodyn2005.univ-mlv.fr`
Prof. C. Soize, University of Marne la Vallee, Ing. 2000, Bat Copernic
5 Bd Descartes, F-77454 Marne la Vallee Cedex 2, France
E-mail: `eurodyn2005@univ-mlv.fr`
Phone: +331 60 95 77 99; Fax: +331 6095 76 61

September 5-7, 2005: Bologna, Italy
Seventh International Conference on Computer Methods
and Experimental Measurements for Surface Effects
and Contact Mechanics Contact/Surface 2005
Web: `http://www.wessex.ac.uk/conferences/2005/secm05/index.html`
Rachel Green, Senior Conference Co-ordinator, Wessex Institute of Technology Ashurst Lodge, Ashurst Southampton, SO40 7AA
5 Bd Descartes, F-77454 Marne la Vallee Cedex 2, France
E-mail: `rgreen@wessex.ac.uk`
Phone: +44 (0) 238 029 3223, Fax: +44 (0) 238 029 2853

October 12-14, 2005: Jurata, Poland
Shell Structures: Theory and Applications
Web: `http://www.ssta.pg.gda.pl/index.php`
SSTA 2005 Organizing Committee, Department of Structural Mechanics
Faculty of Civil and Environmental Engineering, Gdansk University of Technology
G. Narutowicza 11/12, 80-952 Gdansk, POLAND
E-mail: `ssta2005@pg.gda.pl`, Phone: 48-58-347-14-39

2006

January 2-6, 2005: Mérida, Yucatán, México

NINTH PAN AMERICAN CONGRESS OF APPLIED MECHANICS (PACAM IX)
Web: `http://www.mae.ncsu.edu/pacamix/`
Prof. Guillermo Monsivais Galindo, Instituto de Fisica de la UNAM
UNAM, Mexico City, MEXICO
E-mail: `monsi@fisica.unam.mx`

July 3-7, 2005: Alexandroupolis, Greece

S16TH EUROPEAN CONFERENCE OF FRACTURE ECF16
Web: `http://ecf16.civil.duth.gr/menu/welcome.php`
M.S. Konsta-Gdoutos, School of Engineering
Democritus University of Thrace
GR-67100, Xanthi, GR, Alexandroupolis, Greece
E-mail: `mkonsta@civil.duth.gr`
Phone: +30-25410-79651, 79658, Fax: +30-25410-79652

August 28-September 1, 2006: Budapest, Hungary

6TH EUROPEAN SOLID MECHANICS CONFERENCE
Web: `http://esmc2006.mm.bme.hu/`
Prof. Dr. Gábor Stépán, Budapest University of Technology and Economics
Department of Applied Mechanics, 1521 Budapest, P.O. Box 91, Hungary
E-mail: `esmc2006@mm.bme.hu`
Phone: +36 1 463 1369, Fax: +36 1 463 3471

Notes for Contributors

to the Journal of Computational and Applied Mechanics

Aims and scope. The aim of the journal is to publish research papers on theoretical and applied mechanics. Special emphasis is given to articles on computational mechanics, continuum mechanics (mechanics of solid bodies, fluid mechanics, heat and mass transfer) and dynamics. Review papers on a research field and materials effective for teaching can also be accepted and are published as review papers or classroom notes. Papers devoted to mathematical problems relevant to mechanics will also be considered.

Frequency of the journal. Two issues a year (approximately 80 pages per issue).

Submission of Manuscripts. Submission of a manuscript implies that the paper has not been published, nor is being considered for publication elsewhere. Papers should be written in standard grammatical English. Two copies of the manuscript should be submitted on pages of A4 size. The text is to be 130 mm wide and 190 mm long and the main text should be typeset in 10pt CMR fonts. Though the length of a paper is not prescribed, authors are encouraged to write concisely. However, short communications or discussions on papers published in the journal must not be longer than 2 pages. Each manuscript should be provided with an English Abstract of about 50–70 words, reporting concisely on the objective and results of the paper. The Abstract is followed by the Mathematical Subject Classification – in case the author (or authors) give the classification codes – then the keywords (no more than five). References should be grouped at the end of the paper in numerical order of appearance. Author's name(s) and initials, paper titles, journal name, volume, issue, year and page numbers should be given for all journals referenced.

The journal prefers the submission of manuscripts in LaTeX. Authors should prefer the AMS-LaTeX article class and are not recommended to define their own LaTeX commands. Visit our home page for further details concerning the issue how to edit your paper.

For the purpose of refereeing, two copies of the manuscripts should initially be submitted in hardcopy to an editor of the journal. The eventual supply of an accepted-for-publication paper in its final camera-ready form (together with the corresponding files on an MS–DOS diskette) will ensure more rapid publication. Format requirements are provided by the home page of the journal from which sample LaTeX files can be downloaded:

`http://www.uni-miskolc.hu/home/web/pumns/mechanics`

These sample files can also be obtained directly (via e-mail) from a member of the Editorial Board, Gy. Szeidl (Gyorgy.SZEIDL@uni–miskolc.hu), upon request.

Twenty offprints of each paper will be provided free of charge and mailed to the correspondent author.

The Journal of Computational and Applied Mechanics is abstracted in Zentralblatt für Mathematik and in the Russian Referativnij Zhurnal.

Responsible for publication: Rector of the Miskolc University
Published by the Miskolc University Press under the leadership of Dr. József PÉTER
Responsible for duplication: works manager Mária KOVÁCS
Number of copies printed: 200
Put to the Press on June 14, 2005
Number of permission: TU 2005-520-ME **HU ISSN 1586–2070**

A Short History of the Publications of the University of Miskolc

The University of Miskolc (Hungary) is an important center of research in Central Europe. Its parent university was founded by the Empress Maria Teresia in Selmecbánya (today Banska Štiavnica, Slovakia) in 1735. After the first World War the legal predecessor of the University of Miskolc moved to Sopron (Hungary) where, in 1929, it started the series of university publications with the title *Publications of the Mining and Metallurgical Division of the Hungarian Academy of Mining and Forestry Engineering* (Volumes I.-VI.). From 1934 to 1947 the Institution had the name Faculty of Mining, Metallurgical and Forestry Engineering of the József Nádor University of Technology and Economic Sciences at Sopron. Accordingly, the publications were given the title *Publications of the Mining and Metallurgical Engineering Division* (Volumes VII.-XVI.). For the last volume before 1950 – due to a further change in the name of the Institution – *Technical University, Faculties of Mining, Metallurgical and Forestry Engineering, Publications of the Mining and Metallurgical Divisions* was the title.

For some years after 1950 the Publications were temporarily suspended.

After the foundation of the Mechanical Engineering Faculty in Miskolc in 1949 and the movement of the Sopron Mining and Metallurgical Faculties to Miskolc, the Publications restarted with the general title *Publications of the Technical University of Heavy Industry* in 1955. Four new series - Series A (Mining), Series B (Metallurgy), Series C (Machinery) and Series D (Natural Sciences) - were founded in 1976. These came out both in foreign languages (English, German and Russian) and in Hungarian.

In 1990, right after the foundation of some new faculties, the university was renamed to University of Miskolc. At the same time the structure of the Publications was reorganized so that it could follow the faculty structure. Accordingly three new series were established: Series E (Legal Sciences), Series F (Economic Sciences) and Series G (Humanities and Social Sciences). The latest series, i.e., the series H (European Integration Studies) was founded in 2001. The eight series are formed by some periodicals and such publications which come out with various frequencies.

Papers on computational and applied mechanics were published in the

Publications of the University of Miskolc, Series D, Natural Sciences.

This series was given the name Natural Sciences, Mathematics in 1995. The name change reflects the fact that most of the papers published in the journal are of mathematical nature though papers on mechanics also come out.

The series

Publications of the University of Miskolc, Series C, Fundamental Engineering Sciences

founded in 1995 also published papers on mechanical issues. The present journal, which is published with the support of the Faculty of Mechanical Engineering as a member of the Series C (Machinery), is the legal successor of the above journal.

Journal of Computational and Applied Mechanics
Volume 6, Number 1 (2005)

Contents

Contributed Papers